Interpolation-Based Modelling of Microwave Ring Resonators

Marlize Schoeman

Dissertation presented for the degree of Doctor of Philosophy
in Engineering at the University of Stellenbosch
Supervisor: Prof. P. Meyer
December 2006

Declaration

I, the undersigned, hereby declare that the work contained in this dissertation is my own original work and that I have not previously in its entirety or in part submitted it at any university for a degree.

M. Schoeman _____ Date _____

Abstract

Keywords—Adaptive interpolation-based modelling, Vector Fitting, Thiele-type continued fractions, ring resonators, resonant frequencies, Q-factors

Resonant frequencies and Q-factors of microwave ring resonators are predicted using interpolation-based modelling.

A robust and efficient multivariate adaptive rational-multinomial combination interpolant is presented. The algorithm models multiple resonance frequencies of a microwave ring resonator simultaneously by solving an eigenmode problem. To ensure a feasible solution when using the Method of Moments, a frequency dependent scaling constant is applied to the output model. This, however, also induces a discontinuous solution space across the specific geometry and requires that the frequency dependence be addressed separately from other physical parameters. One-dimensional adaptive rational Vector Fitting is used to identify and classify resonance frequencies into modes. The geometrical parameter space then models the different mode frequencies using multivariate adaptive multinomial interpolation.

The technique is illustrated and evaluated on both two- and three-dimensional input models. Statistical analysis results suggest that models are of a high accuracy even when some resonance frequencies are lost during the frequency identification procedure.

A three-point rational interpolant function in the region of resonance is presented for the calculation of loaded quality factors. The technique utilises the already known interpolant coefficients of a Thiele-type continued fraction interpolant, modelling the S-parameter response of a resonator. By using only three of the interpolant coefficients at a time, the technique provides a direct fit and solution to the Q-factors without any additional computational electromagnetic effort.

The modelling algorithm is tested and verified for both high- and low-Q resonators. The model is experimentally verified and comparative results to measurement predictions are shown. A disadvantage of the method is that the technique cannot be applied to noisy measurement data and that results become unreliable under low coupling conditions.

Opsomming

Sleutelwoorde—Aanpasbare interpolasiegebaseerde modellering, Vektor Passing, Thiele volgehoue breukuitbreidings, ring resoneerders, resonansie frekwensies, Q-faktore

Resonansie frekwensies en Q-faktore van mikrogolf ring resoneerders word met behulp van interpolasiegebaseerde modelleringstegnieke voorspel.

'n Robuuste en effektiewe multi-veranderlike aanpasbare rasionale-multinome kombinasie interpolant word beskryf. Die algoritme modelleer verskeie resonansie frekwensies van 'n mikrogolf ring resoneerder gelyktydig deur die oplossing van 'n eiewaarde probleem te vind. Om 'n sinvolle oplossing te verseker wanneer die Metode van Momente gebruik word, word 'n frekwensie afhanklike skaleringskonstante op die uittreemodel aangewend. Toepassing van hierdie skaleringskonstante veroorsaak egter dat die oplossingsruimte diskontinu is oor die spesifieke geometrie en vereis daarom dat die frekwensie afhanklikheid apart van die fisiese parameters aangespreek word. Een-dimensionele aanpasbare rasionale Vektor Passing word gebruik om die resonansie frekwensies te identifiseer en in modusse te kategoriseer. In die geometriese parameterruimte word die verskeie modusfrekwensies daarna met multi-veranderlike aanpasbare multinome interpolasie gemodelleer.

Die tegniek word gedemonstreer en geëvalueer op beide twee- en drie-dimensionele intreemodelle. Resultate verkry vanaf statistiese analise dui daarop dat modelle van 'n hoë akkuraatheid is, selfs wanneer van die resonansie frekwensies gedurende die identifikasie algoritme verlore gaan.

'n Drie-punt rasionale interpolant funksie in die omgewing van resonansie vir die berekening van belaste kwaliteitsfaktore word beskryf. Die tegniek gebruik die reeds bekende koëffisiënte van die Thiele volgehoue breukuitbreidingsmodel wat die S-parameter gedrag van 'n resoneerder beskryf. Deur slegs drie van die interpolant koëffisiënte op 'n keer te gebruik, maak die tegniek voorsiening vir 'n direkte passing en oplossing van die Q-faktore sonder enige addisionele elektromagnetiese berekeningskoste.

Die modelleringsalgoritme is teen beide hoë en lae Q resoneerders getoets en geverifieer. Die model is eksperimenteel bevestig en vergelykende resultate teenoor meetvoorspellings word getoon. 'n Nadeel van die metode is dat die tegniek nie op ruiserige meetdata toegepas kan word nie en dat resultate onbetroubaar word onder lae koppelingstoestande.

"That's why scientists persist in their investigations, why we struggle so desperately for every bit of knowledge, stay up nights seeking the answer to a problem, climb the steepest obstacles to the next fragment of understanding, to finally reach that joyous moment of the kick in the discovery, which is part of the pleasure of finding things out."

Richard P. Feynman (1918–1988)

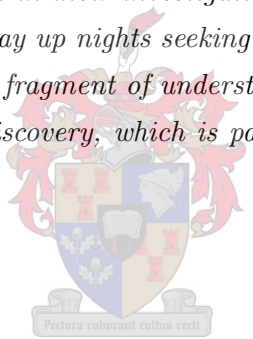

Acknowledgements

I wish to express my sincere gratitude to everyone who has contributed to this thesis in any way. In particular, I would like to convey my thanks to the persons and institutions below:

i) Professor Petrie Meyer who has left deep footprints in my life, both on an academic and on a personal level. I am in debt to Petrie for his unprecedented helpfulness and patience. Thank you for always being available and genuinely concerned in solving my problems. I really enjoy working with you.

ii) Everyone at the E&E Department, thank you for your friendliness and help throughout my nine years of tertiary education. It was indeed a wonderful experience.

iii) Wessel Croukamp, Lincoln Saunders and Ashley Cupido for manufacturing the ring resonators.

iv) EMSS and CST who kindly made their software packages FEKO and CST Microwave Studio available for academic use.

v) David, Thomas and Nielen for unselfishly sharing their computers and running simulations to acquire many of the computational results presented in this work.

vi) Bronwyn and Thomas for proofreading this work with much patience and diligence.

vii) The financial assistance of the National Research Foundation (NRF) toward this research is hereby acknowledged. Opinions expressed and conclusions arrived at, are those of the author and should not necessarily be attributed to the NRF.

viii) My family, for their love, patience and encouragement, and for showing interest, even though they do not always understand the finer details of my work.

ix) All my friends, thank you for always reminding me how much more there is to life outside of my academic life. Thank you for your prayers, support and encouragement, especially during times of difficulty.

Finally, to my Creator and Saviour, Jesus Christ. My praise and thanks for the life that I have—I am nothing without You.

Contents

List of Tables

List of Figures

Chapter 1

Introduction

Microwave resonators play an important role in devices used in high-frequency communication systems such as filters and oscillators. The successful modelling and accurate prediction of resonator characteristics such as resonance frequencies and Q-values, are therefore becoming increasingly important to designers of microwave devices. In order to reduce the cost of the design of microwave circuits, computer-aided design (CAD) tools providing a first-pass success level, are required. While circuit models and the use of simplified structures provide fairly accurate solutions in some cases, they are limited to lower-order resonant modes and specific ranges of dimensions. Computational electromagnetic (CEM) analysis techniques are widely accepted to provide high-accuracy models for general microwave structures over a wide range of frequency and/or physical dimensions. The computational effort required can, however, become excessive, especially for large and complex structures.

An increasing need to reduce the computational effort required in the design of microwave devices, has in recent years resulted in the development of metamodelling techniques, where surrogate or mathematical models are calculated for specific microwave structures. Once created, these models can be evaluated quickly, with minimal computational effort, and are therefore fit for optimisation-based iteration. The term 'surrogate' encompasses any model calculated from CEM analysis, and includes look-up tables, interpolation techniques and artificial neural networks [1].

Since these metamodels directly fit data from CEM simulations, their model accuracy is high. Of these models, interpolation-based metamodels have proved in recent years to be the most computationally efficient, to require the least storage as only the interpolant coefficients are stored, and to require the smallest amount of CEM analyses to establish a model. In addition, the models are fast to evaluate and are well suited for circuit optimisation and statistical design [2,3]. Present interpolation-based implementations focus mainly on the modelling of system responses, such as S-parameters, and not on derived parameters of these responses [4–11]. For microwave

resonators, however, it is the derived parameters f_0 and Q that are of prime importance to designers. A typical design of a microwave filter would require the optimisation of a given resonant circuit for required values of f_0 and Q, or even multiple values of f_0 and Q for dual and triple mode filters.

When CEM techniques are used for the generation of support samples, it is of the utmost importance to minimise the required number of samples. This can be achieved by the use of adaptive sampling techniques where the order of the function is gradually increased until the desired accuracy is reached. The adaptive procedure serves to find the key data points for modelling the system quickly, with or without internal knowledge of the model itself. This requires that a suitable error function exists and that unequally spaced support points can be used [4, 12–14].

The aim of this dissertation is to investigate and establish adaptive interpolation-based meta-models to successfully characterise highly resonant microwave structures using a full-wave Method of Moments (MoM) analysis.

1.1 History of Interpolation Models

The accuracy of an interpolation model depends on the ability of the basis functions to represent the data. When computing a polynomial interpolant, the basis essentially consists of the different orders of the polynomial. Switching from one variable to many variables is, however, not trivial. Not only is there an extensive choice of multivariate functions, but moreover, different algorithms yield different interpolants and apply to different applications.

While polynomial functions are often used as interpolants, rational functions yield better results for functions containing poles and zeros in the data. Polynomial interpolation is also prone to oscillations and an acceptable accuracy is occasionally achieved only by polynomials of intolerably high degree [15]. A rational function can be constructed by calculating the explicit solution of a system of interpolatory conditions, by starting a recursive algorithm, or by calculating the convergent of a continued fraction [16]. In [17], Deschrijver gives an overview and comparison of some of the most commonly used univariate rational fitting methods. These include power series, Chebyshev polynomials of the first and second kind, orthonormal Forsythe polynomials, Lanczos-based methods, the Cauchy method [18], Padé approximations [19], Vector Fitting (VF) [20] and Thiele-type continued fractions [21], and are most often used to model deterministic, simulation based data. Among these, the Thiele continued fractions approach and the Vector Fitting pole-residue method were identified as the most successful in generating models of high accuracy. The use of continued fractions as interpolants is a computationally efficient method and gives accurate numerical results [16], although the method lacks the ability to incor-

porate noise in the model. The Vector Fitting technique estimates residues of partial fractions, which requires less significant digits than the coefficients of a polynomial. When combined with least-squares methods, it therefore provides a more accurate representation for broadband solutions [17]. In Chapter 3 the Thiele and Vector Fitting approaches will be discussed in greater detail.

One of the most straightforward approaches to extending a single variable interpolant to a multivariate interpolant was presented in 1998, where Peik [6] extended the univariate Cauchy method to higher dimensions by setting up and explicitly solving a system of interpolatory conditions. Since the adaptive selection of support points and model order require solving the system numerous times, the technique is considered computationally ineffective, inaccurate and suitable for simple models only. For higher dimensions, Peik developed a fast and stable algorithm in which the adaptive sampling can be applied only in one dimension and all other samples have to form a completely filled uniform or non-uniform grid of support points.

In 1999, De Geest and Dhaene [7, 22] proposed automatic parameterised model creation and a global analytical fitting model, by separating frequency from other physical parameters. Orthonormal multivariate polynomials are used to build a model for the geometrical parameters at a single frequency, and rational interpolation is used to combine these polynomials to determine the entire parameter space. To reduce the number of support points while retaining the speed and stability of the interpolating algorithm, Lehmensiek [16] developed techniques in 2001 based on the Thiele-type branched continued fraction representation of a rational function. The algorithms operate by using univariate adaptive sampling along a selected dimension. In this way, while the support points do not fill the grid completely, they are being added along straight lines passing through the multi-dimensional space. The first completely adaptive multivariate rational interpolation model was suggested in 2003, where Lamecki [9] developed a technique that supports the addition of sample points along all dimensions simultaneously. Compared to previous techniques, a significant four times reduction in the number of support samples was achieved.

Since 2003, the key difference between the various multivariate rational methods has been the approach used to evaluate the order of the multinomials and the coefficients that define them. In 2005, Hendrickx [23] presented a sequential design and adaptive methodology to capture the complex input-output behaviour of the simulator in a multivariate surrogate model. The author also introduced model quality assessment by which each model's accuracy may be asserted. Most recently, Cuyt [11] constructed an interpolating rational function in such a way that it minimises both the truncation error and the amount of simulation data. The problem was reformulated in terms of an orthogonal Chebyshev product basis, which addresses severe ill-conditioning of the system when using the classical multinomial basis. In Chapter 6 a more in depth study on the history of multi-dimensional models is given.

1.2 Original Contributions

Current applications of interpolation-based techniques to the modelling of electromagnetics-based devices focus mainly on the modelling of system responses. Designers of microwave resonators are, however, more interested in the modelling of derived parameters, specifically resonance frequencies and quality factors. The aim of this dissertation is to investigate and develop the theory for adaptive interpolation-based modelling algorithms for the accurate identification of the resonant frequencies and quality factors of microwave ring resonators. To perform CEM analyses, an in-house Method of Moments (MoM) code is used, which was developed during earlier research [24].

The primary original contributions of this work are [25–29]:

i) *The development of a multivariate adaptive rational-multinomial combination interpolant for the modelling of multiple resonance frequencies of a microwave ring resonator* [29]. The algorithm models multiple resonance frequencies of a microwave ring resonator by solving the eigenmode problem $\det[Z(s, \mathbf{X})]$. To ensure a feasible solution when using the Method of Moments, a frequency dependent scaling constant is applied to the output model. A discontinuous solution space across the specific geometry requires that the frequency dependence be addressed separately from other physical parameters. One-dimensional adaptive rational Vector Fitting is used to identify and classify resonance frequencies into modes. The geometrical parameter space then models the different mode frequencies using multivariate adaptive multinomial interpolation. The technique was successfully verified against two- and three-dimensional input models and utilises the following original sub-algorithms:

   (a) The development of a new adaptive sampling convergence criterion based on the position of the roots (resonance frequencies) of the rational model [28]. A 25% reduction in the number of support points required to accurately predict the natural frequencies of a microwave resonator is achieved.

   (b) The development of an automated process by which an identified resonance frequency is associated with a specific mode. The technique utilises correlation of the ideal current patterns of simplified resonator models to the actual current pattern evaluated at the identified frequency [29].

   (c) The development of a constrained grid modelling algorithm. Evaluation samples are restricted to regions where the output parameter exists within the pre-defined parameter space [29].

ii) *A comparison of two one-dimensional adaptive rational metamodelling techniques, the Thiele continued fraction and the Vector Fitting pole-residue methods, in their application to predicting the resonance frequencies of the well-documented microstrip ring resonator* [27].

The research involved investigation of convergence effects due to finite meshing and the interpolation error, accuracy and pole-zeros issues in the identification of different classes of roots, and presenting the usefulness of each technique in predicting the zeros (i.e. the resonance frequencies) of these models.

iii) *The development of a three-point rational interpolation method for the calculation of loaded quality factors* [25, 26].
A new technique for the calculation of the loaded quality factor was proposed by using the same Thiele continued fraction rational interpolant as was calculated to model the S-parameters. By using only three of the interpolant coefficients at a time, the Q-factors are obtained without any additional CEM effort. In standard techniques the extraction of quality factors is obtained by Q-circle fits on multi-frequency S-parameter data. However, where these techniques rely on least-squares fits which normally require large numbers of frequency points, the new technique provides a direct fit and solution to the Q-factors.

iv) *The development of a frequency-dependent scaling constant* [25, 26].
In order to solve for the natural frequencies of closed structures in the absence of excitation, many CEM techniques require solution of

$$\det[Z(s)] = 0. \tag{1.1}$$

The MoM approach to solving Eq. 1.1 leads to the unique numerical problem that $\det[Z(s)]$ evaluates to extremely small values, which also vary quite dramatically in magnitude over frequency. Standard determinant functions are unable to accurately evaluate to such small values, and to ensure an accurate fit, a frequency-dependent scaling constant was developed to adjust the determinant function to values of a similar order of magnitude. Since scaling has no effect on the position of the roots of a function, this is a perfectly viable option. In addition, the functionality of the MoM CEM tool could now be expanded by adding an MoM eigenmode solver.

The secondary contributions are:

i) The development of a method for finding the roots of a Vector Fitting rational model [27]. Three methods were proposed and compared to calculate pole-free solutions to the Thiele continued fraction and Vector Fitting pole-residue models of the characteristic equation $\det[Z(s)]$. The VF formulation iteratively relocates its poles by calculating the zeros of a rational scalar function. By adapting this technique of root-finding, the roots of the rational VF interpolant can now also be calculated. This technique of root-finding has never been applied to the problem of microwave resonators.

ii) The development of an algorithm for the extraction of the resonant frequencies from a rational approximation of the scattering parameter magnitude plot [26].

iii) The adaptation of the boundary conditions used in the Green's function and MoM formulation to include conductor losses on infinite ground planes.

iv) The reformulation of a MoM loading technique to allow extraction of scattering parameters. The technique was developed for use with triangular vector basis functions and multiple half-basis functions at each port are supported.

1.3 Overview of the Dissertation

Chapter 2 presents a brief outline of the MoM formulation that is used to perform CEM analyses, while the two aspects of accurate loss calculation and efficient S-parameter extraction are discussed in greater detail.

Chapter 3 introduces one-dimensional adaptive rational interpolation. Two techniques, Thiele continued fraction and Vector Fitting, have been found most useful in providing models of high accuracy. Since these algorithms are utilised in Chapters 4 and 5, a detailed exposition of the theory on the Thiele-type and Vector Fitting methods is given.

Chapter 4 focuses on the efficient and accurate prediction of the resonant frequencies of microwave ring resonators using one-dimensional rational interpolation techniques. Two techniques are discussed—the first approach is based on the solution of an eigenmode problem (i.e. a resonator without ports) while the second method uses the S-parameter response of a resonator coupled to input and output loads. Next, in Chapter 5, the one-dimensional Thiele-type rational interpolant is utilised to accurately predict the quality factors of microwave ring resonators.

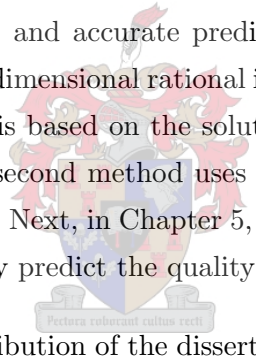

Chapter 6 presents the main contribution of the dissertation, namely a multi-dimensional adaptive rational-multinomial interpolation algorithm. The algorithm is discussed by addressing aspects such as the metamodel definitions, a mode identification algorithm, constrained grid modelling, suitable degree sets, model quality assessment and the selection of new sample locations. The algorithm is verified by means of two-dimensional and three-dimensional examples and its numerical performance and accuracy is discussed.

Finally, Chapter 7 contains possible extensions to the theory presented here and a conclusion.

Chapter 2

Method of Moments (MoM)

Accurate full-wave electromagnetic models are required to account for effects such as dispersion, surface waves, radiation and coupling in microwave structures. Among the numerical techniques applicable to general electromagnetic problems, the MoM is widely regarded as one of the most popular techniques for the solution of the Mixed-Potential Integral Equation (MPIE) for printed geometries in planar layered media [30–32].

An in-house Method of Moments code, previously developed by the author [24], serves as the basis utility with which the full-wave electromagnetic analyses are performed in this dissertation. This chapter briefly presents the formulation used in this MoM code. Of particular importance in the analysis of planar resonators, is the accurate calculation of losses and an efficient S-parameter extraction technique. These two aspects are discussed in detail.

In standard MoM, the solution procedure approximates an integral equation with a system of simultaneous linear algebraic equations in terms of an unknown current distribution I_n as

$$[Z_{mn}(s)][I_n] = [E_m]. \tag{2.1}$$

Here Z_{mn} is an impedance matrix varying as a function of frequency and E_m is the excitation vector. The MoM formulation uses vector-valued basis functions [33] defined over a triangular mesh to model electric surface currents $\mathbf{J}_s$ on conducting scatterers and magnetic surface currents $\mathbf{M}_s$ on slotline interfaces. In this brief overview, however, it will be assumed that only electric surface currents are present, which may be approximated with a series of basis functions $\mathbf{f}_n$ as

$$\mathbf{J}_s(\mathbf{r}') \approx \sum_{n=1}^{N} I_n \mathbf{f}_n(\mathbf{r}'). \tag{2.2}$$

In the standard integral equation formulation the tangential electric fields should be proportional to the total surface currents. Assuming conductor losses to be negligible, the total tangential electric field, i.e. the sum of the incident and scattered fields, is forced to be zero on all conducting

surfaces

$$\hat{\mathbf{n}} \times (\mathbf{E}^i + \mathbf{E}^s) = 0, \tag{2.3}$$

where the scattered electric field $\mathbf{E^s}$ can be computed from the potentials $\mathbf{A}$, $\mathbf{F}$ and Φ by

$$\mathbf{E}^s = -j\omega\mathbf{A} - \nabla\Phi - \frac{1}{\epsilon}\nabla \times \mathbf{F}. \tag{2.4}$$

On substituting Eq. 2.4 (assuming $\mathbf{F} = 0$ for a zero magnetic surface current) into Eq. 2.3, a single expression for the MPIE is obtained

$$\hat{\mathbf{n}} \times \mathbf{E}^i = \hat{\mathbf{n}} \times (j\omega\mathbf{A} + \nabla\Phi), \tag{2.5}$$

where the integral equations defining the magnetic vector and electric scalar potentials are given by

$$\begin{aligned} \mathbf{A}(\mathbf{r}) &= \int_s \bar{\bar{\mathbf{G}}}_A(\mathbf{r}|\mathbf{r}') \cdot \mathbf{J}_s(\mathbf{r}')dS' \\ \Phi(\mathbf{r}) &= \int_S G_\Phi(\mathbf{r}|\mathbf{r}')q_s(\mathbf{r}')dS'. \end{aligned} \tag{2.6}$$

Here $\bar{\bar{\mathbf{G}}}_A$ and G_Φ are the magnetic vector and electric scalar potential Green's functions, and q_s is the surface charge density caused by the electric surface current density $\mathbf{J}_s$.

Since Eq. 2.5 is only a single equation with N unknowns, a method of weighted residuals is enforced to obtain a set of N independent equations. With the testing function $\mathbf{g}_m$ identical to the basis function $\mathbf{f}_n$, and the symmetric product

$$< \mathbf{f}, \mathbf{g} > = \int_S \mathbf{f} \cdot \mathbf{g}dS, \tag{2.7}$$

it follows that

$$< \mathbf{E}^i, \mathbf{g}_m > = j\omega < \mathbf{A}, \mathbf{g}_m > + < \nabla\Phi, \mathbf{g}_m >, \tag{2.8}$$

which upon substitution of the current expansion terms of Eq. 2.2 reduces to the corresponding MoM system equation (Eq. 2.1) with $n = 1, 2, \cdots, N$ and $m = 1, 2, \cdots, N$.

The Green's functions ($\bar{\bar{\mathbf{G}}}_A$ and G_Φ) used in the MoM analysis are those for a stratified medium consisting of a number of dielectric layers separated by planar interfaces parallel to the xy plane of a Cartesian coordinate system [34, 35]. Each layer extends to infinity in the transverse directions and consists of an isotropic, homogeneous material characterised by permeability μ_i and permittivity ϵ_i, which may be complex if the medium is lossy. The upper- and lowermost regions are half-spaces and extend to $\pm\infty$ in the z direction. Finally, boundary conditions allow for the introduction of metallic/PEC ground planes at any of these interfaces.

Following a spectral domain Sommerfeld plane wave formulation, the analysis presented in [34,35] first solves for the fields of an electric dipole in free space. The formulation then calculates the

fields of an arbitrary directed dipole embedded in a layered medium by matching boundary conditions across the discontinuities at the planar interfaces. Using Sommerfeld's identity, the free-space solution is then transformed to a summation of TE- and TM-type plane waves in the z direction. These are characteristic of stratified media and present a convenient form to easily match boundary conditions relating incident and reflected plane waves at the layer interfaces. Finally, the Green's functions for the normal components of the field are related to the Green's functions for the vector and scalar potentials.

2.1 Loss Considerations

Losses encountered in microwave circuits are often divided into dielectric, conduction, radiation and surface wave losses. The first two loss factors have been dealt with extensively in the literature and good approximations exist for the modelling of microstrip transmission lines [36, 37]. Radiation and surface wave losses are less well understood and quantitative solutions are difficult to come by as these treatments are limited to specific circuit discontinuities [38].

The various loss contributions for a microwave resonator can be represented by Q-values of the form

$$Q = 2\pi f_0 \frac{W_{\max}}{P_d} = \left(\frac{1}{Q_d} + \frac{1}{Q_c} + \frac{1}{Q_r} + \frac{1}{Q_{sw}}\right)^{-1}, \tag{2.9}$$

where f_0 is the resonant frequency, $W_{\max}$ is the stored energy, P_d is the average power loss in the resonator and Q_d, Q_c, Q_r and Q_{sw} are the respective dielectric, conductor, radiation and surface wave quality factors.

Treatments in [39] and [40] combined the different loss contributions into a single quantity known as the effective loss tangent $\tan(\delta_{\text{eff}})$ to account for the total losses in the resonator

$$\tan(\delta_{\text{eff}}) = \frac{1}{Q_d} + \frac{1}{Q_c} + \frac{1}{Q_r} + \frac{1}{Q_{sw}}. \tag{2.10}$$

According to [39], the magnitude of $\tan(\delta_{\text{eff}})$ is usually substantially larger than the substrate loss tangent $\tan(\delta)$, and also varies as a function of the substrate parameters $\tan(\delta)$ and height h.

After analysing the approximations presented in [36, 37, 41], however, it becomes apparent that the various loss components behave differently as functions of frequency. The dielectric attenuation constant varies as a function of the relative dielectric constant $\epsilon_{r,\text{eff}}$ and wavelength λ_g, while the conductor attenuation constant varies as a function of the effective line width w_{eff} and surface resistance R_s of the conductor. Furthermore, according to [38], radiation becomes the dominant factor at higher frequencies, especially for low-impedance lines and thick substrates with a low dielectric constant.

To increase the accuracy of the models, each loss component therefore has to be treated separately.

Dielectric Losses

Dielectric loss is a function of the material properties, for which typical values may be found in the manufacturer's data sheets as the substrate dissipation factor $\tan(\delta)$. This is incorporated into the simulation code by means of a complex permittivity

$$\epsilon = \epsilon_0(\epsilon' - j\epsilon'') = \epsilon_0\epsilon_r(1 - j\tan(\delta)). \tag{2.11}$$

Conductor Losses

In the MPIE formulation explained above, the total tangential electric field is forced to be zero on all conducting surfaces (Eq. 2.3). This condition assumes conductor losses to be negligible. At higher frequencies, however, the well-known skin effect occurs because of the decay of fields into the conductor. In this case, the current is flowing in a small surface layer and the behaviour of the conductor is usually described in terms of the surface impedance [42]

$$Z_s = \frac{1+j}{\sigma\delta}, \tag{2.12}$$

where the skin depth δ is given by $\delta = \sqrt{2/\omega\mu\sigma}$, with σ being the conductor conductivity.

Ideally, the value of Z_s should be obtained by measurement, since conductivity depends on the thickness and the roughness of the conducting surface. As an approximation, however, the conductivity σ can be replaced by an effective conductivity $\sigma_{\text{eff}}(f)$, which can be considerably lower than the conductivity found in standard tables [43]. According to [44], the effective conductivity can be calculated as

$$\sigma_{\text{eff}}(f) = \frac{\sigma}{\left[1 + \left(e^{(-\delta/\Delta)}\right)^{1.6}\right]^2}, \tag{2.13}$$

where Δ is the surface roughness. Fig. 2.1 illustrates the change in copper conductivity[†] as a function of frequency and varying surface roughness.

In the MoM formulation, conductor losses on the (meshed) scatterers are accounted for by replacing the ideal boundary condition with the *Leontovich* boundary condition

$$\hat{\mathbf{n}} \times \mathbf{E} = Z_s\mathbf{J}_s. \tag{2.14}$$

Thus, the total tangential electric field is now proportional to the total equivalent electric surface current

$$\hat{\mathbf{n}} \times (\mathbf{E}^i + \mathbf{E}^s) = Z_s\mathbf{J}_s, \tag{2.15}$$

which changes the final expression for the MPIE (Eq. 2.5) to

$$\hat{\mathbf{n}} \times \mathbf{E}^i = \hat{\mathbf{n}} \times \left(j\omega \int_s \bar{\bar{\mathbf{G}}}_A(\mathbf{r}|\mathbf{r}') \cdot \mathbf{J}_s(\mathbf{r}')dS' + \nabla \int_S G_\Phi(\mathbf{r}|\mathbf{r}')q_s(\mathbf{r}')dS' \right) + Z_s\mathbf{J}_s(\mathbf{r}). \tag{2.16}$$

[†]Conductivity of copper: $\sigma = 5.813 \times 10^7$ S/m

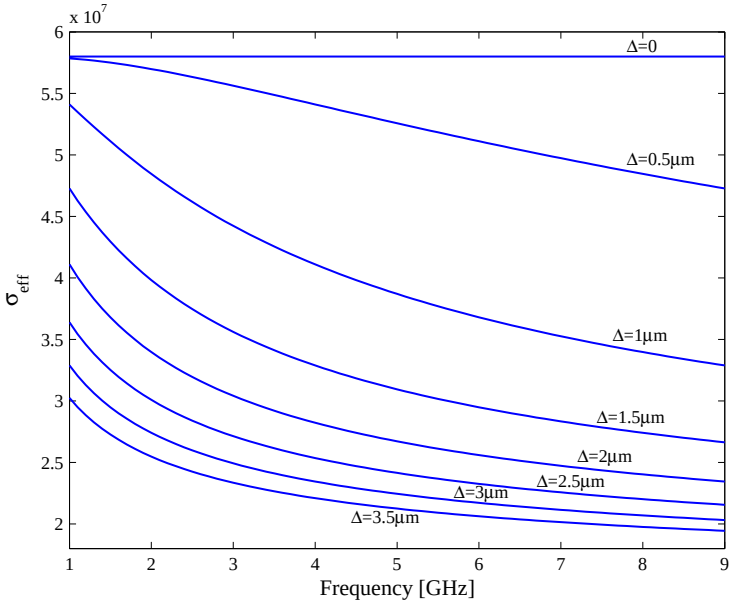

Fig. 2.1. The effective conductivity of copper as a result of surface roughness Δ.

To calculate the conductor losses associated with infinite (unmeshed) ground planes, a different approach is required. By definition, the Green's function formulation for planar layered media incorporates the presence of an electric impedance wall by matching the boundary conditions relating incident and reflected TM- and TE-type plane waves at the layer interface. These ground planes are, however, usually treated as perfect electrical conductors (PEC) where the boundary conditions for the total normal field components are $H_{\text{normal}} = 0$ and $E_{\text{normal}} = 2E_{\text{incident}}$, yielding reflection coefficients of $R^{\text{TE}} = -1$ and $R^{\text{TM}} = 1$ [35].

To include ground plane conductor losses into the model, a transmission line model is introduced where TE-type wave reflection is matched to a voltage reflection coefficient and TM-type wave reflection is matched to a current reflection coefficient.

From transmission line theory [45], the total voltage and current on a line can be written as the sum of incident and reflected waves

$$\begin{aligned} V(z) &= V_0^+ e^{-\gamma z} + V_0^- e^{\gamma z} \\ I(z) &= I_0^+ e^{-\gamma z} + I_0^- e^{\gamma z}, \end{aligned} \tag{2.17}$$

where z is the direction of propagation. Also, the amplitude of the reflected voltage wave normalised to the amplitude of the incident voltage wave, which is known as the voltage reflection coefficient, is given by

$$\Gamma_V = \frac{V_0^-}{V_0^+} = \frac{Z_L - Z_0}{Z_L + Z_0}, \tag{2.18}$$

where Z_0 is the characteristic impedance and Z_L is the load impedance. Similarly, a current reflection coefficient, giving the normalised amplitude of the reflected current wave, can be defined as

$$\Gamma_I = \frac{I_0^-}{I_0^+} = -\frac{Z_L - Z_0}{Z_L + Z_0}, \tag{2.19}$$

which is merely the negative of Γ_V.

Similar to Γ_V and Γ_I, the reflection coefficients R^{TE} and R^{TM} can be computed by choosing suitable values for Z_0 and Z_L. Thus, when setting Z_0 equal to the intrinsic impedance of the medium $\eta_i = \sqrt{\mu_i/\epsilon_i}$, and Z_L equal to the surface impedance Z_s, it follows that

$$\begin{aligned} R^{\mathrm{TE}} &= \frac{Z_s - \eta_i}{Z_s + \eta_i} \\ R^{\mathrm{TM}} &= -\frac{Z_s - \eta_i}{Z_s + \eta_i}. \end{aligned} \tag{2.20}$$

Note that for $Z_s = 0$, the reflection coefficients simplify to $R^{\mathrm{TE}} = -1$ and $R^{\mathrm{TM}} = 1$, which is identical to the lossless PEC case. In the transmission line model, these reflection coefficients correspond to that of a short circuit.

Radiation Losses

By definition, radiation losses are included in the Green's function formulation. When the uppermost (and/or lowermost) region of the problem geometry extends to ∞ and no impedance wall is present at the final discontinuity of the planar interfaces, the reflection coefficients R^{TE} and R^{TM} are both set to zero, thus allowing the plane waves to radiate into open space. When an electric conductor is present, however, the boundary conditions are changed to relate the incident and reflected waves at the layer interface. This condition introduces conductor losses as explained above, while radiation losses are suppressed.

Surface Wave Losses

A point source of current on a metallic patch radiates electromagnetic waves. Some of the waves are diffracted and store magnetic energy, some radiate into space and contribute to the radiation pattern of the patch, while others remain within the dielectric substrate, trapped by the total reflection of the different interfaces. These waves are called surface waves and propagate along a 2D interface, decaying more slowly than space (radiation) waves, which spread out within a 3D space.

Surface waves are a very important factor in the analysis of planar circuits as they reduce the radiation efficiency of a patch and degrade the performances of the resonator [46,47]. It was found that infinite parallel-plate ground planes in the MoM formulation introduce unwanted surface wave modes, which are absent from finite size practical structures. To prevent propagation of such waves, the problem geometry should be bounded by adding vertical metallic/PEC walls to the structure.

2.2 Scattering Parameter Extraction

In the MoM analysis of microstrip circuits, terminating ports with arbitrary loads is a problem addressed by only a few authors [48–50]. Most recently, Liu [50] presented a simple MoM loading technique to deal with an arbitrary load terminating a microstrip line. The loading condition of the microstrip line is equivalent to adding a loading voltage element to the excitation voltage vector in the MoM, and since the loading voltage satisfies Ohm's law, the voltage can be represented by a product of unknown currents and given loads.

In [50], the loading technique was developed for a MoM analysis using rooftop basis functions to represent the unknown current distribution, and rectangular functions as testing functions to obtain a set of linearly independent equations. The technique also assumes that the excitation at each port is modelled by a single half-basis function only. In this section the technique was reformulated for use with the Rao, Wilton and Glisson [33] vector-valued triangular basis functions. In addition, extraction of the circuit S-parameters was introduced, with the model subsequently also supporting multiple half-basis functions at each port.

Basis Functions

Rao, Wilton and Glisson [33] introduced a set of basis functions $\mathbf{f}_n$ suitable for use with the electric field MPIE and triangular patch modelling. Crucial to the construction of such vector basis functions is that their normal components should be continuous across surface edges and that it should be free of fictitious line or point charges. Additionally, each basis function is to be associated with an interior or non-boundary edge of the patch model and is to vanish everywhere except on the two triangles attached to the edge.

With I_n the coefficients to be determined, the electric surface current $\mathbf{J}_s$ at point $\mathbf{r}'$ on the triangulated surfaces may be approximated as

$$\mathbf{J}_s(\mathbf{r}') \approx \sum_{n=1}^{N} I_n \mathbf{f}_n(\mathbf{r}'). \tag{2.21}$$

Here $N = N_1$ where N_1 is the total number of interior edges. An important characteristic of triangular basis functions is that at a given edge, only the basis function associated with that edge has a current component normal to the edge since all other basis currents in adjacent faces are parallel to the edge. Furthermore, since the normal component of $\mathbf{f}_n$ at the n^{th} edge is unity, each coefficient I_n may be interpreted as the normal component of current density flowing past that edge.

At boundary edges, the sum of the normal components of current on opposite sides of the surface are cancelled because of current continuity. These edges are left undefined with no contribution to Eq. 2.21. A different approach is, however, needed to model the flow of induced currents

through a microstrip port edge terminated in an arbitrary load. A special set of half-basis functions is used to ensure continuity of current at these edges. These half-subsections show similar properties to the basis functions defined on interior edges, the difference being that continuity is now achieved between a boundary edge and a non-discretised loading element. To account for these additional currents, Eq. 2.21 is adapted to include $N = N_1 + N_2$ coefficients of which N_2 is the number of port edges.

The physical meaning of the half-basis functions at the loading end is a change in the natural state of the port from an open circuit to a short circuit. An arbitrary load impedance can then easily be connected at this port for numerical simulations. When using half-basis functions at the input source port, the excitation can be regarded as an ideal voltage source having zero internal resistance [50].

Port Boundary Conditions

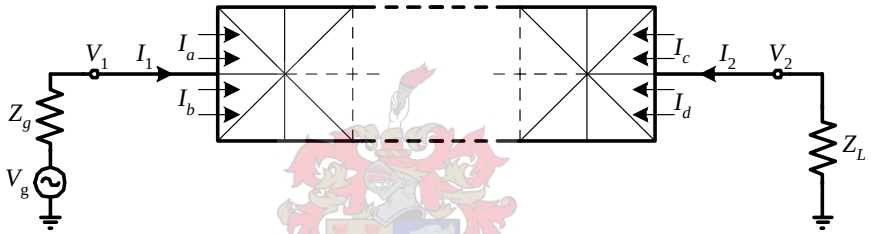

Fig. 2.2. Equivalent circuit and basis functions on a two-port microstrip line.

In Fig. 2.2, port 1 is the excitation source port with an internal impedance Z_g and port 2 is the loading port with a load impedance Z_L. The boundary conditions at these ports are

$$V_1 = V_g - I_1 Z_g \tag{2.22}$$

and

$$V_2 = -I_2 Z_L, \tag{2.23}$$

where V_1 and V_2 are the port voltages and I_1 and I_2 are the total port currents.

Since the total current flowing past an edge is simply the coefficient of current density multiplied by the edge length, and with I_a, I_b, I_c and I_d the components of current density associated with the half-basis functions defining the port edges of length ℓ_a, ℓ_b, ℓ_c and ℓ_d, the total port currents are given by

$$\begin{aligned} I_1 &= I_a \ell_a + I_b \ell_b \\ I_2 &= I_c \ell_c + I_d \ell_d. \end{aligned} \tag{2.24}$$

When assuming a delta-gap source model and using Eq. 2.7 to compute the excitation vector, it can be shown that

$$E_m = < \mathbf{E}_t^i, \mathbf{g}_m > = \int_{T_m^+} \mathbf{E}_t^i \cdot \mathbf{g}_m dS = V_m \ell_m, \tag{2.25}$$

where $\mathbf{E}_t^i$ is a voltage gap source of magnitude V_m. Therefore, a delta-gap source across the m^{th} port edge adds only a single non-zero entry into the excitation vector E_m, the m^{th} element, which is equal to the magnitude of the source V_m multiplied by the edge length ℓ_m.

In Fig. 2.2, port 1 and port 2 are excited by voltages of magnitude V_1 and V_2 respectively. Thus, when substituting Eqs. 2.22 and 2.23, it follows that

$$\begin{aligned} E_a = V_1\ell_a &= (V_g - I_1 Z_g)\ell_a \\ &= (V_g - (I_a\ell_a + I_b\ell_b)Z_g)\ell_a \\ E_b = V_1\ell_b &= (V_g - I_1 Z_g)\ell_b \\ &= (V_g - (I_a\ell_a + I_b\ell_b)Z_g)\ell_b \end{aligned} \tag{2.26}$$

and

$$\begin{aligned} E_c = V_2\ell_c &= -I_2 Z_L\ell_c \\ &= -(I_c\ell_c + I_d\ell_d)Z_L\ell_c \\ E_d = V_2\ell_d &= -I_2 Z_L\ell_d \\ &= -(I_c\ell_c + I_d\ell_d)Z_L\ell_d. \end{aligned} \tag{2.27}$$

With $[Z_{mn}][I_n] = [E_m]$ and E_m given by Eqs. 2.26 and 2.27, a new matrix equation in terms of the original current coefficients I_n is found

$$\left([Z_{mn}] + \begin{bmatrix} 0 & 0 & \cdots & & 0 & \cdots & & 0 \\ 0 & \ddots & & & & & & \\ \vdots & & & & \vdots & & & \vdots \\ & & & 0 & 0 & \cdots & & 0 \\ & & & 0 & l_a l_a Z_g & l_a l_b Z_g & 0 & 0 \\ & & & \vdots & l_b l_a Z_g & l_b l_b Z_g & 0 & 0 \\ 0 & & & & 0 & 0 & l_c l_c Z_L & l_c l_d Z_L \\ 0 & 0 & \cdots & 0 & 0 & 0 & l_d l_c Z_L & l_d l_d Z_L \end{bmatrix} \right) \begin{bmatrix} I_1 \\ I_2 \\ \vdots \\ I_{N_1} \\ I_a \\ I_b \\ I_c \\ I_d \end{bmatrix} = \begin{bmatrix} 0 \\ 0 \\ \vdots \\ 0 \\ l_a V_g \\ l_b V_g \\ 0 \\ 0 \end{bmatrix}. \tag{2.28}$$

Scattering Parameters

Once the approximate distribution of the surface current density is found by solving Eq. 2.28 for the unknown weighting coefficients I_n, scattering parameters for an N-port discontinuity are obtained by examining the current distribution on the ports. In general, N linearly independent excitation schemes are required to evaluate an N-port network.

According to [51], the elements of the scattering matrix $[S]$ can be determined as

$$S_{ij} = \left.\frac{b_i}{a_j}\right|_{a_k=0 \text{ for } k\neq j}, \tag{2.29}$$

where substitution of Eqs. 2.22 and 2.23 for the port voltages give the incident and reflected waves as a function of the port currents (Eq. 2.24)

$$\begin{aligned} a_j &= \frac{V_j + I_j Z_j}{2\sqrt{Z_j}} = \frac{V_g}{2\sqrt{Z_j}} \\ b_i &= \frac{V_i - I_i Z_i}{2\sqrt{Z_i}} = \begin{cases} -I_i\sqrt{Z_i} & i \neq j \\ \dfrac{V_g - 2I_i Z_i}{2\sqrt{Z_i}} & i = j. \end{cases} \end{aligned} \tag{2.30}$$

2.3 Conclusion

In this chapter the Method of Moments formulation has been briefly outlined with the focus on two implementation aspects, namely, the accurate calculation of losses and an efficient S-parameter extraction technique for use with planar structures.

To model losses accurately, each of the loss components (dielectric, conductor, radiation and surface wave losses) has to be treated separately. Ground plane conductor losses were included in the MoM formulation by matching TE- and TM-type wave reflection to transmission line voltage and current reflection coefficients.

S-parameter extraction for Rao, Wilton and Glisson basis functions was implemented by terminating a microstrip line in an arbitrary load impedance. The technique was adapted from a simple method introduced by Liu [50] to compute the currents and voltages at the ports of a microstrip line terminated in an arbitrary load. The technique extended the method of [50] to work with vector-valued basis functions and to support multiple half-basis functions at each port. Finally, the technique allows for easy computation of the S-parameters at each of the network ports.

Chapter 3

One-Dimensional Adaptive Rational Interpolation

Compact rational metamodels are at present widely exploited to characterise the electromagnetic behaviour of microwave circuits in the frequency domain. Several rational interpolation and rational approximation techniques have been proposed to calculate rational functions [17]. In general, the rational analytic model $\Re$ of the complex (frequency) variable $s = \sigma + j2\pi f$ is defined as a ratio of two polynomials $N_\zeta(s)$ and $D_\nu(s)$,

$$\Re(s) = \frac{N_\zeta(s)}{D_\nu(s)} = \frac{\sum_{j=0}^{\zeta} a_j s^j}{\sum_{j=0}^{\nu} b_j s^j}, \tag{3.1}$$

where ζ is the order of the numerator, ν the order of the denominator, and a_j and b_j the polynomial coefficients (b_0 is chosen arbitrarily). The rational interpolant $\Re(s)$ provides an approximation of the system response $H(s)$, which is valid on an interval $[s_0, s_1]$.

When CEM techniques are used for the generation of the support points, it is of the utmost importance to establish a model with the minimum number of electromagnetic evaluations. This can be achieved using adaptive sampling methods where the order of the function is gradually increased until the desired accuracy is reached. The sampling algorithm automatically determines the optimal positions for the support points at which to perform an EM-evaluation, thereby minimising the number of unequally spaced evaluations required to approximate the response accurately [4, 12–14].

In [17], Deschrijver gave an overview and comparison of some univariate rational fitting methods, which are most commonly used to model deterministic, simulation-based data. The paper focused on modelling of S-parameter transfer responses, discussing numerical conditioning and fitting errors. Two metamodelling techniques were identified to be the most successful in gene-

rating univariate rational models of high accuracy, namely, the Thiele-type continued fractions approach [13,15] and the Vector Fitting (VF) pole-residue method [20,52]. Both techniques are suitable for use with an adaptive sampling algorithm since they produce an error estimation in a natural way. This chapter gives a brief description of these two methods.

3.1 Thiele-Type Continued Fractions

The use of continued fractions as rational interpolants in the design of microwave circuits was first proposed in [13]. The rational model (Eq. 3.1) can be represented by a convergent of a Thiele continued fraction [15]

$$\begin{aligned}\Re_k(s) = \frac{N_k(s)}{D_k(s)} &= H_0 + \cfrac{s - s_0}{\varphi_1(s_1, s_0) + \cfrac{s - s_1}{\varphi_2(s_2, s_1, s_0) + \cdots}} \\ &\qquad \cdots + \cfrac{s - s_{k-1}}{\varphi_k(s_k, s_{k-1}, \cdots, s_0)} \\ &= H_0 + \sum_{i=1}^{k} \cfrac{s - s_{i-1}}{\varphi_i(s_i, s_{i-1}, \cdots, s_0)} \qquad k = 0, 1, \cdots, N_s,\end{aligned} \tag{3.2}$$

where each rational expression $\Re_k(s)$ is a k^{th} order partial fraction expansion, showing increasing accuracy as k increases, and reaching a convergent value at $k = N_s$. It is assumed that $\Re(s)$ exists for the function $H(s)$ that is being modelled and a set of $N_s + 1$ support points (s_i, H_i) is required to completely determine $\Re(s)$. The interpolation function can be evaluated numerically with three recurrence relations $N_k(s)$, $D_k(s)$ and φ_k where

$$\begin{aligned}N_k(s) &= \varphi_k(s_k, s_{k-1}, \cdots, s_0)N_{k-1}(s) + (s - s_{k-1})N_{k-2} \qquad k = 2, 3, \cdots, N_s \\ D_k(s) &= \varphi_k(s_k, s_{k-1}, \cdots, s_0)D_{k-1}(s) + (s - s_{k-1})D_{k-2} \qquad k = 2, 3, \cdots, N_s,\end{aligned} \tag{3.3}$$

with initial conditions $N_0(s) = H_0$, $N_1(s) = \varphi_1(s_1, s_0)N_0 + (s - s_0)$, $D_0(s) = 1$ and $D_1(s) = \varphi_1(s_1, s_0)$. The inverse differences φ_k are the partial denominators of Eq. 3.2, and are essentially the polynomial coefficients that define $\Re(s)$. These coefficients are calculated recursively from the support points as

$$\begin{aligned}\varphi_1(s_i, s_0) &\equiv \frac{s_i - s_0}{H_i - H_0} \qquad i = 1, 2, \cdots, N_s \\ \varphi_k(s_i, s_{k-1} \cdots, s_0) &\equiv \frac{s_i - s_{k-1}}{\varphi_{k-1}(s_i, s_{k-2}, \cdots, s_0) - \varphi_{k-1}(s_{k-1}, s_{k-2}, \cdots, s_0)} \\ &\qquad i = k, k+1, \cdots, N_s;\ k = 2, 3, \cdots, N_s.\end{aligned} \tag{3.4}$$

Note that for k even, $\zeta = \nu = k/2$; and for k odd, $\zeta = (k+1)/2$ and $\nu = (k-1)/2$. Once determined, $\Re(s)$ is a curve passing through the support points (s_i, H_i) for $i = 0, 1, 2, \cdots, N_s$.

3.2 Vector Fitting

In [20,52], an accurate and robust algorithm, called Vector Fitting, was introduced to model the frequency domain behaviour of linear time-invariant (LTI) systems by the rational pole-residue expansion

$$\begin{aligned}\Re_k(s) &= \frac{c_1}{s-a_1} + \frac{c_2}{s-a_2} + \cdots + \frac{c_k}{s-a_k} + d \\ &= \sum_{p=1}^{k} \frac{c_p}{s-a_p} + d \qquad\qquad k = P, P+1, \cdots, N_p.\end{aligned} \tag{3.5}$$

Each rational expression $\Re_k(s)$ approximates the measured/simulated data samples H_i at the discrete complex frequencies s_i, $\forall i = 0, \cdots, N_s$. Also, a_p and c_p are the poles and residues respectively, $\forall p = 1, \cdots, k$ and d is a real constant. The Vector Fitting technique linearises the non-linear identification problem by fixing the denominator poles. Starting with an initial guess of $k = P$ poles, the VF algorithm converges towards a global broadband model by relocating the poles in an iterative way. The unknown system variables are estimated by solving two consecutive linear least-squares fits, and it is ensured that the poles and residues are either real or occur in complex conjugate pairs [20]. To improve the accuracy of $\Re_k(s)$, the number of poles k is increased, reaching a convergent value at $k = N_p$.

Instead of fitting $\Re(s)$ directly, the 'weighted' spectral behaviour of the LTI system (Eq. 3.5 multiplied with an unknown rational function $\vartheta(s)$) is approximated. Assuming that both $\vartheta(s)\Re(s)$ and $\vartheta(s)$ can be approximated by rational functions using the same set of poles $\bar{a}_p$, it follows that

$$\begin{bmatrix} (\vartheta\Re)_{\text{fit}}(s) \\ \vartheta_{\text{fit}}(s) \end{bmatrix} = \begin{bmatrix} \sum_{p=1}^{N_p} \frac{c_p}{s-\bar{a}_p} + d \\ \sum_{p=1}^{N_p} \frac{\tilde{c}_p}{s-\bar{a}_p} + 1 \end{bmatrix}. \tag{3.6}$$

The problem can be linearised as a function of the unknowns c_p, d and $\tilde{c}_p$ (the poles $\bar{a}_p$ are fixed beforehand) by multiplying the second row of the vector equation with $\Re(s)$, and equating the first and second rows $(\vartheta\Re)_{\text{fit}}(s) = \vartheta_{\text{fit}}(s)\Re(s)$. Since $\Re(s_i)$ should equal $H(s_i)$ for all frequency samples, an overdetermined system of equations of the form $\mathbf{Ax} = \mathbf{b}$ is found, which can be solved using classical least-squares techniques.

After parameterisation of the rational model, both $(\vartheta\Re)_{\text{fit}}(s)$ and $\vartheta_{\text{fit}}(s)$ can be written as a function of their poles and zeros

$$\begin{bmatrix} (\vartheta\Re)_{\text{fit}}(s) \\ \vartheta_{\text{fit}}(s) \end{bmatrix} = \begin{bmatrix} \frac{\prod_{p=1}^{N_p}(s-z_p)}{\prod_{p=1}^{N_p}(s-\bar{a}_p)} \\ \frac{\prod_{p=1}^{N_p}(s-\tilde{z}_p)}{\prod_{p=1}^{N_p}(s-\bar{a}_p)} \end{bmatrix}. \tag{3.7}$$

From Eq. 3.7, $\Re(s)$ can be calculated as

$$\Re(s) = \frac{(\vartheta\Re)_{\text{fit}}(s)}{\vartheta_{\text{fit}}(s)} = \frac{\prod_{p=1}^{N_p}(s - z_p)}{\prod_{p=1}^{N_p}(s - \tilde{z}_p)}. \tag{3.8}$$

Note that the initial poles are cancelled out and that the zeros of $\vartheta_{\text{fit}}(s)$ become the poles of the approximation $\Re(s)$. The zeros of $\vartheta_{\text{fit}}(s)$ are calculated by an input/output interchange from its state equations [20, 53]. To calculate the residues of $\Re(s)$, Eq. 3.5 is solved as a least-squares problem with the zeros of $\vartheta_{\text{fit}}(s)$ as the new poles of $\Re(s)$ and the now unknown parameters c_p and d.

The above procedure can be applied in an iterative fashion with the poles found in the last iteration used as the new starting poles in order for the method to converge, i.e. $\vartheta_{\text{fit}}(s) \approx 1$, and the poles $\bar{a}_p$ become close enough to the actual poles of $\Re(s)$. A detailed analysis of the significance of the starting pole locations can be found in [20, 54].

3.3 Error Estimation and Adaptive Sampling

In general, a rational interpolant $\Re(s)$ can be found that accurately models a microwave structure over the interval $[s_0, s_1]$, provided that enough support points are used. Although this method can be useful when the data is inexpensive to simulate, it can be computationally expensive and resource demanding when the simulation of data samples is costly. Reducing the spectral density of the data samples becomes an option when the data behaves smoothly. However, a higher model accuracy with even fewer samples is obtained when using adaptive sampling techniques. Adaptive sampling automatically determines the optimal positions for the support points at which to perform an EM-evaluation, thereby minimising the number of evaluations required to approximate the response accurately. In addition, it does not require any *a priori* knowledge of the dynamics of the function being modelled [12, 13].

Both the Thiele-type and Vector Fitting metamodelling techniques are suitable for use with an adaptive sampling algorithm, since both formulations work for unequally spaced support points and both techniques allow for a suitable means of error estimation. For the modelling of functions with more than one complex output parameter, the interpolation model consists of a set of N_e interpolants (sharing the same set of support points), where each interpolant $\Re_k^{(e)}(s)$ models one of the output parameters. Thus, following from the interpolant formulations, a natural residual term emerges as the normalised difference between two approximating functions of different order

$$E_k(s) = \max\left(\frac{|\Re_k^{(e)}(s) - \Re_{k-1}^{(e)}(s)|}{1 + |\Re_k^{(e)}(s)|}\right) \qquad e = 1, 2, \cdots, N_e, \tag{3.9}$$

which provides an estimate of the maximum interpolation error over the interval of interest.

The procedure by which the adaptive sampling algorithm works is as follows[§]—As a first step, support points s_0, s_1, and an arbitrary third support point s_2 in the interval $[s_0, s_1]$ are chosen. The values of H_k at the points s_k are determined by a CEM analysis. Then, by using either the Thiele or VF formulations, the residual $E_k(s)$ is evaluated at a large number of equi-spaced sample points over the interval. At the maximum of the evaluated residual a new support point (s_{k+1}, H_{k+1}) is chosen and the procedure is repeated until the estimated error has been reduced to a sufficiently low value. Upon termination, every interpolant $\Re_k^{(e)}(s)$ will satisfy the convergence criterion.

3.4 Conclusion

In this chapter one-dimensional adaptive rational interpolation has been introduced by means of a detailed discussion on the formulation of two models, namely, the Thiele-type continued fraction approach and the Vector Fitting method.

The above-mentioned techniques proved to be the most useful in generating rational models of high accuracy, and were therefore used in the application of univariate rational interpolation to the problem of accurately predicting resonator characteristics. This is the topic of Chapters 4 and 5, with the focus in Chapter 4 on the calculation of resonance frequencies and in Chapter 5 on the calculation of Q-factors.

[§]For a detailed exposition on the implementation of the adaptive sampling algorithm, see [13, 15].

Chapter 4

Calculation of Resonant Frequencies

The efficient and accurate prediction of the resonant frequencies of microwave resonators is of paramount importance to designers of microwave filters and oscillators. Precision-calculation of this parameter f_0 using computational electromagnetic analysis (CEM) is however not trivial, and standard techniques normally require analysis of a given structure using a high number of frequency points. Adaptively sampled interpolation models can dramatically reduce the computational cost of analyses, and can provide efficient and highly accurate models for microwave structures. Present implementations focus mainly on the modelling of responses such as S-parameters [4, 13], however, and not on the derived parameters of f_0 and Q that are of prime importance to designers of microwave resonators.

This chapter presents two techniques for the extraction of f_0 from a full-wave Method of Moments (MoM) analysis, through the fitting of adaptive rational models to highly resonant structures. The first approach is based on the solution of an eigenmode problem (i.e. a resonator without ports), while the second method uses the S-parameter response of a resonator coupled to input and output loads. As an example of a resonant structure, the well-documented microwave ring resonator will be used to discuss the techniques and verify all results obtained.

For the unloaded problem (Section 4.1), the CEM solution entails finding the zeros of the eigenvalue equation, $\det[Z(s)] = 0$. Conveniently, a pole-free approximation to the roots of this function is possible when using the numerator of a rational interpolation formulation. Numerical difficulties and the existence of improper solutions to the eigenmode function are discussed, and convergence effects due to finite meshing are investigated by varying the maximum discretisation size and the interpolant termination error. Also, the systematic inclusion of different components of loss in the model and the accurate prediction of higher-order resonances are investigated and compared to current techniques.

For the loaded problem (Section 4.2), an algorithm for the extraction of the resonant frequencies from a rational approximation of the scattering parameter magnitude plot is developed, and

results are compared to predictions obtained from measurements and commercial software simulations. Correctness of the interpolation function, as well as asymmetries in the discretisation causing mode splitting are also discussed.

4.1 Calculation of Resonant Frequencies by Solution of the Natural Frequencies of an Unloaded Resonator

As the microwave ring resonator is the test resonator used to discuss and verify techniques presented in this dissertation, this section starts with a brief overview of the most common models used to calculate the resonance frequencies of the ring structure. This is followed by advances made in the field of numerical modelling, specifically related to the prediction of resonance frequencies.

The simplest model of a ring resonator, the straight-line approximation, was first introduced in 1969 by Troughton [55] to measure propagation constants in microstrip, and is based on the principle that resonance is established when the mean circumference of the ring is equal to an integral multiple of wavelengths. This may be expressed as

$$2\pi R = n\lambda_g \qquad \text{for } n = 1, 2, 3, \cdots, \tag{4.1}$$

where R is the mean radius of the ring, λ_g is the guided wavelength, and n is the azimuthal mode number. Since λ_g is frequency dependent, the resonant frequencies for different modes can be calculated using

$$\omega_0 = 2\pi f_0 = \frac{nc}{R\sqrt{\epsilon_{r,\text{eff}}}}, \tag{4.2}$$

where c is the speed of light in free space, and $\epsilon_{r,\text{eff}}$ is the static effective relative dielectric constant. The proposed simple solution only predicts the TM_{n10} modes that exist when the width of the ring is narrow and does not explain the effects of curvature on the resonant frequency for ring widths of small impedance.

In 1971 Wolff and Knoppik [56] presented the first field analysis description of a microstrip ring resonator based on a radial waveguide model. This magnetic-wall model method approximates the ring as a cavity resonator with electric walls on the top and bottom and magnetic walls on the sides (Fig. 4.1). It is assumed that there is no z-dependency ($\partial/\partial z = 0$) and that the fields are transverse magnetic (TM) to the z direction. By taking a solution of Maxwell's equations in cylindrical coordinates and applying boundary conditions at R_i and R_o, the respective inner and outer radii of the ring, the eigenvalue equation is

$$J_n'(kR_o)N_n'(kR_i) - J_n'(kR_i)N_n'(kR_o) = 0, \tag{4.3}$$

where k is the wave number, J_n is a Bessel function of the first kind of order n and N_n is a

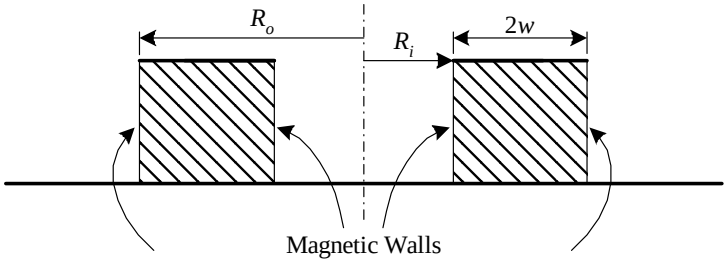

Fig. 4.1. Cross section of the magnetic-wall model of a microstrip ring resonator.

Bessel function of the second kind and order n. J'_n and N'_n are the derivatives of the Bessel functions with respect to the argument kR.

By solving for the roots of this characteristic equation, the resonant frequencies can be found and full mode charts can be generated, such as presented by Wu and Rosenbaum [57]. Fig. 4.2 shows the solution set where the resonant frequencies of the various $\mathrm{TM}_{nm\ell}$ modes are a function of the ring line width ($2w$). Here n is the azimuthal mode number, m is the root number for each n and $\ell = 0$, since $\partial/\partial z = 0$. As the normalised ring width (w/R) is increased, higher-order modes are excited. These higher-order modes are often quite closely spaced in frequency, which may cause difficulty in successfully predicting resonator characteristics such as the quality factor.

The magnetic-wall model eliminates the error due to the mean radius straight-line approximation

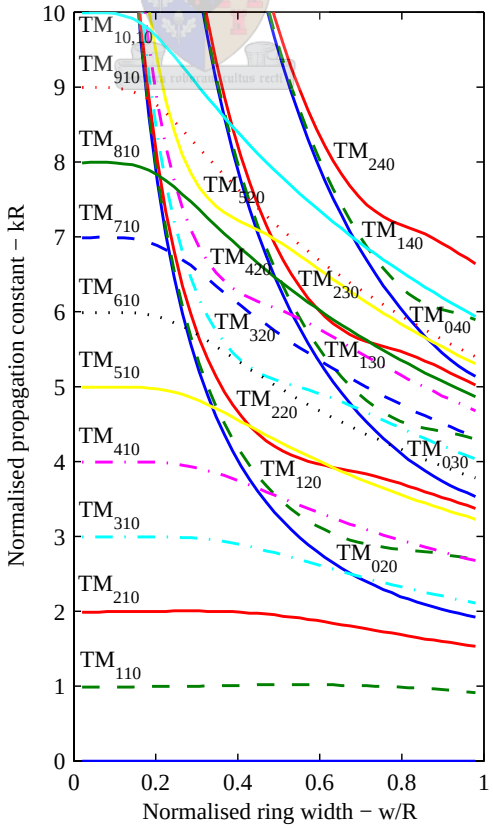

Fig. 4.2. Mode chart of a microstrip ring resonator using the magnetic-wall model.

(Eq. 4.2) and includes the effect of curvature of the microstrip line. Wolff and Knoppik [56] found that the influence of curvature becomes significant when the ring widths become large and the mean radius is not well-defined. If rings of small diameter are used, the effects become even more dramatic due to the increased curvature. Using the magnetic-wall model it can also be shown that the microstrip ring resonator supports two degenerate orthogonal modes that coexist independently of each other [58]. The main drawback of the model is that it does not take into account the fringing edge fields or dispersive effects of the microstrip line.

In 1976 Owens [59] introduced an improvement on the magnetic-wall model. In this approach the relative permittivity of the substrate is equated to a frequency-dependent effective relative permittivity $\epsilon_{r,\text{eff}}(f)$ [60]; and the planar waveguide model is used to calculate a frequency-dependent effective line width $w_{\text{eff}}(f)$ for the parallel conducting plates [59], [61] and [45, p. 162]. To apply the planar waveguide model to the ring resonator, the inner and outer radii of the ring are adjusted to [62]

$$\begin{aligned} R_i &\leftarrow R_i - 0.5\big(w_{\text{eff}}(f) - 2w\big)\frac{R_i}{R_o} \\ R_o &\leftarrow R_o + 0.5\big(w_{\text{eff}}(f) - 2w\big), \end{aligned} \tag{4.4}$$

where the new model imposes the condition $R_i \geq 0$. The improved model is capable of predicting resonant frequencies with an accuracy of 0.2%.

Since 1990, full-wave electromagnetic (EM) analysis methods have been utilised to solve for the natural frequencies of closed structures in the absence of excitation [63, 64]. For many EM-techniques, this requires solution of Eq. 4.5

$$\Re(s) = \det[Z(s)] = 0, \tag{4.5}$$

where $s_i = \sigma_i + j2\pi f_i$ and i indicates the i^{th} solution. This function can be extremely non-linear with an infinite number of solutions, interspersed with an infinite number of poles. In addition, very sharp non-zero local minima are often encountered. Together, this combination of characteristics normally requires an EM-evaluation of the structure at a very high number of closely-spaced frequencies over any given interval. This is computationally very expensive, and still often misses sharp resonances in high-Q structures. In an attempt to trivialise this problem a number of formulations have been reported—pole-free formulations [65], the use of a singular-value decomposition method (SVD) [66], finding the pole-positions analytically, either removing them [67] or searching in-between them [68], and the use of adaptive rational models, the latter providing a very efficient solution to this problem, as models are constructed using very small sets of support points.

In 2001, Lehmensiek [16] proposed a model-based parameter estimation technique based on a Thiele-type continued fraction rational interpolation formulation and a Method of Lines (MoL) analysis, to provide an accurate pole-free approximation to the roots of $\Re(s)$ and to calculate

the propagation constants of modes in quasi-TEM microwave structures. A Newton-Raphson method utilising a zero-suppression technique was used to find the roots of $\Re(s)$. This technique is most useful, since the resulting approximation can be written as a ratio of two polynomials and thus only the numerator needs to be solved to find the zeros of the function. Using this technique together with a MoM analysis does, however, present a few problems.

Firstly, MoM solutions create unique numerical problems when evaluating the expression $\det[Z(s)]$, [25, 26]. Function values are extremely small while differing by orders of magnitude from the start to the end of the frequency interval. To solve this, a frequency-dependent scaling constant was developed to adjust the determinant function to values of a similar order of magnitude across the complete frequency interval.

Secondly, the Thiele fitting function interpolates support points exactly and is incapable of compensating for noise in the data. When a low interpolation error and smooth fit is required, longer computational times and oversampling may result. Root-finding as proposed by Lehmensiek [16] is based on an iterative search algorithm, which can potentially miss one or more roots. To improve on these shortcomings, the application of Vector Fitting (VF) to the problem of the natural frequencies of an unloaded planar ring resonator from a full-wave MoM analysis is investigated, and compared to the approach by Lehmensiek when applied to the same structure. In the latter approach, the Newton-Raphson method used by [16] is replaced by a root-finding algorithm, which computes the roots of the polynomial form of the continued fraction model by constructing an upper-Hessenberg matrix, which is significantly faster than the Newton-Raphson algorithm. Vector Fitting can be applied to least-squares solutions where the data may be contaminated with noise. The Vector Fitting formulation iteratively relocates its poles by calculating the zeros of a rational scalar function $\vartheta(s)$. Using the VF equivalent state equation representation (SER), Gustavsen [20,53] has shown that these zeros can easily be calculated as the eigenvalues of a combination of the state matrices. This technique of root-finding has never been applied to the problem of microwave resonators and the theory was extended to also calculate the roots of the VF interpolant $\Re(s)$, [27].

Two experimental studies are presented to support the theory. In the first study the two modelling approaches are compared by analysing an unloaded microstrip ring resonator to predict the resonance frequencies. Convergence effects due to finite meshing are investigated by varying the maximum discretisation size and the interpolation error, the existence of different classes of roots are explained, and the usefullness of each technique is discussed giving advantages and disadvantages. In the second study the Thiele and VF models are tested against the straight-line approximation, the different magnetic-wall models and commercial software, to compare accuracy in the predictions, model capabilities (inclusion of loss components), and the successful prediction of higher-order resonances for ring widths of low impedance.

4.1.1 Evaluation of det[Z(s)] [26]

The MoM approach to solving Eq. 4.5 leads to the numerical problem that the $\det[Z(s)]$ evaluates to extremely small values, which also vary by orders of magnitude over frequency. Standard determinant functions are unable to accurately evaluate to such small values and to ensure an accurate fit, a frequency-dependent scaling constant is introduced to adjust the determinant function to values of a similar order of magnitude.

Calculation of this scaling factor sf, over the frequency interval $[s_0, s_1]$, relies on an alternative algorithm for the evaluation of the $\det[Z(s)]$. Based on the LU factorisation of the Z-matrix, and using an IMSL Fortran 90 library routine (dlfdcg[†]), the determinant is returned in the useful form [69]

$$\det[Z(s_k)] = \det_{1,s_k} \times 10^{\det_{2,s_k}} \tag{4.6}$$

where $\det_1$ is a complex scalar containing the mantissa of the determinant and $\det_2$ is a scalar containing the exponent of the determinant. The value of $\det_1$ is normalised so that either $1 \leq |\det_1| < 10$ or $\det_1 = 0$.

To adjust the magnitude for equal values at the start and end of the frequency interval, set

$$\begin{aligned} |\det[Z(s_0)]| \times (s_0)^{sf} &\approx |\det[Z(s_1)]| \times (s_1)^{sf} \\ \Rightarrow |\det_{1,s_0}| \times 10^{\det_{2,s_0}} \times (s_0)^{sf} &\approx |\det_{1,s_1}| \times 10^{\det_{2,s_1}} \times (s_1)^{sf}, \end{aligned} \tag{4.7}$$

and presuming that $|\det_{1,s_0} / \det_{1,s_1}| \approx 1$, it follows that

$$sf = \frac{\det_{2,s_0} - \det_{2,s_1}}{\log\left(\frac{s_1}{s_0}\right)} \tag{4.8}$$

and

$$\underset{\text{(scaled)}}{\det}[Z(s_k)] = \det_{1,s_k} \times 10^{\det_{2,s_k}} \times (s_k)^{sf}. \tag{4.9}$$

Since scaling has no effect on the position of the roots of a function, this is a perfectly viable option.

However, the multiplication of two extreme values as used in Eq. 4.9 leads to numerical ill-conditioning. To ensure an increase in accuracy, the transformation

$$(s_k)^{sf} = p \times 10^q \tag{4.10}$$

is required where the value of p is chosen consistent with scientific notation, i.e. $1 \leq p < 10$.

By taking the logarithm of Eq. 4.10, and since $\log(p) < 1$, it follows that

$$q = \lfloor sf \times \log(s_k) \rfloor, \tag{4.11}$$

[†]dlfdcg—computes the determinant of a complex general matrix given the LU factorization of the matrix.

and thus

$$p = 10^{(sf \times \log(s_k) - q)}. \tag{4.12}$$

Finally, Eq. 4.9 reduces to

$$\det_{(\text{scaled})}[Z(s_k)] = \det_{1,s_k} \times p \times 10^{(\det_{2,s_k} + q + t)}, \tag{4.13}$$

where t is chosen to normalise the exponent term $(\det_2 + q + t)|_{s=s_0}$ to zero.

Fig. 4.3 shows a plot of the real and imaginary parts of a scaled interpolant. The resonance frequencies are found where both the real and imaginary parts are zero, which for this example yields two natural pairs of frequencies in the region of 2.02 GHz for the TM_{110} mode and 4.02 GHz for the TM_{210} mode. Without scaling, the determinant evaluated to $(-3.5245 - j0.1193) \times 10^{-1031}$ at 1 GHz and $(-1.7672 - j0.1808) \times 10^{-1190}$ at 5 GHz. These values differ by orders of magnitude (10^{159}) and yet both function values numerically have a zero magnitude. To accurately identify the actual zeros or resonance frequencies of the determinant function within such a range of values, scaling of the determinant is absolutely essential.

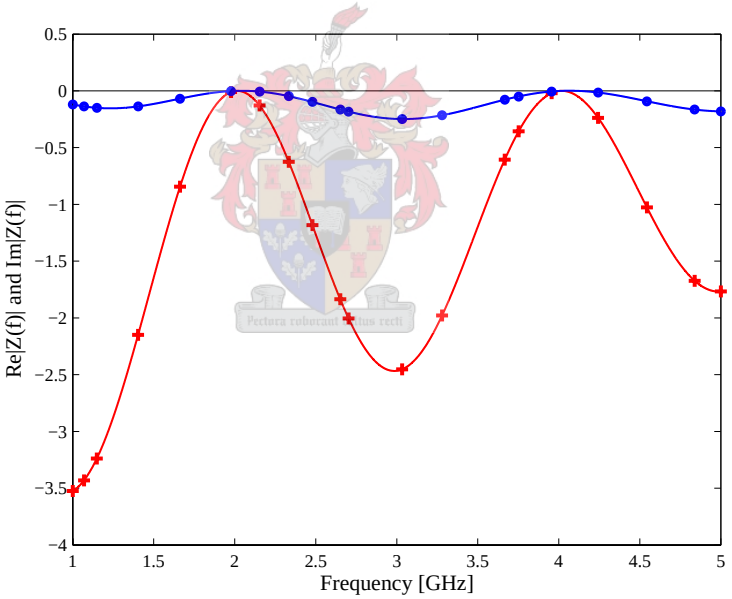

Fig. 4.3. Real (red) and imaginary (blue) parts of a scaled interpolant.

4.1.2 Calculation of Zeros [27]

Thiele Continued Fractions

Since the approximation of $\Re(s)$ can be written as a ratio of two polynomials, only the numerator, which is pole-free by nature, needs to be solved to calculate the zeros of the function.

As a first root-finding algorithm, the first-order Newton-Raphson method used by Lehmensiek [16]

$$s_{m+1} = s_m - \alpha \frac{N(s_m)}{N'(s_m)} \tag{4.14}$$

is applied to the numerator model of $\Re(s)$.

In this method, root-finding is based on the direct evaluation of the Thiele representation. The numerator of the rational polynomial $N_k(s)$ can easily be calculated from Eq. 3.3. Favourable when using gradient root-finding algorithms, the derivative of the numerator is also an analytic function and can be calculated from

$$\frac{\partial N_k(s)}{\partial s} = \varphi_k(s_k, s_{k-1}, \cdots, s_0)\frac{\partial N_{k-1}(s)}{\partial s} + (s - s_{k-1})\frac{\partial N_{k-2}(s)}{\partial s} + N_{k-2}(s). \tag{4.15}$$

Furthermore, evaluation of both the numerator and its derivative are computationally efficient and inexpensive tasks.

As an iterative method, the Newton-Raphson algorithm can easily reconverge to a previously calculated root. Therefore, the zero-suppression technique [70] is used to prevent the root-finding algorithm from calculating the same root twice. This technique requires that the derivative used in Eq. 4.14 be transformed to

$$N'(s) \leftarrow \frac{\partial N(s)}{\partial s} - \sum_{i=1}^{N_\mathrm{r}} \frac{N(s)}{s - \xi_i}, \tag{4.16}$$

where ξ_i are the N_r previously found roots. The advantage of this method, as opposed to deflation, where the polynomial $N(s)$ is divided by $s - \xi_i$ explicitly to give a polynomial of lower order, is that the accuracy of a new root is not sensitive to the errors incurred in calculating the previous roots.

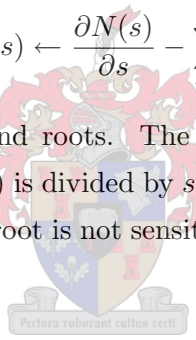

The Newton-Raphson method used by [16], while accurate, is however quite slow and can still easily become trapped in local minima. Instead, the roots of the polynomial representation of the numerator model of $\Re(s)$ are computed. While being slightly less accurate for high orders of the approximating functions, it is significantly faster. Devising recurrence formulae for Eq. 3.3, $N_k(s)$ can be transformed to a polynomial of the form

$$N_k(s) = a_0^{(k)} + a_1^{(k)}s + a_2^{(k)}s^2 + \cdots + a_\zeta^{(k)}s^\zeta, \tag{4.17}$$

where

$$\begin{aligned} a_0^{(k)} &= \varphi_k(s_k, s_{k-1}, \cdots, s_0)a_0^{(k-1)} - s_{k-1}a_0^{(k-2)} \\ a_i^{(k)} &= \varphi_k(s_k, s_{k-1}, \cdots, s_0)a_i^{(k-1)} - s_{k-1}a_i^{(k-2)} + a_{i-1}^{(k-2)} \qquad k = 2, 3, \cdots, N; \\ &\qquad\qquad\qquad\qquad\qquad\qquad\qquad\qquad\qquad\qquad i = 1, 2, \cdots, \zeta, \end{aligned} \tag{4.18}$$

with initial values $a_0^{(0)} = H_0$, $a_i^{(0)} = 0$ for $i = 1, 2, \cdots, \zeta$; $a_0^{(1)} = \varphi_1(s_1, s_0)a_0^{(0)} - s_0$, $a_1^{(1)} = 1$ and $a_i^{(1)} = 0$ for $i = 2, 3, \cdots, \zeta$. Following from the continued fraction formulation, the numerator order is $\zeta = \lfloor (k+1)/2 \rfloor$.

Equivalently, Eq. 4.17 with $a_{\zeta}^{(k)} = 1$ can be reconstructed into the determinant of an upper-Hessenberg matrix as

$$N_k(s) = \det \begin{bmatrix} s & 0 & 0 & \cdot & \cdot & 0 & 0 & (-1)^{\zeta-1}a_0^{(k)} \\ 1 & s & 0 & 0 & \cdot & \cdot & 0 & (-1)^{\zeta-2}a_1^{(k)} \\ 0 & 1 & s & 0 & \cdot & \cdot & \cdot & (-1)^{\zeta-3}a_2^{(k)} \\ \cdot & 0 & 1 & \cdot & \cdot & \cdot & \cdot & \cdot \\ \cdot & \cdot & \cdot & \cdot & \cdot & 0 & 0 & \cdot \\ 0 & \cdot & \cdot & \cdot & 1 & s & 0 & (-1)^{2}a_{\zeta-3}^{(k)} \\ 0 & 0 & \cdot & \cdot & 0 & 1 & s & (-1)^{1}a_{\zeta-2}^{(k)} \\ 0 & 0 & 0 & \cdot & \cdot & 0 & 1 & s + a_{\zeta-1}^{(k)} \end{bmatrix}, \tag{4.19}$$

or in matrix form

$$N_k(s) = \det[s\mathbf{I} - \tilde{\mathbf{A}}]. \tag{4.20}$$

Finding the roots of a polynomial in this form is a trivial problem where the zeros of the polynomial $N_k(s)$ are computed as the eigenvalues of matrix $\tilde{\mathbf{A}}$.

To ensure that the root positions of $\Re(s)$ are accurate and that $\Re(s)$ does not miss any roots, a high accuracy in the model is required. This demand on accuracy can cause the sampling algorithm to produce pole-zero combinations, with the result that more zeros are calculated than the sought-after number of $j\omega$-axis zeros describing the characteristic equation (Eq. 4.5). Therefore, the validity of all zeros are checked against the roots of the denominator, eliminating all zeros that are within 0.003 absolute distance to a pole. The roots of the polynomial equivalent of the denominator are computed by using the recurrence relations of Eq. 4.18 with the order equal to $\nu = \lfloor k/2 \rfloor$ and the initial conditions $a_0^{(0)} = 1$, $a_0^{(1)} = \varphi_1(s_1, s_0)$ and $a_i^{(k)} = 0$ for $i = 1, 2, \cdots, \nu$; $k = 0, 1$.

Vector Fitting

The Vector Fitting formulation lends itself to an elegant method for finding the zeros (and poles) of the model $\Re(s)$. Since VF by pole relocation requires calculation of the zeros of $\vartheta(s)$ by means of an input/output interchange from its state equation [20], it is possible to exploit this procedure to also find the zeros of $\Re(s)$.

In VF, it is well-known that Eq. 3.5 can be directly converted into the form

$$\mathbf{R}(s) = \frac{\mathbf{y}(s)}{\mathbf{u}(s)} = \mathbf{C}(s\mathbf{I} - \mathbf{A})^{-1}\mathbf{B} + \mathbf{D}, \tag{4.21}$$

where $\mathbf{R}(s)$ is the transfer response matrix, and $\mathbf{A}$, $\mathbf{B}$, $\mathbf{C}$ and $\mathbf{D}$ are the state space matrices for a low-order state equation approximation [52]. Matrix $\mathbf{A}$ is a diagonal matrix containing the final poles a_p, $\mathbf{B}$ is a column vector of ones, $\mathbf{C}$ is a row vector containing the residues c_p and $\mathbf{D}$ is the real constant d.

Now, the roots of $\Re(s)$ are found where the output parameter $y(s)$ is zero. To establish a relation, return to the time domain state equations of Eq. 4.21

$$\begin{aligned} \dot{x} &= \mathbf{A}x + \mathbf{B}u \\ y &= \mathbf{C}x + \mathbf{D}u. \end{aligned} \tag{4.22}$$

By eliminating u from Eq. 4.22 and choosing $y = 0$, it follows that

$$\begin{aligned} \dot{x} &= \mathbf{A}x + \mathbf{B}\mathbf{D}^{-1}(y - \mathbf{C}x) \\ &= (\mathbf{A} - \mathbf{B}\mathbf{D}^{-1}\mathbf{C})x, \end{aligned} \tag{4.23}$$

which corresponds to solving the eigenproblem $\tilde{\mathbf{A}}\mathbf{x} = s\mathbf{x}$. It follows that the zeros of $\Re(s)$ are the eigenvalues of $\tilde{\mathbf{A}} = \mathbf{A} - \mathbf{B}\mathbf{D}^{-1}\mathbf{C}$.[‡]

Note that in the case of a complex pair of poles, the submatrices in $\tilde{\mathbf{A}}$ should be modified via a similarity transform to ensure that $\tilde{\mathbf{A}}$ becomes a real matrix and its complex eigenvalues come out as perfect complex conjugate pairs [20].

No additional computation is required to find the poles of $\Re(s)$ as they correspond to the diagonal elements of matrix $\mathbf{A}$, i.e the values a_p.

4.1.3 Study 1—Investigation of the Effect of MoM Discretisation

The use of MoM introduces several accuracy and convergence effects due to finite meshing of the structure. Finer discretisations yield accurate results at the expense of computational time, while a coarser mesh solves more quickly, however, numerical defects such as noise and oversampling can no longer be ignored. This study investigates mesh related issues surrounding the prediction of the resonance frequencies of an unloaded microstrip ring resonator. This is achieved by finding a compromise between the mesh fineness (computational time) and the termination error (number of support points) of the interpolation problem. The use of both Vector Fitting and Thiele continued fractions as rational models, and root-finding by iterative and direct solution are investigated.

The experimental setup was selected to support fundamental TM_{n10} modes only. As this study focuses primarily on issues surrounding the identification of resonance frequencies and not on the accuracy of the actual roots as such, there is no need to model a more complex lower impedance ring that would also include closely-spaced higher-order modes. The selected resonant structure consists of an unloaded lossy microstrip ring resonator with mean ring radius $R = 16.9$ mm and a normalised ring width $w/R = 0.1$. The substrate (Taconic TLY-5) has a relative permittivity of $\epsilon_r = 2.2$, a dissipation factor of $\tan(\delta) = 0.0009$ and a thickness of $h = 0.508$ mm. Several

[‡]In $\vartheta(s)$, $\mathbf{D} = 1$ and the zeros of $\vartheta(s)$ are calculated as the eigenvalues of the matrix $\mathbf{A} - \mathbf{B}\mathbf{C}$. This was shown in [20, 53].

computer simulations were performed in the range [1 GHz, 9 GHz]. The structure is expected to have four degenerate pairs of resonant frequencies in the given band. For the calculation of the natural frequencies of this resonator, the maximum discretisation size L was set to a fraction of the free-space wavelength at 5 GHz and 9 GHz respectively; and the interpolation error was estimated using a residual term that emerged from the rational fitting methods as

$$E_k(s) = \frac{|\Re_k(s) - \Re_{k-1}(s)|}{1 + |\Re_k(s)|}, \tag{4.24}$$

which provides a relative error between the current estimate of the interpolant and the previous estimate, i.e. before adding the last support point. Simulation results were obtained for a variety of discretisations, including $\lambda/10$, $\lambda/15$, $\lambda/20$, $\lambda/25$, $\lambda/30$ and $\lambda/35$. For discussion, Table 4.1 shows the results for the $\lambda/15$ and $\lambda/35$ meshings of this experiment, where the 'Interpolation Error' refers to the maximum value E_k in the frequency interval, obtained by the number of support points shown in brackets. For the Thiele-type approach, both the Newton-Raphson and the proposed polynomial root-finding techniques were implemented, and the SER eigenvalue approach was implemented for the Vector Fitting method. A number of interesting characteristics emerged from this study, as discussed below.

Mesh Related Issues

i) Most CEM techniques calculate two slightly different f_0's for each degenerate resonance pair. For this example, the first four natural pairs of frequencies were found in the region of 2.02 GHz, 4.02 GHz, 6.03 GHz and 8.02 GHz. Fig. 4.4 shows the different meshings ($\lambda/15$ and $\lambda/35$) with the calculated current distribution at first resonance.

ii) As the mesh is refined and a higher accuracy in the model is required, the resonance frequencies decrease in value and the dual frequencies converge to a numerically single value.

iii) A reduction in the order of the fitting functions can be observed as the mesh is refined. This is due to the reduction in numerical noise with increasing mesh refinement, and is far more pronounced in the Thiele approach, as this approach interpolates the support points exactly.

iv) The different root-finding methods predicted the roots to within 0.04% error.

Accuracy and Pole-Zero Issues

The comparison between the Thiele continued fraction and the Vector Fitting techniques has shown that the fitting errors are comparable and highly accurate. However, if the mesh is too coarse, the models can differ substantially from the actual response. Due to the interpolating nature of the Thiele fitting function, which passes through the support samples, a high number of samples is required to ensure a low interpolation error and smooth fit. This inability to compensate for numerical noise means longer computational times, but more importantly, may lead to oversampling. Vector Fitting, however, can be applied to least-squares solutions, where

TABLE 4.1
Comparison of the roots calculated by using different methods to model and predict the resonance frequencies of an unloaded lossy microstrip ring resonator. All roots are presented in the complex frequency plane ($s/(2\pi) = \sigma/(2\pi) + jf) \times 10^9$. ($L$ = Maximum Discretisation Size; E_k = Interpolation Error; Substrate parameters for Taconic TLY-5: $h = 0.508$ mm, $\epsilon_r = 2.2$, $\tan(\delta) = 0.0009$; Ring parameters: $R = 16.9$ mm, $w/R = 0.1$)

(a) Frequency Range [1 GHz, 5 GHz].

Interpolation Error (E_k)	Class of Zeros	Thiele Continued Fraction: Newton-Raphson Method		Thiele Continued Fraction: Polynomial Method		Vector Fitting: SER Eigenvalue Method	
		$L < \lambda/15$ 54 triangles	$L < \lambda/35$ 303 triangles	$L < \lambda/15$ 54 triangles	$L < \lambda/35$ 303 triangles	$L < \lambda/15$ 54 triangles	$L < \lambda/35$ 303 triangles
10^{-2} (-40 dB)	Actual Roots (Resonant Frequencies)	(14 samples) -0.0023+j2.0116 -0.0023+j2.0255 0.0107+j4.0285 -0.0204+j4.0290	(13 samples) -0.0023+j2.0155 -0.0024+j2.0163 0.0021+j4.0186 -0.0119+j4.0187	(14 samples) -0.0023+j2.0116 -0.0023+j2.0255 0.0107+j4.0285 -0.0204+j4.0290	(13 samples) -0.0023+j2.0155 -0.0024+j2.0163 0.0021+j4.0186 -0.0119+j4.0187	(14 samples) -0.0027+j2.0182 -0.0019+j2.0184 -0.0103+j4.0284 0.0009+j4.0286	(15 samples) -0.0001+j2.0157 -0.0046+j2.0159 -0.0052+j4.0179 -0.0045+j4.0200
	Roots occurring in Pole-Zero Pairs						
	Real Roots					0.6172	-8.8868 -0.2696 0.2208 10.2123
	Complex Roots						
10^{-3} (-60 dB)	Actual Roots (Resonant Frequencies)	(31 samples) -0.0023+j2.0178 -0.0023+j2.0188 0.0054+j4.0285	(14 samples) -0.0026+j2.0158 -0.0021+j2.0160 -0.0032+j4.0188 -0.0065+j4.0190	(31 samples) -0.0023+j2.0178 -0.0023+j2.0188 -0.0149+j4.0285 0.0054+j4.0285	(14 samples) -0.0026+j2.0158 -0.0021+j2.0160 -0.0032+j4.0188 -0.0065+j4.0190	(14 samples) -0.0027+j2.0182 -0.0019+j2.0184 -0.0103+j4.0284 0.0009+j4.0286	(16 samples) -0.0064+j2.0153 0.0017+j2.0161 -0.0040+j4.0177 -0.0057+j4.0203
	Roots occurring in Pole-Zero Pairs	-0.2313+j3.0492 0.0011+j4.2903 -0.0021+j4.3462		-0.2313+j3.0492 0.2324+j3.0493 0.0011+j4.2903 -0.0020+j4.3462			
	Real Roots					0.6172	-3.4613 -0.9760 -0.3055 0.2167 5.8454
	Complex Roots			0.0707+j4.3441 -0.0666+j4.3448			
10^{-4} (-80 dB)	Actual Roots (Resonant Frequencies)	(46 samples) -0.0017+j2.0183 -0.0029+j2.0183 -0.0045+j4.0274 -0.0045+j4.0333	(15 samples) -0.0025+j2.0158 -0.0022+j2.0160 -0.0030+j4.0189 -0.0068+j4.0189	(46 samples) -0.0017+j2.0183 -0.0029+j2.0183 	(15 samples) -0.0025+j2.0158 -0.0022+j2.0160 -0.0030+j4.0189 -0.0068+j4.0189	(26 samples) -0.0021+j2.0182 -0.0025+j2.0184 -0.0086+j4.0263 -0.0009+4.0305	(20 samples) -0.0035+j2.0158 -0.0012+j2.0160 -0.0047+j4.0172 -0.0050+j4.0207
	Roots occurring in Pole-Zero Pairs	0.2774+j2.8794 -0.0023+j4.1025 0.0020+j4.1028 0.0175+j4.3096		-0.2817+j2.8789 0.2774+j2.8794		0.0472+j4.3117 -0.0466+j4.3124	-0.3254+j2.5911 0.3441+j2.6028
	Real Roots					0.2204 1.0485 1.4367	-6.5755 -0.2625 0.2062 1.1166 9.0934
	Complex Roots			0.5192+j3.9527 -0.5159+j3.9573 -0.5694+j4.2534 0.5779+j4.2551 -0.4717+j4.5668 0.4753+j4.5792 -0.2016+j4.8025 0.1880+j4.8134		-1.3569+j2.2416 -0.1886+j4.1061 0.1415+j4.1333	

(b) FREQUENCY RANGE [5 GHz, 9 GHz].

Interpolation Error (E_k)	Class of Zeros	Thiele Continued Fraction: Newton-Raphson Method		Thiele Continued Fraction: Polynomial Method		Vector Fitting: SER Eigenvalue Method	
		$L < \lambda/15$ 234 triangles	$L < \lambda/35$ 896 triangles	$L < \lambda/15$ 234 triangles	$L < \lambda/35$ 896 triangles	$L < \lambda/15$ 234 triangles	$L < \lambda/35$ 896 triangles
10^{-2} (-40 dB)		(14 samples)	(13 samples)	(14 samples)	(13 samples)	(14 samples)	(14 samples)
	Actual Roots (Resonant Frequencies)	-0.0071+j6.0301 -0.0079+j6.0331 -0.0107+j8.0351 -0.0092+j8.0390	-0.0078+j6.0189 -0.0077+j6.0322 -0.0105+j8.0185 -0.0100+j8.0236	-0.0071+j6.0301 -0.0079+j6.0331 -0.0107+j8.0351 -0.0092+j8.0390	-0.0078+j6.0189 -0.0077+j6.0322 -0.0105+j8.0185 -0.0100+j8.0236	-0.0076+j6.0245 -0.0074+j6.0385 -0.0100+j8.0297 -0.0100+j8.0444	-0.0077+j6.0189 -0.0078+j6.0322 -0.0102+j8.0201 -0.0103+j8.0222
	Roots occurring in Pole-Zero Pairs						
	Real Roots					0.1507	0.9794
	Complex Roots						
10^{-3} (-60 dB)		(14 samples)	(14 samples)	(14 samples)	(14 samples)	(19 samples)	(15 samples)
	Actual Roots (Resonant Frequencies)	-0.0071+j6.0301 -0.0079+j6.0331 -0.0107+j8.0351 -0.0092+j8.0390	-0.0077+j6.0191 -0.0078+j6.0321 -0.0104+j8.0188 -0.0102+j8.0234	-0.0071+j6.0301 -0.0079+j6.0331 -0.0107+j8.0351 -0.0092+j8.0390	-0.0077+j6.0191 -0.0078+j6.0321 -0.0104+j8.0188 -0.0102+j8.0234	-0.0075+j6.0292 -0.0075+j6.0339 -0.0099+j8.0342 -0.0101+j8.0399	-0.0077+j6.0189 -0.0078+j6.0323 -0.0105+j8.0203 -0.0100+j8.0219
	Roots occurring in Pole-Zero Pairs					-0.0303+j7.8519	
	Real Roots						
	Complex Roots					-1.4340+j6.7123 1.3013+j6.9350	
10^{-4} (-80 dB)		(23 samples)	(18 samples)	(23 samples)	(18 samples)	(27 samples)	(19 samples)
	Actual Roots (Resonant Frequencies)	-0.0074+j6.0294 -0.0076+j6.0337 -0.0099+j8.0342 -0.0101+j8.0400	-0.0077+j6.0191 -0.0078+j6.0320 -0.0101+j8.0204 -0.0105+j8.0218	-0.0026+j6.0296 -0.0124+j6.0336 0.0028+j8.0274 -0.0236+j8.0469	-0.0077+j6.0191 -0.0078+j6.0320 -0.0100+j8.0204 -0.0105+j8.0218	-0.0056+j6.0306 -0.0094+j6.0325 -0.0099+j8.0342 -0.0101+j8.0399	-0.0077+j6.0188 -0.0078+j6.0323 -0.0105+j8.0204 -0.0100+j8.0218
	Roots occurring in Pole-Zero Pairs	0.0479+j5.5481 -0.0771+j8.2493		0.0479+j5.5481 -0.0763+j8.2492		0.3050+j5.0479 -0.3856+j5.3637 0.0178+j5.9873 -0.0271+j7.7551 0.0060+j7.8947	0.3225+j8.1055 -0.1025+j8.2091
	Real Roots						
	Complex Roots			-0.9752+j7.4368 0.9165+j7.5810		-2.1872+j6.1164 1.9425+j6.4670	

overdetermined equations need to be solved and data may be contaminated with noise. A modified VF, called Vector Fitting with Adding and Skimming (VF-AS) [71], has also shown to be capable of handling noisy data successfully and improving the convergence properties of VF. Though this is not required in the case of very accurate EM analysis, it does broaden the applicability of the technique significantly.

To attain the desired accuracy, the fitting function will be of a higher order than the number of roots defining Eq. 4.5 over the interval of interest. To distinguish the actual roots (resonance frequencies) from others, four steps of elimination are used:

i) As the interpolant is valid within a specified frequency range only, all roots outside of this interval are assumed to be invalid and void.

ii) Roots occurring in pole-zero pairs are identified by calculating the poles of the denominator and matching poles to zeros that are within 0.003 absolute distance of each other.

iii) Complex roots are identified as those roots where the $|\sigma/\omega|$ ratio is larger than 1%. Note that the real parts of the zero values are not used to calculate loss, as the required accuracy

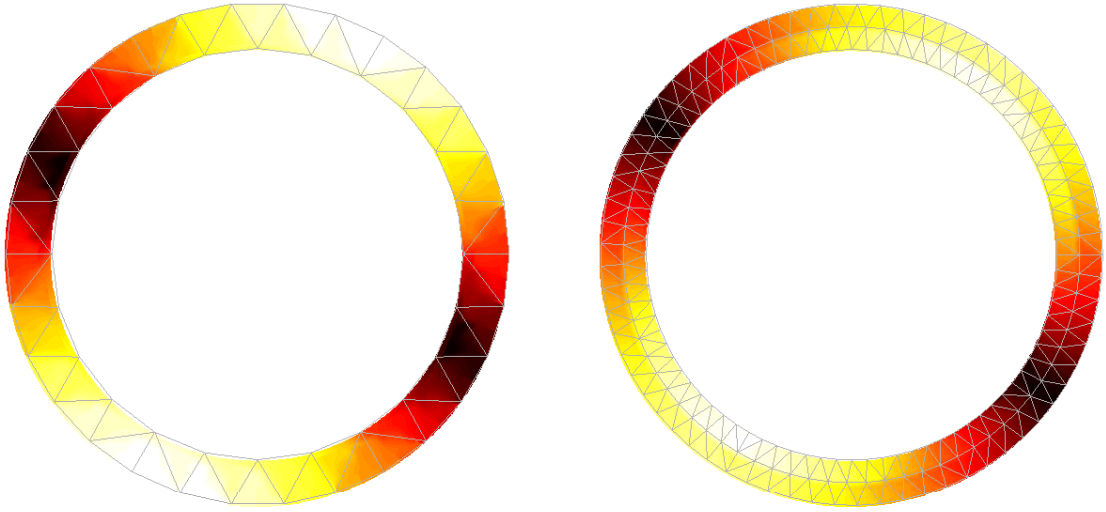

(a) $\lambda/15$ mesh (54 triangles). (b) $\lambda/35$ mesh (303 triangles).

Fig. 4.4. Current distribution for TM_{110} mode as calculated on different meshings.

for this is extremely high. Rather, only the imaginary part is used to give the resonance frequencies.

iv) Real roots are single-valued and have insignificant imaginary parts.

Thiele Continued Fraction—Newton-Raphson Method

In this method, root-finding is based on the direct evaluation of the Thiele representation. Ideally, the roots of $\det[Z(s)]$ should all lie on the $j\omega$-axis. However, as numerical approximations can cause some of the zeros to shift slightly into the complex plane, the algorithm needs to be configured to search in a narrow band around the $j\omega$-axis. In addition, zeros belonging to pole-zero pairs need to be identified.

As an iterative search method with a finite termination criterion, it is possible for the algorithm to miss one or more roots, especially when closely spaced. This happens regardless of a high-precision accuracy in the model as can be seen in Table 4.1(a) for the $\lambda/15$ coarse mesh and -60 dB interpolation error. This is quite important, as the existence of dual and triple mode resonances are unavoidable in microwave structures and the roots should be identified correctly.

A higher-order overdetermined model naturally results in the calculation of more roots. The effect of oversampling can be seen for the $\lambda/15$ mesh and a -80 dB error (Table 4.1(a)). Three roots (identified as pole-zero combinations) were found in close proximity of the 4.02 GHz natural frequency. As the model order increases, it becomes more difficult to correctly distinguish the resonance frequencies from invalid zeros.

Thiele Continued Fraction—Polynomial Method

In this method, the need for an iterative root-finding algorithm is eliminated. The number of computed roots is now equal to the order of the numerator and the roots may be located

anywhere within the complex frequency plane.

The conversion from a continued fraction representation to a ratio of polynomials can incur a loss of accuracy, especially in models of high order. Note that for the -40 dB and -60 dB interpolation errors, both root-finding algorithms used with the Thiele-type interpolation model predict the same resonances. However, for the -80 dB case, a large number of complex roots in the vicinity of the TM_{210} resonance frequencies were predicted without finding the actual mode frequencies. This failure is a direct consequence of the loss in quality of the polynomial model. This can be rectified by sub-dividing the interval to ensure computation of lower order high accuracy models.

Vector Fitting—SER Eigenvalue Method

As before, the roots can be either imaginary roots (the actual resonances), real roots or roots occurring in complex conjugate pairs. In the final comparison the VF SER proves to be the most robust technique, identifying all sought resonance frequencies correctly. As the VF technique estimates residues of partial fractions, which requires less significant digits than the coefficients of a polynomial, the pole-residue model often provides a more accurate representation for broadband solutions (with fewer samples). Comparing the -80 dB results (Table 4.1(a)), the VF least-squares approach required only 26 support points for a smooth fit while the continued fractions model was oversampled with 46 support points. In the second higher frequency interval (Table 4.1(b)) the effect of oversampling is not as dramatic and models of similar order are required by the Thiele and VF approaches.

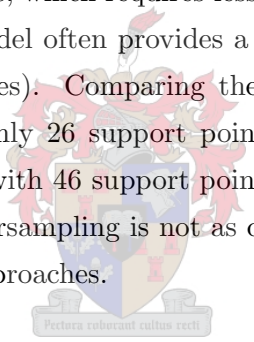

Conclusion

The fitting error of the Vector Fitting technique is highly accurate and quite comparable to interpolation techniques based on continued fractions. However, when searching for the roots of the interpolant, the SER eigenvalue method as applied to the VF model was found to be a non-iterative and robust technique, which accurately and successfully predicts the location of all possible resonance frequencies in the interpolation interval. Furthermore, the VF pole-residue model compensates for numerical noise in the data by solving a system of overdetermined equations.

4.1.4 Study 2—Investigation of the Effects of Loss

The second investigation aims to establish the effect of losses on resonance frequencies. This investigation follows from the observation that several models, namely, the straight-line approximation [55], the different magnetic-wall models [56, 59] and the eigenmode solver of the commercial code CST Microwave Studio Version 5 (CST), offer only limited capabilities for the inclusion of losses in the model. Based on the MoM eigenmode analysis and either the Thiele continued fraction or the VF rational modelling techniques, this study investigates the accuracy

of the resonant frequencies (both fundamental and higher-order mode frequencies) of a planar ring resonator by comparison to the mentioned models and by introducing different components of loss in the model.

Two test structures were selected, each consisting of an unloaded planar ring resonator with mean ring radius $R = 16.9$ mm. The first ring (Ring #1) was chosen to support TM_{n10} modes only, with a normalised ring width $w/R = 0.1$. Computer simulations were performed in the frequency range [1 GHz, 9 GHz]. To support higher-order modes, however, the normalised ring width has to be greater than 0.2. A second low impedance ring (Ring #2) was therefore selected with a normalised ring width $w/R = 0.6$. Since higher-order modes are usually more closely spaced in frequency, simulations were only performed in the frequency range [1.5 GHz, 6.5 GHz]. The substrate parameters used in the simulations are that of Taconic TLY-5, which

TABLE 4.2
Comparison of the resonant frequencies calculated by solution of the natural frequencies of an unloaded resonator (Ring #1) with different loss components. All roots are presented in GHz. (Frequency range [1 GHz, 9 GHz]; L = Maximum Discretisation Size; E_k = Maximum Interpolation Error; Substrate parameters for Taconic TLY-5: $h = 0.508$ mm, $\epsilon_r = 2.2$, $\tan(\delta) = 0.0009$; Ring parameters: $R = 16.9$ mm, $w/R = 0.1$)

(a) Lossless covered microstrip ring resonator.

Resonant Mode	Straight-Line Model	Magnetic-Wall Model	Improved Magnetic-Wall Model	CST ($L < \lambda/35$)		Thiele Continued Fractions ($L < \lambda/35$, $E_k < -80$ dB)		Vector Fitting ($L < \lambda/35$, $E_k < -80$ dB)	
TM_{110}	2.0175	1.9926	1.9926	2.0190	2.0190	2.0154	2.0155	2.0130	2.0179
TM_{210}	4.0350	4.0272	4.0061	4.0195	4.0295	4.0286	4.0288	4.0264	4.0310
TM_{310}	6.0524	6.0404	6.0192	6.0172	6.0173	6.0305	6.0436	6.0305	6.0436
TM_{410}	8.0699	8.0530	8.0318	7.9566	8.0084	8.0328	8.0344	8.0328	8.0344

(b) Lossy covered microstrip ring resonator (dielectric losses).

Resonant Mode	Straight-Line Model	Magnetic-Wall Model	Improved Magnetic-Wall Model	CST ($L < \lambda/35$)		Thiele Continued Fractions ($L < \lambda/35$, $E_k < -80$ dB)		Vector Fitting ($L < \lambda/35$, $E_k < -80$ dB)	
TM_{110}				2.0195	2.0195	2.0151	2.0158	2.0142	2.0167
TM_{210}				4.0208	4.0304	4.0275	4.0299	4.0270	4.0304
TM_{310}				6.0187	6.0188	6.0302	6.0438	6.0304	6.0436
TM_{410}				7.9581	8.0107	8.0325	8.0348	8.0330	8.0342

(c) Lossy covered microstrip ring resonator (dielectric and conductor losses).

Resonant Mode	Straight-Line Model	Magnetic-Wall Model	Improved Magnetic-Wall Model	CST		Thiele Continued Fractions ($L < \lambda/35$, $E_k < -80$ dB)		Vector Fitting ($L < \lambda/35$, $E_k < -80$ dB)	
TM_{110}						2.0142	2.0147	2.0133	2.0157
TM_{210}						4.0260	4.0285	4.0270	4.0276
TM_{310}						6.0286	6.0419	6.0287	6.0418
TM_{410}						8.0304	8.0328	8.0315	8.0316

(d) Lossy microstrip ring resonator (dielectric, conductor and radiation losses).

Resonant Mode	Straight-Line Model	Magnetic-Wall Model	Improved Magnetic-Wall Model	CST		Thiele Continued Fractions ($L < \lambda/35$, $E_k < -80$ dB)		Vector Fitting ($L < \lambda/35$, $E_k < -80$ dB)	
TM_{110}						2.0158	2.0160	2.0158	2.0160
TM_{210}						4.0189	4.0189	4.0172	4.0207
TM_{310}						6.0191	6.0320	6.0188	6.0323
TM_{410}						8.0204	8.0218	8.0204	8.0218

has a relative permittivity of $\epsilon_r = 2.2$, a dissipation factor of $\tan(\delta) = 0.0009$ and a thickness of $h = 0.508$ mm.

Table 4.2 shows the results of this experiment for Ring #1, while Table 4.3 lists the results for Ring #2. For the calculation of the natural frequencies of these resonators, the maximum discretisation size L was set to $\lambda/35$ at the maximum frequency in each interval; and the interpolation error E_k (Eq. 4.24) was required to be less than -80 dB across the band. The characteristics that emerged from this study are presented below.

Accuracy and Higher-Order Modes

i) For Ring #1, the first four natural pairs of resonant frequencies were found in the region of 2.02 GHz, 4.02 GHz, 6.03 GHz and 8.02 GHz. Fig. 4.5 shows the instantaneous surface

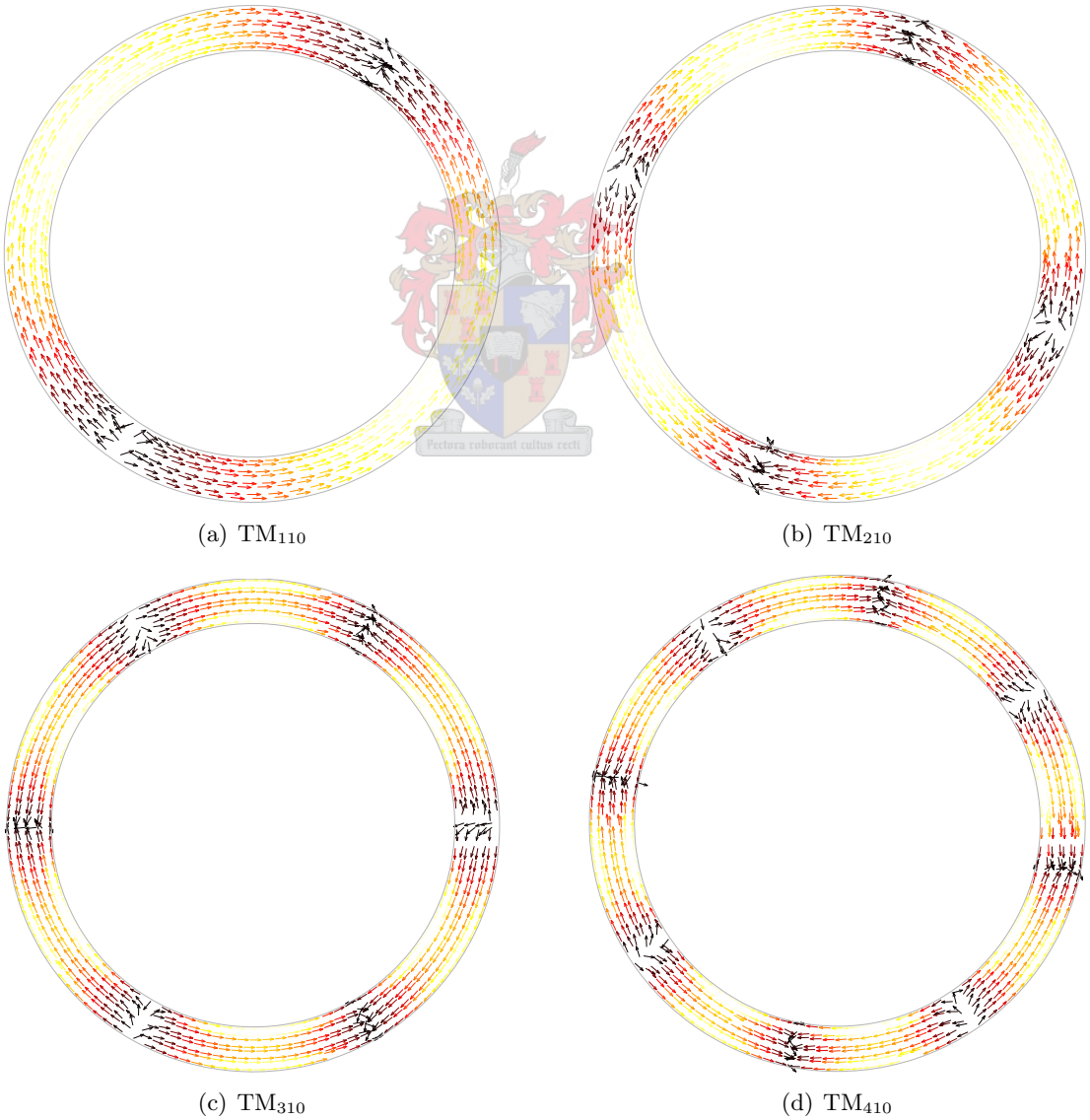

(a) TM_{110} (b) TM_{210}

(c) TM_{310} (d) TM_{410}

Fig. 4.5. Instantaneous surface currents of a microstrip ring resonator (Ring #1) at the first four natural mode frequencies. (Substrate parameters for Taconic TLY-5: $h = 0.508$ mm, $\epsilon_r = 2.2$, $\tan(\delta) = 0.0009$; Ring parameters: $R = 16.9$ mm, $w/R = 0.1$)

TABLE 4.3
COMPARISON OF THE RESONANT FREQUENCIES CALCULATED BY SOLUTION OF THE NATURAL FREQUENCIES OF AN UNLOADED RESONATOR (RING #2) WITH DIFFERENT LOSS COMPONENTS. ALL ROOTS ARE PRESENTED IN GHZ. (FREQUENCY RANGE [1.5 GHZ, 6.5 GHZ]; L = MAXIMUM DISCRETISATION SIZE; E_k = MAXIMUM INTERPOLATION ERROR; SUBSTRATE PARAMETERS FOR TACONIC TLY-5: $h = 0.508$ mm, $\epsilon_r = 2.2$, $\tan(\delta) = 0.0009$; RING PARAMETERS: $R = 16.9$ mm, $w/R = 0.6$)

(a) LOSSLESS COVERED MICROSTRIP RING RESONATOR.

Resonant Mode	Magnetic-Wall Model	Improved Magnetic-Wall Model	CST ($L < \lambda/35$)		Thiele Continued Fractions ($L < \lambda/35$, $E_k < -80$ dB)		Vector Fitting ($L < \lambda/35$, $E_k < -80$ dB)	
TM_{110}	1.9734	1.9327	2.0068	2.0075	2.0389	2.0396	2.0386	2.0399
TM_{210}	3.6272	3.5255	3.5865	3.5936	3.6577	3.6579	3.6573	3.6583
TM_{310}	5.0613	4.9189	4.9647	4.9686	5.0346	5.0707	5.0348	5.0711
TM_{020}	5.3654	5.1508	5.0022	5.1400		5.3178		5.3205
TM_{120}	6.0404	5.8576	5.8459	5.8466	5.9860	5.9869	5.9840	5.9889
TM_{410}	6.4159	6.2521	6.2789	6.2958	6.3948	6.3954	6.3948	6.3954

(b) LOSSY COVERED MICROSTRIP RING RESONATOR (DIELECTRIC LOSSES).

Resonant Mode	Magnetic-Wall Model	Improved Magnetic-Wall Model	CST ($L < \lambda/20$)		Thiele Continued Fractions ($L < \lambda/35$, $E_k < -80$ dB)		Vector Fitting ($L < \lambda/35$, $E_k < -80$ dB)	
TM_{110}			1.9985	1.9998	2.0389	2.0396	2.0388	2.0397
TM_{210}			3.5650	3.5674	3.6571	3.6585	3.6566	3.6591
TM_{310}			4.9238	4.9295	5.0347	5.0708	5.0348	5.0707
TM_{020}			4.9671	5.1382		5.4686	5.3196	5.4689
TM_{120}			5.8113	5.8116	5.9851	5.9878	5.9843	5.9885
TM_{410}			6.2147	6.2456	6.3930	6.3971	6.3938	6.3960

(c) LOSSY COVERED MICROSTRIP RING RESONATOR (DIELECTRIC AND CONDUCTOR LOSSES).

Resonant Mode	Magnetic-Wall Model	Improved Magnetic-Wall Model	CST		Thiele Continued Fractions ($L < \lambda/35$, $E_k < -80$ dB)		Vector Fitting ($L < \lambda/35$, $E_k < -80$ dB)	
TM_{110}					2.0382	2.0384	2.0381	2.0385
TM_{210}					3.6557	3.6575	3.6564	3.6568
TM_{310}					5.0335	5.0692	5.0334	5.0694
TM_{020}						5.3175		5.3180
TM_{120}					5.9842	5.9857	5.9841	5.9861
TM_{410}					6.3927	6.3942	6.3934	6.3936

(d) LOSSY MICROSTRIP RING RESONATOR (DIELECTRIC, CONDUCTOR AND RADIATION LOSSES).

Resonant Mode	Magnetic-Wall Model	Improved Magnetic-Wall Model	CST		Thiele Continued Fractions ($L < \lambda/35$, $E_k < -80$ dB)		Vector Fitting ($L < \lambda/35$, $E_k < -80$ dB)	
TM_{110}					2.0373	2.0374	2.0368	2.0378
TM_{210}					3.6222	3.6231	3.6224	3.6229
TM_{310}					4.9969	5.0317	4.9967	5.0320
TM_{020}						5.1868	5.1771	5.1868
TM_{120}					5.9567	5.9571	5.9567	5.9571
TM_{410}					6.3595	6.3600	6.3595	6.3600

currents at these resonances, which correspond to the TM_{110}, TM_{210}, TM_{310} and TM_{410} modes.

ii) For Ring #2, the first six natural pairs of resonant frequencies were found in the region of 2.04 GHz, 3.62 GHz, 5.01 GHz, 5.18 GHz, 5.96 GHz and 6.36 GHz. Fig. 4.6 shows the instantaneous surface currents at these resonances, which correspond to the TM_{110}, TM_{210}, TM_{310}, TM_{020}, TM_{120} and TM_{410} modes. Note the presence of the higher-order modes TM_{020} and TM_{120}, which are characteristic for normalised ring widths of small impedance ($w/R > 0.2$).

iii) The CST eigenmode solver requires the ring model to be enclosed by a finite PEC bounding box. For the purposes of comparison, where either microstrip or covered microstrip was used, the CST cavity-modes were ignored.

iv) Ring #1 yielded accuracies of within 0.5% of the straight-line model, within 1.3% of the magnetic-wall models and within 1% of the CST data.

v) The accuracies of the respective f_0 predictions for Ring #2 varied by a slightly larger margin than for Ring #1, but still yielded good agreement. Predictions were accurate to within 5% of the magnetic-wall models and 3% of the CST data when omitting the TM_{020} results. Since the frequencies of modes TM_{310} and TM_{020} are less than 5% apart, the task of identifying all frequencies correctly becomes a lot more difficult. Note for example that the CST eigenmode solver predicted the dual resonance frequencies of the TM_{020} mode to differ by 2.8% and 3.4% in Table 4.3(a) and (b) respectively. A separation of dual mode frequencies that is of a similar order of magnitude than the separation in frequency for different resonance modes can therefore lead to the incorrect identification of a specific mode frequency. The Thiele and Vector Fitting approaches show a similar behaviour in separating the dual frequencies of the TM_{020} mode. Also, these mode frequencies were found slightly deeper into the complex plane, thereby not adhering to the identification criterion of $|\sigma/\omega| < 1\%$.

vi) Even though the straight-line model yielded a good first approximation for Ring #1 where the ring width/ring radius (w/R) is small, the model falls well short of correctly predicting the resonance frequencies for Ring #2, where a line of low impedance was used. As such, the mean radius is not well-defined and the influence of curvature becomes important. Also, the model can only be used to estimate the TM_{n10} mode frequencies when no higher-order modes are present. Thus, except for the prediction of the fundamental TM_{110} mode frequency at 2.02 GHz, this model cannot be used to predict the resonance frequencies of low impedance rings such as Ring #2.

Loss Components

One of the biggest advantages of using an in-house code is the possibility to access and develop the code to satisfy specific model requirements. The effect of different loss factors on the prediction of the resonant frequencies was investigated by gradually introducing dielectric, conductor and radiation losses respectively.

The results of this investigation are shown in Tables 4.2 and 4.3 where the model in (a) is assumed lossless** and the model in (d) includes all the components of loss. The covered microstrip ring resonator was modelled with a PEC parallel plate structure in the MoM analysis, while the CST eigenmode solver assumed PEC boundary conditions all-around. Dielectric losses were included by adjusting the dissipation factor $\tan(\delta)$ and conductor losses were introduced by assuming a

**Losses due to travelling surface waves were neglected.

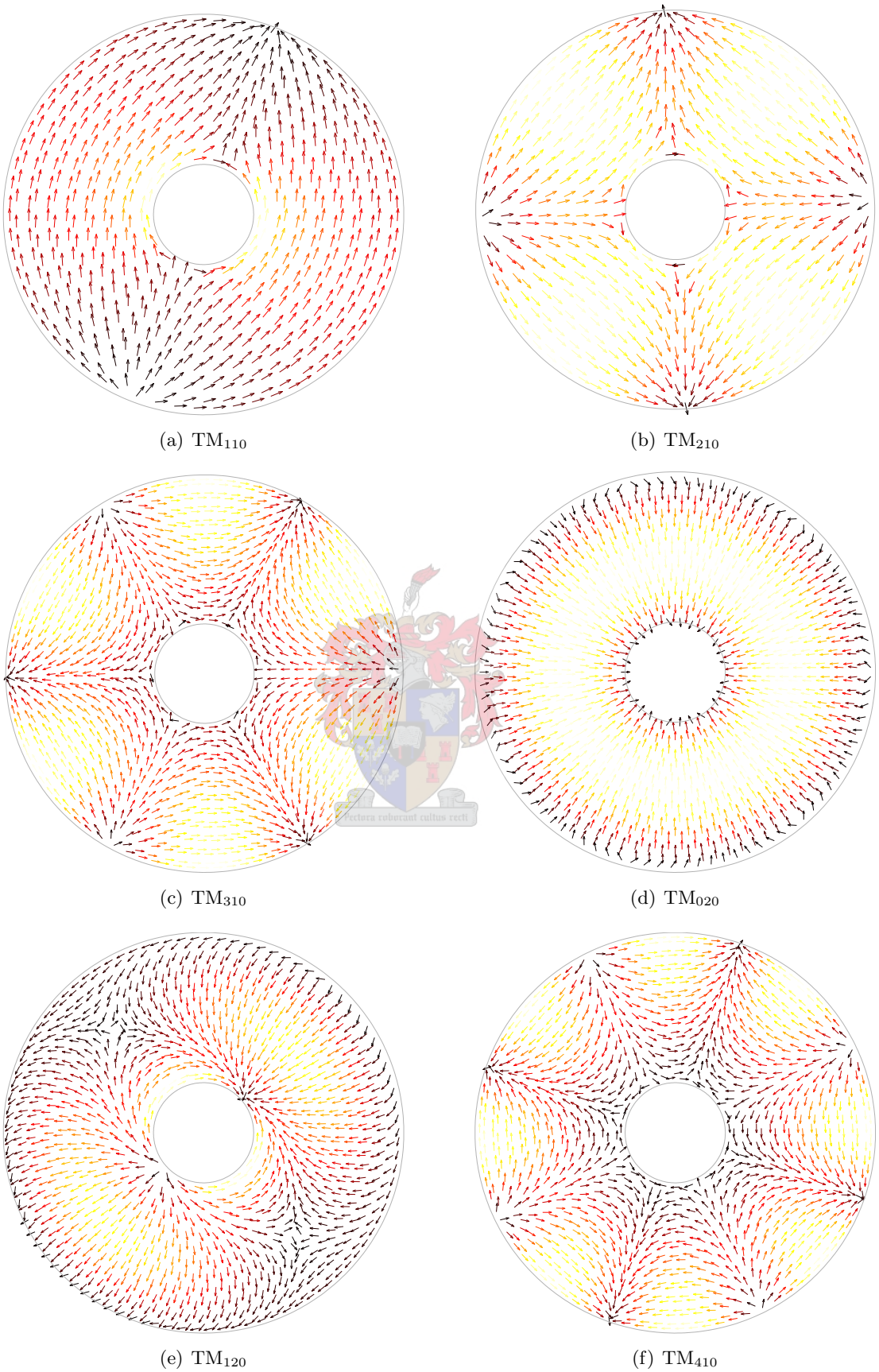

(a) TM_{110} (b) TM_{210}

(c) TM_{310} (d) TM_{020}

(e) TM_{120} (f) TM_{410}

Fig. 4.6. Instantaneous surface currents of a microstrip ring resonator (Ring #2) at the first six natural mode frequencies. (Substrate parameters for Taconic TLY-5: $h = 0.508$ mm, $\epsilon_r = 2.2$, $\tan(\delta) = 0.0009$; Ring parameters: $R = 16.9$ mm, $w/R = 0.6$)

finite surface impedance Z_s, present on the ring surface.

From the analyses it was found that most of the methods do not support the inclusion of different components of loss in their models. The straight-line approximation and the magnetic-wall models assume an ideal problem neglecting all forms of loss, while the CST model shows an incapability to model both conductor losses and radiation losses present in an open structure. However, the question arises as to how important the inclusion of these components of loss is on the accurate prediction of the resonance frequencies. The following observations were made:

i) The resonant frequencies show a decrease in value as more loss components are introduced.

ii) The inclusion of $\tan(\delta) = 0.0009$ had little effect ($< 0.06\%$) on the value of f_0. Materials with larger dissipation factors may, however, show larger deviation upon introducing dielectric losses in the model.

iii) The inclusion of conductor losses introduced insignificant changes in f_0 of less than 0.07%.

iv) The inclusion of radiation losses introduced changes in f_0 of less than 0.24%.

Conclusion

The inclusion of loss in the various models does not have a significant influence on the prediction of the resonant frequencies. However, these factors cannot be ignored when predicting characteristics such as the Q-values, which of course give a direct indication of the losses in the structure. Without introducing any additional computational effort, the more accurate model may just as well also be used in the extraction of the resonant frequencies.

4.2 Calculation of Resonant Frequencies through Scattering Parameters of a Loaded Resonator

An alternative way of calculating resonant frequencies is to use the S-parameters of a loaded resonator. Chang *et al.* [72] used a T-network in terms of equivalent impedances with a closed form solution to analyse the ring circuit, showing accuracies of better than 0.2% with respect to measurements of the fundamental TM_{110} mode. A distributed circuit model using cascaded transmission line segments to easily incorporate any discontinuities along the ring and predict mode splitting in asymmetric ring structures has also been used [73], but the accuracy of results were not discussed. When using CEM analyses, S-parameter data with a high spectral density is normally needed for the extraction of f_0 and Q, as resonant structures have the distinct property of sharp peaks and valleys, as shown in Fig. 4.8(a), which are difficult to model and predict accurately.

This section presents two experimental studies. In the first study, the two rational modelling approaches investigated in the modelling of an unloaded resonator (Thiele continued fractions

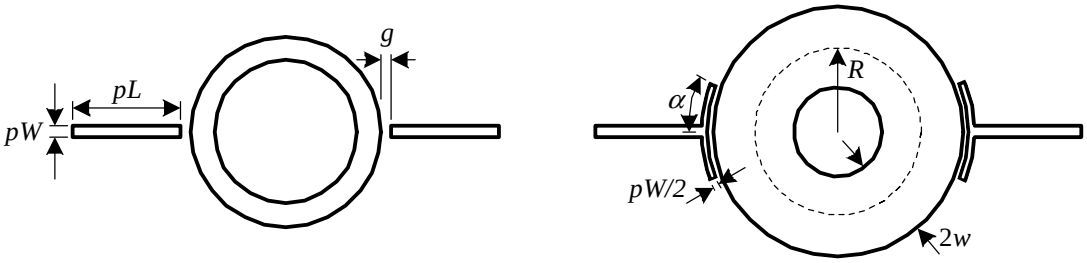

Fig. 4.7. Excitation used to construct ring resonators of normalised ring width $w/R = 0.1$ and $w/R = 0.6$.

and Vector Fitting) are compared with respect to their ability to predict the resonance frequencies of a loaded microwave ring resonator. The prediction of both fundamental and higher-order resonances are investigated and results are verified against predictions obtained from commercial software and measurement. In addition, a new algorithm for the extraction of the resonant frequencies from the rational approximation of the scattering parameter magnitude plot is proposed. The second study investigates the correctness of the interpolation function, by focusing on asymmetries in the discretisation causing unwanted mode splitting.

4.2.1 Study 1—Investigation of the Accuracy of Different Model Predictions

When a loaded microstrip ring resonator is loosely coupled to its feed lines, the coupling gap capacitances do not greatly affect the intrinsic resonant frequencies of the ring. Using this model of loose coupling, the ring resonators of Section 4.1.4 were loaded with symmetrically arranged feed lines as shown in Fig. 4.7. Ring #1 was excited with feed lines of length $pL = 3$ mm and width $pW = 1.53$ mm, and a coupling gap size of $g = 0.7h$. However, when using the same excitation on the lower impedance ring (Ring #2), coupling was found to be too small. To increase the coupling, the following feed parameters were used: $pL = 5$ mm, $pW = 1.53$ mm, $\alpha = 15°$ and $g = 0.6h$. This investigation focuses on the comparison of different rational metamodels with respect to their ability to approximate the S-parameter response of a resonator accurately before locating the resonance frequencies at the maxima of the S-parameter magnitude response.

Fig. 4.8(a) shows the S-parameter response of Ring #1 as calculated with the MoM code. Using the Vector Fitting adaptive rational interpolation formulation, a response with a -100 dB accuracy in the interpolant ($E_k(f) = |\Re_k(f) - \Re_{k-1}(f)|$) and only 20 support points was found. Fig. 4.8(b) shows the comparative result when using the same number of support points, but at equally spaced discrete frequency points. Since no additional data exist between the selected points, this method fails to correctly predict the system response. Even if the number of discrete evaluation points is increased to a large number, which is computationally inefficient, there is a chance that the points of resonance will still be missed.

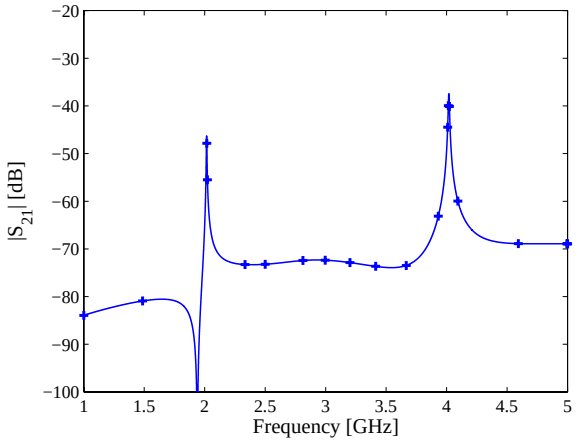

(a) MoM using adaptive rational interpolation. (20 support points; $E_k(f) = 10^{-5}$)

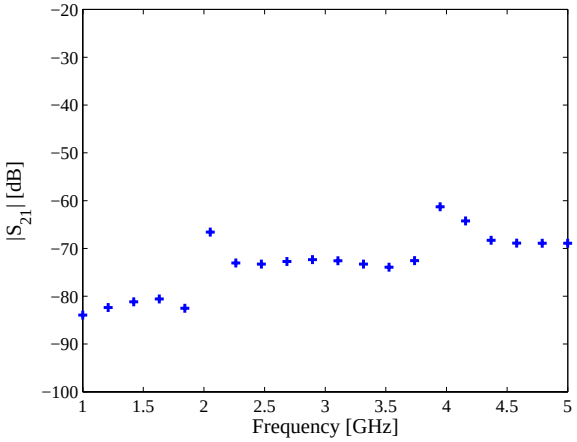

(b) MoM using 20 discrete equally spaced support points.

Fig. 4.8. Comparison of S_{21} magnitude responses obtained using an equal number of samples for the adaptive rational interpolation formulation and the evaluation of linearly spaced discrete frequencies.

To obtain the resonant frequencies numerically from the interpolant of the S-parameters, use is made of the fact that the interpolant can be evaluated at any frequency point with little extra cost. An initial estimate of f_0 is taken from the S-parameter plot. The interpolant is then evaluated at a large number of equally spaced points (e.g. 100 Hz apart) around f_0. The frequency associated with the maximum magnitude then becomes the new resonant frequency. If this frequency falls on the first or last point in the evaluated interval, the S-parameter slope is either decreasing or increasing and the process is repeated. Otherwise, the interval includes the correct resonance value and the spacing is decreased to 10% of the previous interval spacing, i.e. 10 Hz. The process then repeats itself and the algorithm terminates when the frequency spacing reaches the user defined accuracy of e.g. 0.1 Hz.

Table 4.4 shows the results of this experiment for Ring #1, while Table 4.5 lists the results for Ring #2. The maximum discretisation size L was set to $\lambda/35$ at the maximum frequency in each interval; and the interpolation error E_k was required to be less than -100 dB across the band. Comments on accuracy and higher-order modes are given below.

Accuracy and Higher-Order Modes

i) As the rings are excited using colinear feed lines, only one of the dual mode frequencies will be excited.

ii) Using the described algorithm for the extraction of the resonant frequencies from a rational approximation of the scattering parameter magnitude plot, the first four resonant frequencies of Ring #1 were calculated as 2.02 GHz, 4.02 GHz, 6.02 GHz and 8.02 GHz, all corresponding to the TM_{n10} modes.

iii) Similarly for Ring #2, five resonant frequencies were identified at 2.04 GHz, 3.62 GHz, 5.00 GHz, 5.97 GHz and 6.36 GHz, corresponding to the TM_{110}, TM_{210}, TM_{310}, TM_{120} and TM_{410} modes. Note that the higher-order TM_{020} resonance frequency could not be

TABLE 4.4
Comparison of the resonant frequencies calculated through scattering parameters of a loaded resonator (Ring #1) with different loss components.
All roots are presented in GHz. (Frequency range [1 GHz, 9 GHz];
L = Maximum Discretisation Size; E_k = Maximum Interpolation Error;
Substrate parameters for Taconic TLY-5: $h = 0.508$ mm, $\epsilon_r = 2.2$, $\tan(\delta) = 0.0009$;
Ring parameters: $R = 16.9$ mm, $w/R = 0.1$, $g = 0.7h$, $pL = 3$ mm, $pW = 1.53$ mm)

(a) Lossy covered microstrip ring resonator (dielectric and conductor losses).

Resonant Mode	Measurements	FEKO ($L < \lambda/35$)	Thiele Continued Fractions ($L < \lambda/35$, $E_k < -100$ dB)	Vector Fitting ($L < \lambda/35$, $E_k < -100$ dB)
TM_{110}	2.0195	2.0214	2.0221	2.0220
TM_{210}	4.0328	4.0331	4.0339	4.0339
TM_{310}	6.0173	6.0352	6.0357	6.0357
TM_{410}	8.0027	8.0246	8.0369	8.0369

(b) Lossy microstrip ring resonator (dielectric, conductor and radiation losses).

Resonant Mode	Measurements	FEKO ($L < \lambda/35$)	Thiele Continued Fractions ($L < \lambda/35$, $E_k < -100$ dB)	Vector Fitting ($L < \lambda/35$, $E_k < -100$ dB)
TM_{110}	2.0046	2.0102	2.0158	2.0158
TM_{210}	4.0102	4.0150	4.0186	4.0186
TM_{310}	6.0040	6.0132	6.0180	6.0180
TM_{410}	7.9918	8.0032	8.0196	8.0196

TABLE 4.5
Comparison of the resonant frequencies calculated through scattering parameters of a loaded resonator (Ring #2) with different loss components.
All roots are presented in GHz. (Frequency range [1.5 GHz, 6.5 GHz];
L = Maximum Discretisation Size; E_k = Maximum Interpolation Error;
Substrate parameters for Taconic TLY-5: $h = 0.508$ mm, $\epsilon_r = 2.2$, $\tan(\delta) = 0.0009$;
Ring parameters: $R = 16.9$ mm, $w/R = 0.6$, $g = 0.6h$, $pL = 5$ mm, $pW = 1.53$ mm, $\alpha = 15°$)

(a) Lossy covered microstrip ring resonator (dielectric and conductor losses).

Resonant Mode	Measurements	FEKO ($L < \lambda/35$)	Thiele Continued Fractions ($L < \lambda/35$, $E_k < -100$ dB)	Vector Fitting ($L < \lambda/35$, $E_k < -100$ dB)
TM_{110}	2.0101	2.0120	2.0412	2.0411
TM_{210}	3.6189	3.6350	3.6431	3.6432
TM_{310}	5.0785	5.0367	5.0365	5.0366
TM_{020}				
TM_{120}	5.8893	5.9535	6.0075	6.0074
TM_{410}	6.3217	6.3749	6.3919	6.3919

(b) Lossy microstrip ring resonator (dielectric, conductor and radiation losses).

Resonant Mode	Measurements	FEKO ($L < \lambda/35$)	Thiele Continued Fractions ($L < \lambda/35$, $E_k < -100$ dB)	Vector Fitting ($L < \lambda/35$, $E_k < -100$ dB)
TM_{110}	1.9661	1.9778	2.0397	2.0394
TM_{210}	3.5484	3.5813	3.6222	3.6222
TM_{310}	4.9434	4.9811	4.9963	4.9963
TM_{020}				
TM_{120}	5.8450	5.8982	5.9661	5.9661
TM_{410}	6.2863	6.3286	6.3590	6.3590

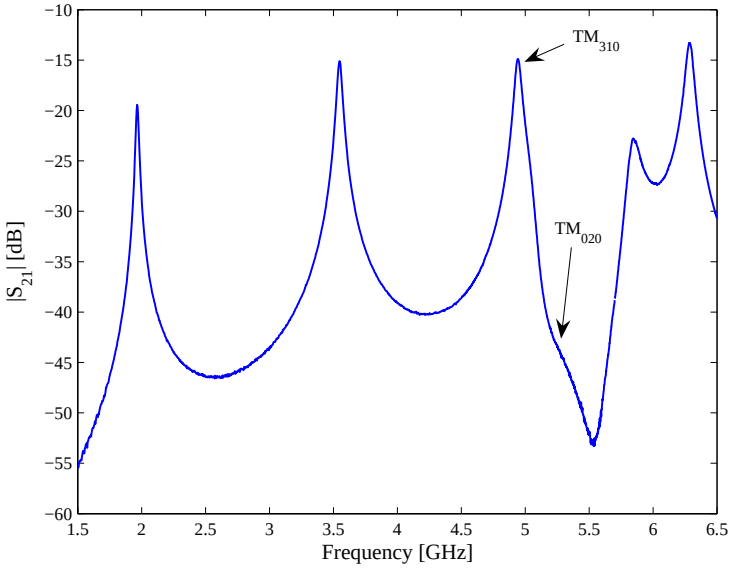

Fig. 4.9. S_{21} magnitude response of Ring #2 demonstrating the improbability of correctly identifying the TM_{020} mode frequency.

extracted from the S-parameter response as the TM_{310} and the TM_{020} modes were too closely spaced in frequency. This is shown in Fig. 4.9 where the TM_{020} mode disappears below the skirts of the more strongly coupled TM_{310} mode.

iv) Compared to the resonant frequencies read off the S_{21} magnitude responses measured and computed with FEKO Suite 4.2, the frequencies for Ring #1 were found to agree within 0.6% and 0.3% respectively. Also, compared to the natural frequencies found in Section 4.1.4 Table 4.2, results were within 0.3% of the MoM and 1.0% of the CST predictions.

v) For Ring #2, the comparisons yielded accuracies of better than 3.6% and 3.0% compared to the measured and FEKO simulated results. Larger discrepancies in the measured results may be as a result of the finite size ground planes used in the practical structure. Compared to the natural frequencies found in Section 4.1.4 Table 4.3, results were within 0.7% of the MoM and 3.3% of the CST predictions.

Conclusion

Mode identification from an S-parameter response requires the finding of resonance peaks or maxima. Similar to the extraction techniques based on the solution of an eigenmode problem, resonance frequencies can be predicted accurately. However, finding multiple maxima using an automated algorithm poses a far more daunting task than to identify multiple zeros, as numerical noise effects can easily be misinterpreted as resonance frequencies. In addition, the technique can only identify the resonance frequencies of modes that are excited and do not disappear below the skirts of nearby modes that are more strongly coupled.

4.2.2 Study 2—Investigation of Mode Splitting

A microstrip ring resonator is known to support two degenerate (orthogonal) modes that coexist independently of each other. If circular symmetrical ring resonators are used with colinear feed lines, then only one of these modes will be excited. If the coupling lines are arranged asymmetrically (or the symmetry of the ring is disturbed), then both modes should again be excited and the slight splitting of the modes should be easily detected [74]. A different result was however found when analysing a symmetrical ring structure with a coarse asymmetric mesh discretisation—an undesirable mode splitting occurred.

The test problem consisted of a microstrip ring resonator with mean ring radius $R = 7.475$ mm and a normalised ring width $w/R = 0.1$. The dielectric substrate has a relative permittivity of $\epsilon_r = 10.2$ and thickness $h = 0.635$ mm. The coupling lines were arranged symmetrically with a coupling gap size of $g = 0.1h$ and the port lengths and widths were $pL = 8.2$ mm and $pW = 1.4328$ mm respectively. No dielectric or surface losses were included in the calculations and the problem was discretised into 87 asymmetrically spaced triangles.

Fig. 4.10(a) shows the S-parameter response around the TM_{110} resonant frequency for a -70 dB and a -80 dB error in the interpolant. For the -80 dB error case, an unexpected mode splitting is observed, in this case traceable to a slightly assymetric MoM solution. However, this phenomenon is absent from the -70 dB error case, where the accuracy of the fit is only slightly worse. Using a finer symmetric discretisation of 200 triangles, mode splitting was eliminated and only a single mode was successfully excited.

The surface current magnitudes at first resonance were analysed and plotted along symmetrical lines around the ring. The currents, as shown in Fig. 4.10(b), are anti-metrical around the ring. Upon mirroring one set of data around the zero position, it was found that the currents indeed

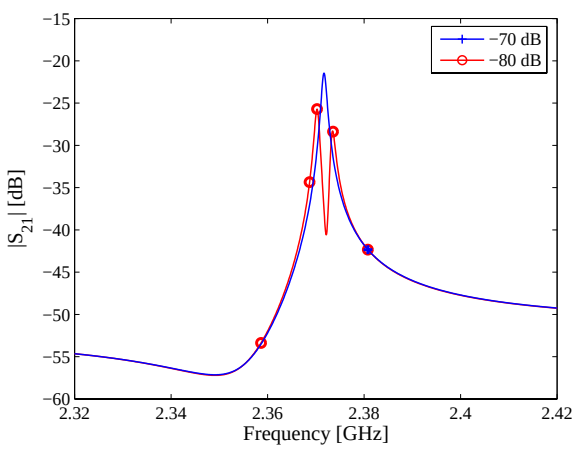

(a) Unwanted mode splitting visible at the first resonant mode, TM_{110}.

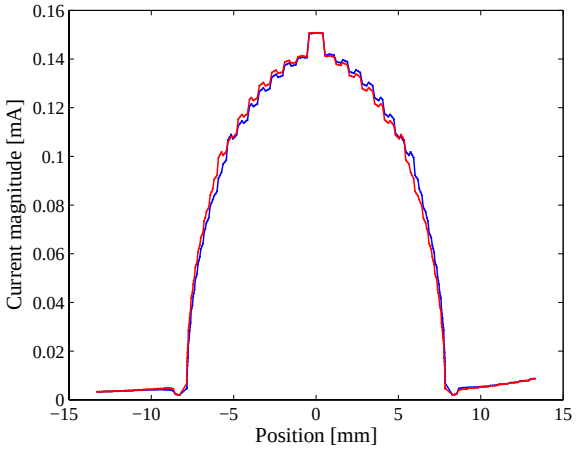

(b) Surface current magnitude along symmetrical lines around the ring.

Fig. 4.10. Mode splitting caused by slightly assymetric MoM solution.

matched each other. Also, the differences in symmetry becomes more as one moves away from the resonant point.

It is therefore clear that when doing this type of analysis, care has to be taken when selecting the combination of mesh size and minimum error bound. Fortunately, in practical problems involving loss, the simulation becomes less sensitive to a particular discretisation where splitting becomes invisible or unnoticable below the S-parameter skirts.

4.3 Conclusion

In this chapter two univariate rational interpolation models, the Thiele-type continued fractions and Vector Fitting pole-residue approaches, were exploited to accurately predict the resonance frequencies of a microwave ring resonator. Calculation of this characteristic f_0 was performed using two techniques—one predicting the natural frequencies of an unloaded resonator (eigenmode problem) and the other using the S-parameter response of a loosely coupled loaded resonator.

For the unloaded problem, the CEM solution required finding the zeros of an eigenvalue equation. Firstly, using MoM, this required the development of a new frequency dependent scaling constant to ensure evaluation to a viable solution to be used with interpolation techniques. Next, three methods were proposed and compared to calculate pole-free solutions to the Thiele and Vector Fitting models. Numerical difficulties and the existence of improper solutions to the eigenmode function were discussed, and convergence effects due to finite meshing were investigated. Finally, the inclusion of different components of loss in the model and the prediction of higher-order resonances was investigated and compared to current techniques.

For the loaded problem, an algorithm for the extraction of the resonant frequencies from a rational approximation of the scattering parameter magnitude plot was developed, and the results were compared to predictions obtained from measurements and commercial software simulations. Also, correctness of the interpolant and asymmetries in the discretisation causing mode splitting was investigated and discussed.

Results suggest that resonance frequencies can be accurately predicted by modelling either an unloaded resonator or a loosely coupled loaded resonator. To identify each one of the mode frequencies, however, it is advised to solve the unloaded eigenmode problem using Vector Fitting and the SER eigenvalue method of root-finding. The technique is robust, can handle noise in the data and provides a direct solution to finding the resonance frequencies. On the contrary, automated extraction of resonance frequencies from an S-parameter magnitude response is far more difficult. In addition, some resonances are left unidentified as their peak response cannot be differentiated from below the skirts of nearby, more strongly coupled, resonances. Due to ability

of Vector Fitting to compensate for numerical noise, it is recommended to use the technique instead of the Thiele fitting function in modelling the S-parameter response.

In Chapter 5, the univariate rational interpolant of the Thiele continued fraction will be further exploited to accurately predict the important resonator characteristic of Q-values.

Chapter 5

Calculation of Q-Factors

The second parameter of importance for microwave resonators is the Q-value. As a measure of the loss in a resonator, the quality factor is defined as the ratio of maximum energy $W_{\max}$ stored within a system to the power dissipated P_d in the system

$$Q = 2\pi f_0 \frac{W_{\max}}{P_d}. \tag{5.1}$$

A number of methods for Q-factor measurement and calculation exist, and are usually based on measurements of various types of system response: impedance [75–78], power [79] and S-parameters [80–84]. For the case of an unloaded resonator enclosed in a metal cavity, the Q-factor can most accurately be calculated by directly evaluating the definition in Eq. 5.1. The total energy stored at resonance may be found by taking a volume integral over the squared peak magnetic fields, and computation of the dissipated power requires integration of the squared magnetic fields over the entire metal surface of the cavity. Even though commercial packages successfully utilise this direct method for limited topologies, the method requires the computationally expensive use of an accurate full-wave EM evaluation of the field distribution over the complete volume of interest. For open structures such as microstrip, the computational expense is even greater as the volume has to now include all of the surrounding fields.

Because of the dominating effect of a resonator on circuit response in the vicinity of resonance, many techniques for Q-factor extraction rely on the fitting of response data to simplified network models. The simplest expression for determining the loaded quality factor of a resonator is the 3-dB "three frequencies" method as derived from a 3-element *RLC* equivalent circuit. The Q-factor is a ratio of the resonant frequency to the difference between the upper and lower 3 dB frequency points. Although often used, this expression is based on a simple approximation and will deviate for resonators with multiple resonant points since nearby resonances will affect the 3 dB values of the particular resonance being considered.

The more popular Q determination techniques rely on a Foster network type of formulation, where the quality factors are obtained by fitting a circle to multi-frequency S-parameter data.

This is a more accurate method than the 3-dB point expression for determining Q, since all points around the resonant frequency contribute to the definition of the circle. One of the more successful methods, the transmission mode quality factor (TMQF) fitting procedure, was developed by Leong [84] in 2002. The technique is based on equations derived for resonators working in the transmission mode and fractional linear circle-fitting techniques. The TMQF is of great use in calculating Q-values from measurement. Q-factor measurement techniques have been developed based on ideal models of resonator systems. In [84], Leong gives an overview on the effects that may influence the S-parameters of dielectric resonators. These include noise, electrical delay introduced by transmission lines, losses due to uncalibrated transmission lines and coupling structures, impedance mismatch and crosstalk. Some of the effects can be eliminated through a calibration procedure while other distortions need to be accounted for by adjusting and incorporation into the model. The TMQF method was developed to address most of these parasitic measurement effects. For a single resonator working in the transmission mode, a least-squares solution of the system provides the Q-factors as a function of the curve parameters. The procedure involves relating the S-parameters with the loaded quality factor Q_L, the coupling coefficients β and the overall resonant frequency f_L through the use of a circuit model (Fig. 5.1).

As with the calculation of f_0, interpolation-based models can be used to good effect to calculate Q-values. Applied to the TMQF fitting method, the rational interpolation model of the S-parameter response can be used to accurately and efficiently generate multiple data samples in the vicinity of resonance for use in the least-squares solution. These data samples are found at no additional CEM cost. An alternative approach, based on the same Thiele rational interpolant of the S-parameters as calculated in the previous chapter, can also be used for the prediction of Q-factors. This new three-point rational interpolation method, which uses only three of these Thiele coefficients at a time, provides a direct fit and solution to the Q-factors, again without any additional CEM effort. In Section 5.2 the theory for the three-point method is developed and verified. Advantages and problems encountered with this formulation are discussed and comparative results with the TMQF method and measurements are shown.

5.1 Transmission Mode Quality Factor (TMQF) Technique [84]

The theory of the TMQF technique was first presented in 2002. To derive equations relating the S-parameters to the loaded quality factor Q_L, the coupling coefficients β_1 and β_2 and the overall resonant frequency f_L, the circuit model of a transmission-mode resonator as shown in Fig. 5.1 has been used.

The three components R_0, L_0 and C_0 of shunt admittance Y_0 represent the ideal resonator. The

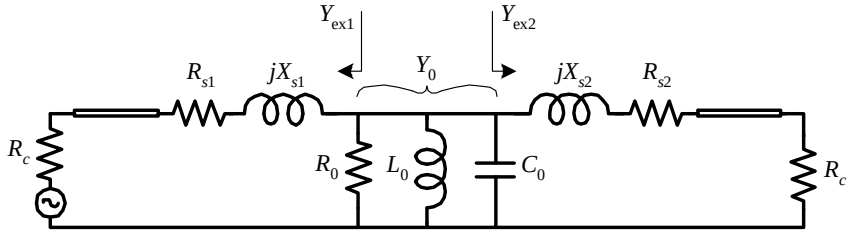

Fig. 5.1. Circuit model of a transmission resonator system.

shunt elements determine the unloaded quality factor of the system that can be described as

$$Y_0 = \frac{1}{R_0}\Big(1 + j2Q_0\frac{f - f_0}{f_0}\Big), \tag{5.2}$$

when using the narrow-band approximation $f^2 - f_0^2 \approx 2f\Delta f$. Here Q_0 is the unloaded quality factor of the ideal resonator and the resonant frequency f_0 is given by

$$f_0 = \frac{1}{2\pi\sqrt{L_0C_0}}. \tag{5.3}$$

The admittances Y_{ex1} and Y_{ex2} are external admittances as seen towards each port of the resonator

$$Y_{exp} = \frac{1}{R_{sp} + R_c + jX_{sp}} = G_{\text{exp}} + jB_{\text{exp}}, \tag{5.4}$$

where p denotes the input and output ports respectively. Resistances R_{s1} and R_{s2} represent losses of coupling structures, connectors, and losses of transmission lines connected to the two ports of the resonator, while reactances of the coupling structures are modelled by X_{s1} and X_{s2}. The resistance R_c represents an internal resistance of a microwave source, a load resistance and the characteristic impedance of transmission lines at both ports.

The circuit diagram of Fig. 5.1 can be seen as a cascaded connection of three networks. The S-parameters of the total resonator system can then be obtained from the ABCD-parameters as

$$S_{21} = \frac{2R_c}{AR_c + B + CR_c^2 + DR_c} = \frac{2R_cY_{\text{ex1}}Y_{\text{ex2}}}{Y_{\text{ex1}} + Y_{\text{ex2}} + Y_0}. \tag{5.5}$$

The denominator of Eq. 5.5 is equal to the total circuit admittance Y_L and the resonant frequency f_L of the loaded resonator can be found by assuming the imaginary part of Y_L to be zero

$$f_L = f_0\Big(1 - \frac{B_{\text{ex1}} + B_{\text{ex2}}}{2Q_0G_0}\Big). \tag{5.6}$$

Near resonance, the complex transmission coefficient S_{21} can be expressed in terms of the loaded quality factor Q_L, the coupling coefficients and frequency

$$S_{21}(f) \approx \frac{2R_cY_{\text{ex1}}Y_{\text{ex2}}}{G_0(1 + \beta_1 + \beta_2)\Big(1 + j2Q_L\frac{f - f_L}{f_L}\Big)}, \tag{5.7}$$

where β_1 and β_2 are the coupling coefficients of the loaded resonator and are defined as a ratio of the external power dissipated to power dissipated in the system

$$\beta_1 = \frac{G_{\text{ex1}}}{G_0} \text{ and } \beta_2 = \frac{G_{\text{ex2}}}{G_0}, \tag{5.8}$$

and for resonators working in the transmission mode

$$Q_0 = Q_L(1 + \beta_1 + \beta_2). \tag{5.9}$$

The relationship between the reflection parameter S_{11} and the loaded quality factor Q_L is given by

$$S_{11}(f) \approx \frac{j2Q_L S_{11d}\dfrac{f - f_L}{f_L} + \left(S_{11d} + \dfrac{2R_c Y_{ex1}^2}{G_0(1 + \beta_1 + \beta_2)}\right)}{j2Q_L\dfrac{f - f_L}{f_L} + 1}, \tag{5.10}$$

where S_{11d} represents the detuned value of the reflection coefficient at the port when the frequency is far from f_L.

The above derivation shows that both the transmission coefficient S_{21} (Eq. 5.7) and the reflection parameter S_{11} (Eq. 5.10) have a fractional linear form in the region of resonance

$$S_{ij} = \frac{a_1 t + a_2}{a_3 t + 1}, \tag{5.11}$$

where $t = 2(f - f_L)/f_L$ is a normalised frequency variable. A least-squares solution of the system provides the Q-factor as a function of the complex curve parameters a_1, a_2 and a_3, and the loaded quality factor can be found directly as the imaginary part of a_3 ($Q_L = \mathrm{Im}\{a_3\}$). As a result the loaded quality factor for transmission-mode resonators can be found from either the transmission or reflection responses. Note that $a_1 = 0$ when working with S_{21}.

One problem with the method in [84] is that the parameters a_i are dependent on the frequency span used. For wide spans, the order of the rational function is simply too low to fit the curve accurately. To solve this, a reduced frequency span should be used. The effect of an excessively wide frequency span on the Q-value of a resonator was investigated by calculating the quality factor for decreasing frequency spans and computing an associated maximum error $\sum(|(a_1 t + a_2)/(a_3 t + 1) - S_{ij}|^p)/N$ between the S-parameter response and the fitting curve obtained. Fig. 5.2 shows the results of this experiment, plotting the loaded quality factor against error. Converged Q-factor values of 1636.0 and 1640.3 were extracted from the transmission and reflection responses, respectively. Note that the Q-factor extracted from the transmission response remains constant over a far wider frequency span than for the reflection response, making Q-factor extraction from the S_{21} response the preferred option. When using this technique of frequency band shrinking and error calculation, the transmission mode quality factor (TMQF) technique was found to be a robust tool for accurate calculation of the loaded quality factors.

The TMQF method calculates the loaded quality factor Q_L. To fully characterise a resonator, the unloaded quality factor Q_0 (Eq. 5.9) should be determined. This requires calculation of the coupling coefficients β_1 and β_2, as discussed in [84]. Under weak coupling conditions, however, the reflection Q circles are too small to yield reliable results and the unloaded quality factor

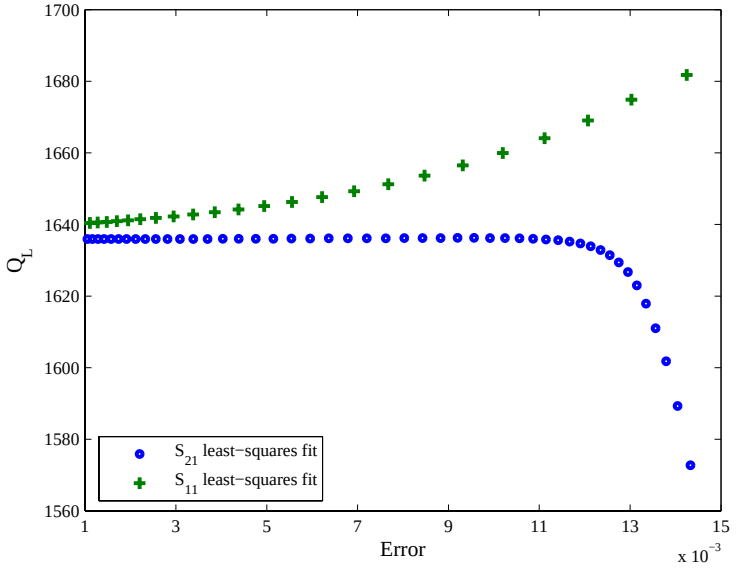

Fig. 5.2. Convergence results of the loaded quality factor calculated using the TMQF technique on both transmission and reflection responses.

have to be approximated by the loaded quality factor ($Q_0 \approx Q_L$). As both coupling coefficients are very small for this case, this does not affect the unloaded Q adversely. Also, the noise in the reflection trace is usually significantly higher than in the transmission trace, and measurements with low coupling result in a low SNR ratio that may affect the accuracy of the measurements. Hence, according to [84] it is desirable to use sufficiently high levels of coupling.

In [83], an uncertainty analysis of the transmission-type measurement of Q-factors has been presented, suggesting the opposite, i.e. overcoupled resonators have considerably larger uncertainty in Q_0 than in Q_L, where undercoupled resonators have approximately the same uncertainty in Q_0 than in Q_L. Using this method of insertion-loss, the unloaded quality factor is calculated as

$$Q_0 = \frac{Q_L}{1 - 10^{-L/20}}, \tag{5.12}$$

where L is the insertion loss in dB at resonance. This method assumes the input and output couplings to be identical to each other. Eq. 5.12 is widely used and generally gives accurate results, provided the coupling is small [74]. As such, this method of approximating Q_0 will be used in this chapter.

5.2 Three-Point Rational Interpolation Method [26]

The problem with the standard TMQF fitting method is that the technique relies on least-squares fits, which normally require a large number of frequency points in the vicinity of resonance. A new method, using the previously calculated coefficients of the S-parameter Thiele interpolant (Chapter 4.2), is proposed that eliminates the need for a least-squares fit. The proposed technique, called the three-point rational interpolation method, uses only three of the interpolant

coefficients at a time, to obtain Q-factors without any additional CEM effort. The method provides a direct fit and solution to the Q-values.

In the rational interpolation formulation, the Thiele continued fraction (Eq. 3.2) for 3 support points, $\Re_2(f)$, has the form

$$\Re_2(f) = H_0 + \cfrac{f - f_0}{\varphi_1(f_1, f_0) + \cfrac{f - f_1}{\varphi_2(f_2, f_1, f_0)}}. \tag{5.13}$$

In the vicinity of resonance, $\Re_2(f)$ can be changed into the form of $\Re_2(t)$, which has the exact same form as Eq. 5.11 for the reflection response (i.e. $a_1 \neq 0$).

With t the normalised frequency variable

$$t = 2\frac{f - f_L}{f_L} \tag{5.14}$$

and f_L the loaded resonant frequency, it follows that

$$\Re_2(t) = \frac{\left[\dfrac{f_L(H_0 + \varphi_2)}{2(\varphi_1\varphi_2 - f_1 + f_L)}\right] t + \left[S_0 + \dfrac{\varphi_2(f_L - f_0)}{\varphi_1\varphi_2 - f_1 + f_L}\right]}{\left[\dfrac{f_L}{2(\varphi_1\varphi_2 - f_1 + f_L)}\right] t + 1}. \tag{5.15}$$

Since all the interpolant coefficients are known, the parameters a_1, a_2 and a_3 can be extracted directly from the reflection response and the need for a least-squares fit is eliminated. Also, the loaded quality factor is readily available and equal to the imaginary part of parameter a_3

$$Q_L = \mathrm{Im}\{a_3\} = \mathrm{Im}\left\{\frac{f_L}{2(\varphi_1(f_1, f_0)\varphi_2(f_2, f_1, f_0) - f_1 + f_L)}\right\}. \tag{5.16}$$

Since this technique uses only three of the original interpolant samples to model the S-parameter response in the vicinity of resonance, these support points should be chosen carefully. With the Thiele fitting function required to pass through each support sample, it follows that a support point (f_i, H_i) has the largest influence on the interpolant near the frequency f_i. Hence, the obvious choice is to select the three support samples closest to the resonant frequency f_L. Fig. 5.3 shows an example fit achieved by using the three-point interpolant. A quality factor of $Q_L = 937.7$ was extracted, which agrees well with the values of 942.2 and 951.3 obtained using the TMQF technique on the transmission and reflection responses respectively.

However, when using adaptive sampling there is no means of ensuring that there will indeed be at least three support samples in close proximity of the resonant frequency. The three-point interpolant may then differ substantially from the original model, yielding incorrect results. Fig. 5.4 illustrates this incorrect fit, from which a loaded quality factor of $Q_L = -146.6$ was extracted. This value is negative and not near the TMQF predictions of 1636.0 for the S_{21} fit and 1640.3 for the S_{11} fit. To improve this method, the contribution of each and every support point needs to be considered and incorporated into the model.

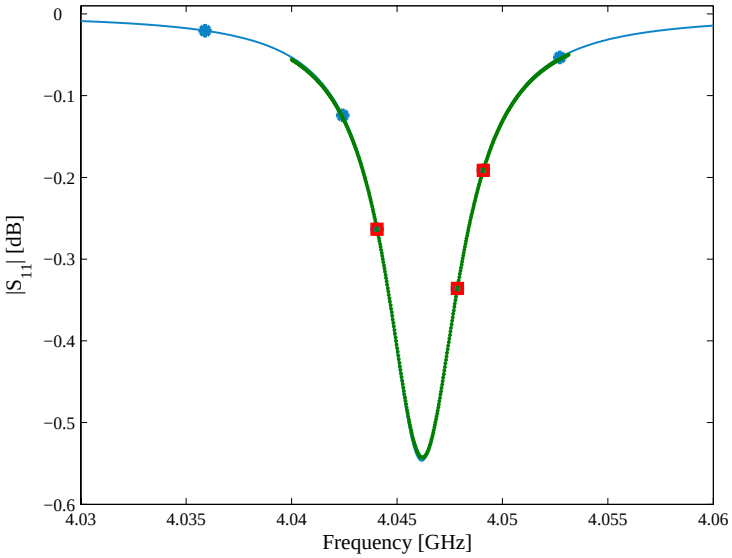

Fig. 5.3. Three-point rational interpolation fit on S_{11} data at $f_L = 4.0461$ GHz.

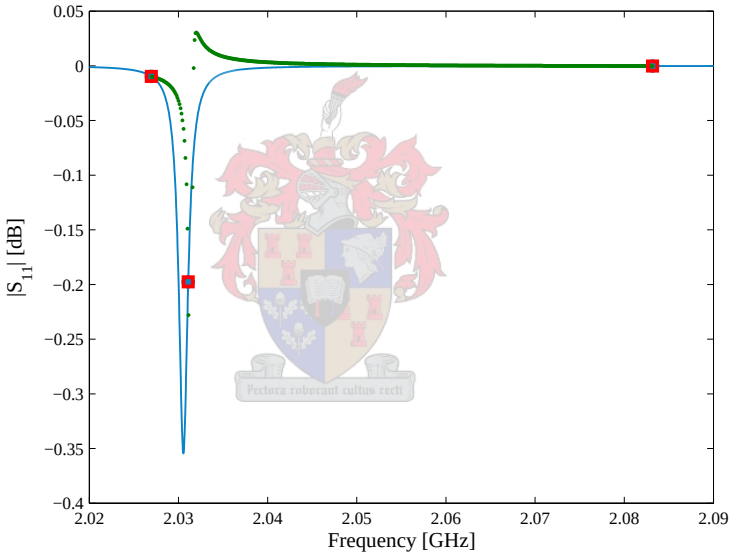

Fig. 5.4. Incorrect three-point rational interpolation fit on S_{11} data at $f_L = 2.0306$ GHz.

In the region of resonance, the interpolant term associated with a support point (excluding the two points closest to f_L) behaves as a constant. Therefore, the Thiele continued fraction $\Re_2(f)$ was extended to include the constant Θ as evaluated at f_L, to give

$$\Re_2(f) = H_0 + \frac{f - f_0}{\varphi_1(f_1, f_0) + \dfrac{f - f_1}{\Theta_{N_s}(f_L)}}, \tag{5.17}$$

where $N_s + 1$ is the total number of support points describing S_{11}. The constant $\Theta(f_L)$ has the same form as the original partial fraction expansion and can be evaluated using the same

recurrence formula

$$\begin{aligned} N_k(f_L) &= \varphi_k(f_k, f_{k-1}, \cdots, f_0)N_{k-1}(f_L) + (f_L - f_{k-1})N_{k-2}(f_L) \qquad k = 4, 5, \cdots, N_s \\ D_k(f_L) &= \varphi_k(f_k, f_{k-1}, \cdots, f_0)D_{k-1}(f_L) + (f_L - f_{k-1})D_{k-2}(f_L) \qquad k = 4, 5, \cdots, N_s \\ \Theta_k(f_L) &= \frac{N_k(f_L)}{D_k(f_L)} \qquad k = 2, 3, \cdots, N_s, \end{aligned} \tag{5.18}$$

but with different starting conditions $N_2(f_L) = \varphi_2(f_2, f_1, f_0)$,
$N_3(f_L) = \varphi_3(f_3, f_2, f_1, f_0)N_2 + (f_L - f_2)$, $D_2(f_L) = 1$ and $D_3(f_L) = \varphi_3(f_3, f_2, f_1, f_0)$.

Note that the interpolant passes through the point of resonance (f_L, H_L) and also the support points H_0 and H_1. For a best fit these are selected as the two support points closest to f_L. After transforming Eq. 5.17 to the form of Eq. 5.11[†], the loaded quality factor is given by

$$Q_L = \mathrm{Im}\{a_3\} = \mathrm{Im}\left\{\frac{f_L}{2(\varphi_1(f_1, f_0)\Theta_N(f_L) - f_1 + f_L)}\right\}. \tag{5.19}$$

Fig. 5.5 plots the improved three-point solutions as calculated at the two test resonance frequencies discussed in Figs. 5.3 and 5.4. The method yielded Q-values of 1662.7 at $f_L = 2.0306$ GHz and 949.2 at $f_L = 4.0461$ GHz. These results are within 1.6% of the values predicted with the TMQF least-squares fit.

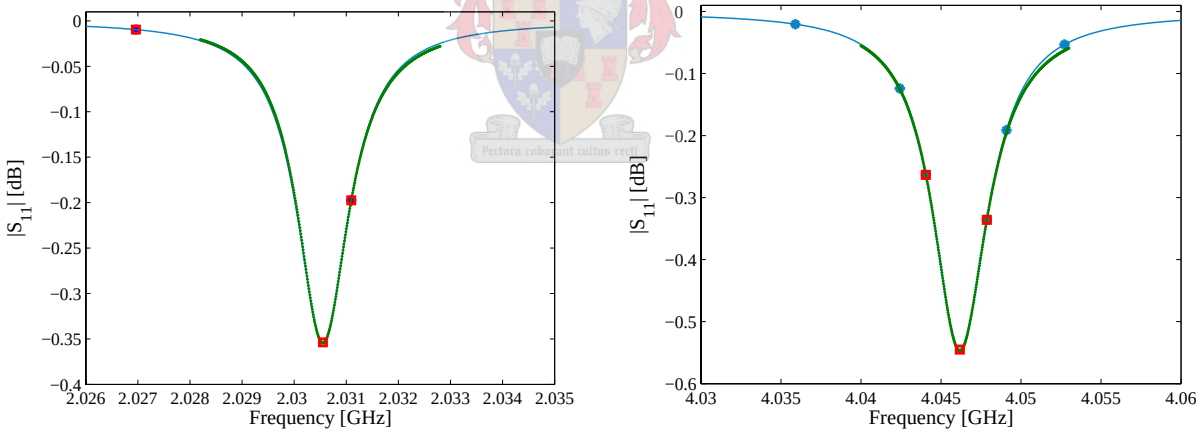

(a) $f_L = 2.0306$ GHz. (b) $f_L = 4.0461$ GHz.

Fig. 5.5. Improved three-point rational interpolation fit on S_{11} data.

5.2.1 Study 1—Verification of the Three-Point Method

In this study the three-point rational interpolation method is verified theoretically for both high-Q and low-Q values. The basic ring structure selected for this test study is that of Ring #1 ($R = 16.9$ mm, $w/R = 0.1$) described in Section 4.2.1, and supports only the TM_{n10} modes that are widely spaced in frequency. The three-point method computes the loaded quality factor of a resonator. To establish high values of Q_L, losses were suppressed by setting $\tan(\delta) = 0$, surface

[†]The result is obtained by a simple interchange from $\varphi_2(f_2, f_1, f_0)$ to $\Theta_N(f_L)$ in Eq. 5.15.

roughness $\Delta = 0$ and assuming ideal conductors $Z_s = 0$, leaving only radiation loss. To simulate lower values of Q_L, stronger coupling was enforced by decreasing the coupling gap size to $g = 0$. Tables 5.1 and 5.2 list the loaded quality factors extracted using both the least-squares TMQF approximation and the two variants of the three-point rational interpolation method.

Quality factors Q_L were computed at the first four mode frequencies. In Table 5.1 the higher Q-values agree to within 1.8%. Note that the three-point method at 2.0306 GHz predicted an incorrect negative value of -146.6 while the improved three-point method provided a good estimate of $Q_L = 1662.7$. In Table 5.2, the lower Q-values agree to within 2.7% when discarding the value obtained at the TM_{110} mode frequency. Differences in the predictions at this fundamental resonant frequency is the result of a weakened coupling, which means the reflection Q-circle is too small to yield reliable results. Also, according to [84], the range of Q-factors measureable with the TMQF technique is from 10^3 up to 10^7, as applied to dielectric resonators. In this example, however, the fitting methods have been tested to predict extremely small values of Q.

It is important to realise at this point that one of the greatest disadvantages of the three-

TABLE 5.1
COMPARISON OF LOADED Q-FACTORS (HIGH-Q VALUES) CALCULATED WITH THE TRANSMISSION MODE QUALITY FACTOR (TMQF) TECHNIQUE AND THE THREE-POINT RATIONAL INTERPOLATION METHODS.
(SUBSTRATE PARAMETERS: $h = 0.508$ mm, $\epsilon_r = 2.17$, $\tan(\delta) = 0$;
RING PARAMETERS: $R = 16.9$ mm, $w/R = 0.1$, $g = 0.7h$, $pL = 3$ mm, $pW = 1.53$ mm;
SURFACE ROUGHNESS: $\Delta = 0$; CONDUCTOR LOSSES: $Z_s = 0$)

Resonant Mode	Resonant Frequency [GHz]	TMQF		Three-Point Method	Improved Three-Point Method
		S_{21}	S_{11}	S_{11}	S_{11}
TM_{110}	2.0306	1636.0	1640.3	-146.6	1662.7
TM_{210}	4.0461	942.1	951.3	937.7	949.2
TM_{310}	6.0573	780.7	788.6	798.9	794.8
TM_{410}	8.0717	693.8	696.2	697.2	701.0

TABLE 5.2
COMPARISON OF LOADED Q-FACTORS (LOW-Q VALUES) CALCULATED WITH THE TRANSMISSION MODE QUALITY FACTOR (TMQF) TECHNIQUE AND THE THREE-POINT RATIONAL INTERPOLATION METHODS.
(SUBSTRATE PARAMETERS: $h = 0.508$ mm, $\epsilon_r = 2.17$, $\tan(\delta) = 0.0011$;
RING PARAMETERS: $R = 16.9$ mm, $w/R = 0.1$, $g = 0$, $pL = 3$ mm, $pW = 1.53$ mm;
SURFACE ROUGHNESS: $\Delta = 3.5$ μm)

Resonant Mode	Resonant Frequency [GHz]	TMQF		Three-Point Method	Improved Three-Point Method
		S_{21}	S_{11}	S_{11}	S_{11}
TM_{110}	2.0509	3.11	3.37	3.08	2.73
TM_{210}	4.0814	6.07	6.19	6.30	6.24
TM_{310}	6.1351	9.20	9.27	9.64	9.49
TM_{410}	8.1672	12.56	12.64	14.16	12.50

point rational interpolation method is that the fitting procedure is applied to the reflection parameter S_{11}. As was explained in Section 5.1, the noise in the reflecion response is usually significantly higher than in the transmission response. Also, as was seen in the previous example, the reflection Q-circles become too small and poorly defined under weak coupling conditions to make any meaningful predictions.

To investigate this issue, the unloaded quality factors Q_u for Ring #1 ($R = 16.9$ mm, $w/R = 0.1$) were computed while considering different coupling conditions. The results are listed in Table 5.3 for coupling gap sizes varying between $g = 0$ and $g = 0.3h$. The model includes the various loss components with $\tan(\delta) = 0.0011$, $Z_s = (1 + j)/(\sigma_{\text{eff}}\delta)$ and a uniform surface roughness of $\Delta = 3.5$ μm. A discussion on interesting characteristics that emerged from the study follows below.

Accuracy

i) Coupling increases as frequency increases. As such, coupling is the weakest at the fundamental resonance frequency, resulting in the worst Q-circle fit and the least accurate results. For $g = 0$ and $g = 0.2h$, only a single support point in close vicinity of the TM_{110} mode frequency was needed to establish an accurate S-parameter response, which is of course insufficient for Q-value extraction. This means that a higher accuracy model with more support points may be needed to correctly extract the Q-values than to generate an accurate S-parameter response.

ii) Weaker coupling means smaller reflection Q-circles and inaccurate results. Comparing only the TMQF predictions for the transmission and reflection responses, it is clear that the Q-values predicted using the S_{21} trace remain constant as expected for Q_u values while the Q-values predicted using the S_{11} response increase in magnitude. Differences of up to 14% are recorded for the $g = 0.3h$ case. Thus, under weak coupling conditions, it is preferable to use the transmission S_{21} response to compute quality factors.

iii) When comparing the S_{11} predictions for the TMQF technique and the improved three-point method, the Q-values are in good agreement with a maximum difference of 5.9%. Thus, under sufficiently high levels of coupling, the improved three-point method may be utilised to accurately predict resonator Q-factors. This can be seen from the $g = 0$ (high coupling) case where the S_{21} and S_{11} predictions are within 3% of each other.

Conclusion The three-point rational interpolation method has been verified to extract the Q-values of both high- and low-Q resonators. Under loose coupling conditions, however, the technique falls short of giving accurate predictions, as the reflection Q-circles are too small to predict reasonable values. As Q-factor extractions from S_{21} transmission responses are more reliable and less sensitive to the feed line coupling strength and frequency span used in the fitting approximation, the use of the TMQF technique to extract Q-values from the S_{21} response is recommended instead. In addition, it is proposed that the S-parameter interpolation model be

TABLE 5.3
UNLOADED Q-FACTORS CALCULATED FOR RING #1 WITH DIFFERENT COUPLING CONDITIONS.
(SUBSTRATE PARAMETERS: $h = 0.508$ mm, $\epsilon_r = 2.17$, $\tan(\delta) = 0.0011$;
RING PARAMETERS: $R = 16.9$ mm, $w/R = 0.1$, $pL = 3$ mm, $pW = 1.53$ mm;
SURFACE ROUGHNESS: $\Delta = 3.5$ μm)

(a) $g = 0$.

Resonant Mode	Resonant Frequency [GHz]	TMQF		Improved Three-Point Method
		S_{21}	S_{11}	S_{11}
TM_{110}	2.0509	151.1	163.9	132.7
TM_{210}	4.0814	159.8	163.0	164.3
TM_{310}	6.1351	165.7	166.8	170.8
TM_{410}	8.1672	168.4	169.6	167.6

(b) $g = 0.1h$.

Resonant Mode	Resonant Frequency [GHz]	TMQF		Improved Three-Point Method
		S_{21}	S_{11}	S_{11}
TM_{110}	2.0248	152.7	168.1	175.9
TM_{210}	4.0366	163.7	175.8	180.5
TM_{310}	6.0389	171.4	183.3	185.9
TM_{410}	8.0554	178.8	191.3	194.9

(c) $g = 0.2h$.

Resonant Mode	Resonant Frequency [GHz]	TMQF		Improved Three-Point Method
		S_{21}	S_{11}	S_{11}
TM_{110}	2.0251	152.7	172.3	221.0
TM_{210}	4.0371	163.7	178.7	177.5
TM_{310}	6.0397	171.2	186.0	188.8
TM_{410}	8.0563	178.5	194.1	195.2

(d) $g = 0.3h$.

Resonant Mode	Resonant Frequency [GHz]	TMQF		Improved Three-Point Method
		S_{21}	S_{11}	S_{11}
TM_{110}	2.0253	152.6	177.7	188.8
TM_{210}	4.0375	163.7	182.3	189.4
TM_{310}	6.0403	171.0	189.1	183.8
TM_{410}	8.0571	178.3	197.5	200.4

utilised to accurately and efficiently generate the large number of data samples required by the least-squares approximation, at no additional CEM cost.

5.2.2 Study 2—Experimental Verification

Extraction of Q-values from measurement is essential when establishing the quality of the numerical model used. As the Q-factor is a measure of the loss in a resonator, all components of loss should be included in the model to accurately predict Q-values. In this study, the Q-factors of the two ring resonators of Section 4.2.1 are investigated. These two rings, referred to as Ring #1 ($R = 16.9$ mm, $w/R = 0.1$) and Ring #2 ($R = 16.9$ mm, $w/R = 0.6$), were manufactured using Taconic TLY-5A substrate with manufacturer specifications of $\epsilon_r = 2.17$

TABLE 5.4
Comparison of unloaded Q-factors calculated from measurements and extracted with the Transmission Mode Quality Factor (TMQF) technique and the improved three-point rational interpolation method. (MoM parameters: $\tan(\delta) = 0.0011$; $\Delta = 3.5$ μm)

(a) Ring #1. (Ring parameters: $R = 16.9$ mm, $w/R = 0.1$)

Resonant Mode	Measurements	TMQF		Improved Three-Point Method
	S_{21}	S_{21}	S_{11}	S_{11}
TM_{110}	145.2	151.1	163.9	132.7
TM_{210}	149.3	159.8	163.0	164.3
TM_{310}	157.8	165.7	166.8	170.8
TM_{410}	179.8	168.4	169.6	167.6

(b) Ring #2. (Ring parameters: $R = 16.9$ mm, $w/R = 0.6$)

Resonant Mode	Measurements	TMQF		Improved Three-Point Method
	S_{21}	S_{21}	S_{11}	S_{11}
TM_{110}	93.4	88.3		
TM_{210}	104.5	91.9	108.4	115.3
TM_{310}	114.8	107.8	120.5	120.1
TM_{120}	66.4	55.6		
TM_{410}	129.6	121.5	135.9	140.9

and $\tan(\delta) = 0.0009$. To extract the Q-values from measurement, a Vector Fitting model is generated based on the measurement data. This filters out the noise from the measurement and ensures proper calculation of the insertion loss L at resonance, as required by Eq. 5.12.

All components of loss should be included in the MoM simulation to compute Q-values accurately. The loss parameters used throughout the MoM simulations were $\tan(\delta) = 0.0011$ (compared to data sheet value of 0.0009) and a uniform surface roughness of $\Delta = 3.5$ μm. Also, all scatterers and ground planes were assumed lossy. The comparative results for the microstrip resonators are listed in Table 5.4.

The predicted Q-factors (improved three-point method) are within 10.0% and 10.5% of the Q-values extracted from the measurement traces for Ring #1 and Ring #2 respectively. Note that the higher-order TM_{120} mode has a much lower Q-value than the various TM_{n10} modes. It was found that coupling to these higher-order modes is a lot less than for the fundamental mode series, which makes extraction of the Q-values at these mode frequencies using the S_{11} trace less favourable. Both the TM_{110} and the TM_{120} reflection Q-circles were too small to make any meaningful predictions. These results show that the MoM model succesfully accounts for most components of loss. Dielectric losses are accounted for by inclusion of the substrate dissipation factor, while conductor losses are affected by the surface roughness value used. In this open structure, radiation losses dominate over the lesser surface wave losses to finally give Q-factors of average value.

5.3 Conclusion

In this chapter, the calculation of Q-values using rational interpolation models has been investigated.

A new three-point rational interpolant function in the region of resonance was proposed. This technique utilises the already known interpolant coefficients of the S-parameter response of a resonator, and provides a direct fit and solution to the Q-factors. A disadvantage to the method is that the technique cannot be applied to noisy measurement data. The technique is based on the S_{11} reflection parameter, which becomes ill-defined under low coupling conditions and yields unreliable results. It is suggested that the three-point Q-extraction technique be used with high-Q resonators instead. The more feasible solution would, however, be to utilise the robust TMQF fitting method as applied to the S_{21} transmission response, but to exploit the efficiency of a rational interpolant to gather the large number of data samples required by this technique.

Chapter 6

Multi-Dimensional Adaptive Interpolation

In the preceding chapters, it was shown that one-dimensional adaptive rational interpolation techniques can be used to good effect in calculating resonance frequencies and Q-values. As the accurate prediction of these resonator characteristics is of primary importance in the modelling of resonators, the extension of one-dimensional interpolation techniques to multi-dimensional interpolation techniques demands further investigation.

In recent years, the problem of creating multi-dimensional models for system responses of microwave structures from EM simulations has received considerable attention. One of the main goals of this multi-dimensional research is to create techniques that allow the building of parametric models for components using as few data points as possible. Examples of techniques which can be used to achieve this goal include look-up tables [85], artificial neural networks (ANN) [86], circuit models and equation-based mathematical models.

Look-up tables [85] require the up-front calculation of a number of data points on a multi-dimensional fixed grid. These data points are stored in a database of which the storage space increases exponentially as the dimension increases. To compute values between grid points, low order polynomial (simple linear or quadratic) interpolation techniques are often used. Hence, these techniques can only handle mild fluctuations and have difficulty modelling the frequency behaviour of resonant structures. In addition, the number and selection of the data points is non-optimal and may lead to a poor model quality (undersampling) and questionable accuracy, or a waste of computational resources (oversampling).

Techniques based on artificial neural networks [86] have the ability to handle highly non-linear behaviour and models of high dimension, since the size of the model does not increase exponentially with dimension. These techniques do however have some serious drawbacks. It is hard to find a good suitable topology, and the number of hidden layers and nodes must be found by

trial and error. In addition, frequency behaviour is difficult to model and long training times can make the ANN difficult to apply in automated model generation procedures. Finally, there is also no easy method to ensure quality of the ANN model.

Automatic parameterised model creation was first presented in [7, 22, 87]. In this proprietary algorithm, called Multi-dimensional Adaptive Parameter Sampling (MAPS), a global analytical fitting model for the scattering parameters of general planar structures is built by separating frequency from other physical parameters. At selected frequency points, multi-dimensional models are created by expanding the multivariate functions into series of orthonormal multinomials (all using the same set of basis functions). The expansion coefficients are found by solving a system of interpolatory conditions, and support points are added in an entirely adaptive way. Orthonormal multinomials improve the numerical stability and efficiency of the interpolation, while the frequency dependence is added by one-dimensional rational interpolation of the model's response. The procedure creates models with a predefined accuracy, but sampling frequency separately from other physical parameters may result in a non-optimal number of support points.

Models can also be created in an automated fashion by interpolating EM data with multivariate rational functions. The most straightforward approach is to extend the univariate Cauchy method [5, 18], which allows adaptive selection of support points [4] and model order, to higher dimensions by setting up and explicitly solving a system of interpolatory conditions. These problems involving interpolation with non-orthogonal multinomials are, however, ill-conditioned [88] and are expensive to solve. Since the adaptive selection of support points and model order requires solving the system a number of times, the technique is considered computationally ineffective, inaccurate and suitable for simple models only [6]. In fact, Peik [6] shows the results only for two-dimensional models. For higher dimensions, a fast and stable recursive Bulirsch-Stoer algorithm [89] was developed in which the adaptive sampling can be applied only in one dimension and all other samples have to form a completely filled uniform or non-uniform grid. This implies that the number of full-wave analyses are high.

To reduce the number of support points while retaining the speed and stability of the interpolating algorithm, Lehmensiek [8, 14, 90] developed techniques based on the Thiele-type branched continued fraction representation of a rational function. The algorithms operate by using univariate adaptive sampling along a selected dimension. In this way, while the support points do not fill the grid completely, they are being added along straight lines passing through multi-dimensional space. The efficiency of the algorithms was illustrated on two- and three-dimensional models.

In 2003, Lamecki [9] showed that, despite earlier skepticism, multivariate rational interpolation that involves setting up and explicitly solving a system of interpolatory conditions, can be implemented in such a way that accurate high dimensional models can be created automatically

with support points added along all dimensions (including frequency) simultaneously. Stability and efficiency of the algorithm was achieved by using the total least-squares (TLS) [91] method for solving the interpolation equations combined with the QR row update procedure [91] and the monitoring of the interpolation error to detect convergence or potential instability. Compared to the three-dimensional models presented in [8], a significant four times reduction in the number of support points was achieved. Also, the quality of a five-dimensional model generated by the proposed technique was demonstrated.

Since 2003, the key difference between the various multivariate rational methods has been the approach used to evaluate the order of the multinomials and the coefficients that define them. In 2004, Dhaene [92,93] introduced constrained metamodelling, where certain dependencies may exist between (some of) the geometrical parameters, followed by Hendrickx [10,23] who presented a sequential design and adaptive methodology to capture the complex input-output behaviour of the simulator in a multivariate surrogate model. The author discusses the importance of suitable degree sets and builds a variety of models based on the sample sets by tuning the *weighting* (importance) of each variable, setting the *degrees of freedom* as a percentage of the number of samples and setting *polynomial/rational flags* to indicate which of the input variables should appear in the denominator. More importantly, Hendrickx introduced a model quality assessment by which each model's accuracy may be asserted. Most recently, Cuyt [11] constructed an interpolating rational function in such a way that it minimises both the truncation error and the model complexity (number of simulation data). The problem was also reformulated in terms of an orthogonal Chebyshev product basis, which addresses the severe ill-conditioning of the system when using the classical multinomial basis. Finally, the author also proposed that the rational model may be computed via a fast linear block Cauchy-Vandermonde-like solver, which can cope with the non-square block structure of the system and is as stable as Gaussian elimination with partial pivoting.

As shown in Chapters 4 and 5, models for resonators must primarily calculate f_0 and Q, and the present techniques which model system response becomes non-optimal in calculating these parameters. In this chapter, a new multivariate rational-multinomial combination interpolant is proposed to model multiple mode frequencies of microwave ring resonators simultaneously [29]. Unlike most of the above modelling techniques using either the S-parameter or Y-parameter responses of a loaded structure to build a model, the present approach is based on the solution of an eigenmode problem or unloaded structure—the main reasons being the difficulty with which maxima (mode frequencies) can be identified in an automated fashion, and the improbability of correctly identifying modes that are closely spaced (Section 4.2.1).

Similar to the MAPS [7] algorithm, frequency is separated from other physical parameters. However, even though excluding frequency from the adaptive sampling procedure may lead to a less optimal placement of support points, it becomes a prerequisite to finding a solution to

the proposed problem, as the complete parameter space is discontinuous across the physical dimensions. In Section 4.1 [26], the one-dimensional calculation of resonance frequencies by solution of the natural frequencies of an unloaded resonator was discussed. It was shown that the technique requires finding the roots of the characteristic equation

$$\Re(s) = \det[Z(s)] = 0 \tag{6.1}$$

and that the determinant needs to be scaled by a frequency dependent scaling constant. For the one-dimensional problem, this scaling factor poses no additional problems. When changing one of the physical parameters, however, the geometry needs to be remeshed requiring a different scaling factor and hence creates a discontinuous function across the physical parameter space.

Thus, building a $(d+1)$-dimensional model describing the complete function $\det[Z(s, \mathbf{X})]$ becomes improbable. However, the crux of the proposed algorithm lies in the fact that the resonance frequencies (zeros of Eq. 6.1) remain continuous across all dimensions, despite the discontinuity of the complete function. Therefore, instead of modelling the $(d+1)$-dimensional input space, the frequency dependence s is modelled separately employing the single input, single output adaptive rational Vector Fitting (VF) algorithm. This sampling loop is performed with the sole purpose of identifying the various mode frequencies, and only the zeros of the interpolant need to be entirely accurate. The d-dimensional physical dependence $\mathbf{X}$ is then added, building multiple input, multiple output multinomial metamodels describing the resonance behaviour of each of the modes.

Since Vector Fitting has proved to be a robust technique and lends itself to an elegant method for identifying the resonance frequencies correctly and accurately (Section 4.1 [27]), the author selected VF as the technique of choice to model the frequency behaviour. For the multi-dimensional geometrical interpolation, a combination of the methods proposed by Lamecki [9], Hendrickx [23] and Cuyt [11] is utilised. Although the model is approximated by an expansion in a set of multi-dimensional multinomials, any other complete set of basis functions could also be used. For the calculation of the frequency model, a new convergence criterion applied to the one-dimensional adaptive sampling algorithm presented by Lehmensiek [13] is introduced. Based on the position of the roots (resonance frequencies) of the rational model $\det[Z(s)]$, convergence is reached with a greater than 25% reduction in the number of support points required [28].

For automated mode identification, a method is proposed by which an identified resonance frequency is associated with a known resonant mode. The technique utilises correlation of the ideal current patterns, as created by the analytical equations describing the magnetic-wall model [56] in free-space, to the actual current pattern evaluated at the identified frequency. This technique has also been verified against a microwave square ring resonator.

Interpolation results are known to be valid only within the pre-defined parameter space. In some instances, one or more of the outputs may not exist across the entire parameter space.

To ensure that evaluation of the model is only performed in valid regions, a constrained grid modelling approach is introduced by which a convex hull around all valid support samples is found. This is followed by a discussion on the selection of a suitable degree set and model quality assesment [23] across this constrained evaluation grid.

The proposed algorithm is verified by presenting results for both two- and three-dimensional input models. Accuracy of the final model was also investigated by comparing predictions to the analytical solution of the magnetic-wall model. In this case the magnetic-wall model was also used to predict the resonance frequencies when building the metamodels. Accuracy of both interpolated and extrapolated results are discussed and a Monte Carlo statistical analysis was performed to assess the model quality across the complete parameter space. It is also shown that the models self-compensate if the root-finding algorithm should ignore one or more of the resonance frequencies.

6.1 The Algorithm

In this section the proposed algorithm is discussed in more detail, including a qualitative comparison to the multivariate rational metamodelling techniques of Lamecki [9], Hendrickx [23] and Cuyt [11]. Since these three techniques mainly differ in their approach used to evaluate the order of the multinomials and the coefficients that define them, they can be treated as one, when compared to the new approach. As such, these techniques will be referred to as the standard approach.

Probably the biggest difference to the standard approach is that the newly proposed algorithm models a resonator without ports by solving an eigenmode problem. The standard approach models the S-parameter response of a resonator coupled to input and output loads. Since S-parameters are inherently rational functions, they can be modelled very efficiently using multivariate rational metamodelling techniques. However, the main aim of this dissertation is to present a method to predict the different resonance frequencies of the various modes of a resonant structure. Upon finding a model for the S-parameter response, the resonance frequencies are still not easily found.

The following difficulties were identified when modelling the S-parameter response:

i) The arrangement of the coupling lines should be chosen carefully as the feed line arrangement regulates excitation of the various modes. For some arrangements not all of the modes are excited and thus cannot be identified.

ii) When two modes are closely spaced in frequency, the one mode (usually a higher-order mode) may disappear below the skirts of the more strongly coupled mode and once again cannot be identified (see Fig. 4.9).

iii) Mode identification from the S-parameter response requires the finding of resonance peaks (maxima). Finding maxima involves overcoming many more difficulties than finding zeros from the unloaded eigenmode response. For example, when looking for an automated algorithm to find multiple maxima, the effects of noise can easily be misinterpreted and included as invalid resonances.

An advantage of the standard approach is the requirement to set up and explicitly solve only a single system of interpolatory conditions while adding support points completely adaptively along all of the input dimensions (including frequency) simultaneously. This would of course yield an optimal placement of support points with a subsequent minimum number of CEM evaluations. In the new approach, however, this is not possible. As explained in the introduction to this technique, modelling of the $(d+1)$-dimensional input and single output unloaded problem

$$\Re(s, \mathbf{X}) = \det[Z(s, \mathbf{X})], \tag{6.2}$$

requires building a model that is discontinuous across the physical parameter space, due to the scaling factor sf which differs for each set of parameter values. This scaling factor was designed specific for application with the MoM technique, and poses no additional numerical difficulties in one dimension. However, when changing one of the physical parameters, the geometry needs to be remeshed. Since the scaling factor depends on the mesh size, a new discretisation requires recalculation of a different scaling factor and hence leads to a discontinuous function across the physical dimensions. Fig. 6.1 illustrates this discontinuity by varying the normalised ring width w/R.

Note that all the one-dimensional interpolants are continuous across frequency but also, and more importantly, regardless of the complete function showing a discontinuity across w/R, the

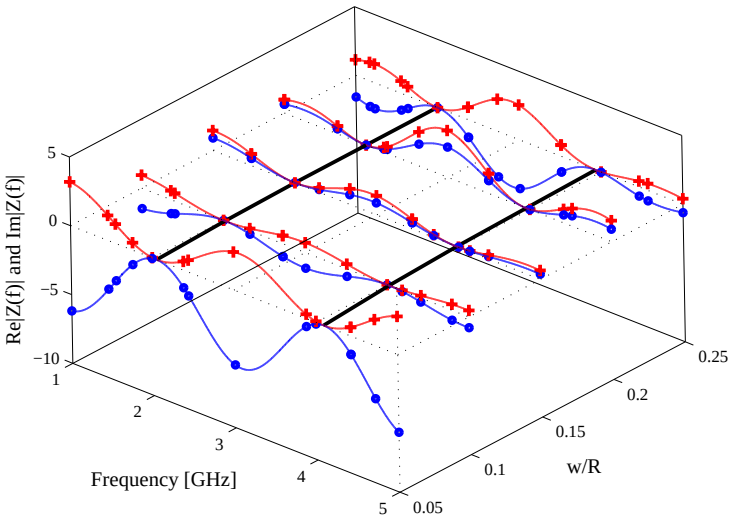

Fig. 6.1. Discontinuous two-dimensional model showing the real (red) and imaginary (blue) parts of the scaled interpolants for different values of normalised ring width w/R. Note that the resonance frequencies (zeros of the function) remain continuous across w/R.

resonance frequencies (zeros of the function) remain continuous across the physical parameter space. Therefore, a discontinuity in the output space lead to the suggested solution of separating frequency from the physical dimensions. This requires execution of two adaptive sampling loops, the first of which is a single input, single output frequency sampling loop that models

$$\Re(s) = \det[Z(s)] \tag{6.3}$$

at a specific geometrical input $\mathbf{X}$. From this single output the zeros $s_0 = \sigma_0 + j2\pi f_0$ are identified and the resonance frequencies f_0 become the output parameters for the second adaptive sampling loop. Thus, instead of constructing a model for the complete characteristic equation (Eq. 6.2) in the second adaptive sampling loop, the resonance frequencies are now modelled as a function of the d-dimensional physical input space $\mathbf{X}$, with the mode number n describing azimuthal variation and m describing radial variation. Thus, with multiple outputs

$$\Re(\mathbf{X}, n, m) = f_0(\mathbf{X}, n, m). \tag{6.4}$$

This second sampling loop is completely adaptive with an optimal placement of the support points similar to the standard approaches. Figs. 6.2 and 6.3 describe the complete algorithm, separating the adaptive rational frequency sampling loop from the adaptive multinomial geometrical sampling loop. Specifics regarding this algorithm are discussed throughout the chapter.

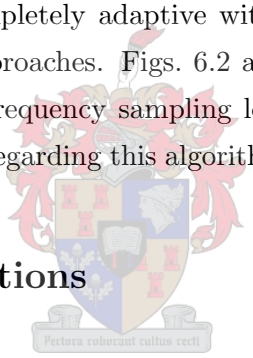

6.2 Metamodel Definitions

Vector Fitting and Zero Calculation

Since the Vector Fitting algorithm was discussed in detail under one-dimensional adaptive rational interpolation methods (Section 3.2), only a few important equations will be repeated here for convenience.

Vector Fitting models the frequency domain behaviour of linear time-invariant (LTI) systems using a rational pole-residue model

$$\Re(s) = \sum_{p=1}^{N_p} \frac{c_p}{s - a_p} + d, \tag{6.5}$$

which equivalently, can also be written in the form

$$\mathbf{R}(s) = \mathbf{C}(s\mathbf{I} - \mathbf{A})^{-1}\mathbf{B} + \mathbf{D}. \tag{6.6}$$

$\mathbf{R}(s)$ is the transfer response matrix, and $\mathbf{A}$, $\mathbf{B}$, $\mathbf{C}$ and $\mathbf{D}$ are the state space matrices for a low-order state equation approximation. Matrix $\mathbf{A}$ is a diagonal matrix containing the final poles a_p and $\mathbf{C}$ is a row vector containing the residues c_p, $\forall p = 1, ..., N_p$. $\mathbf{B}$ is a column vector

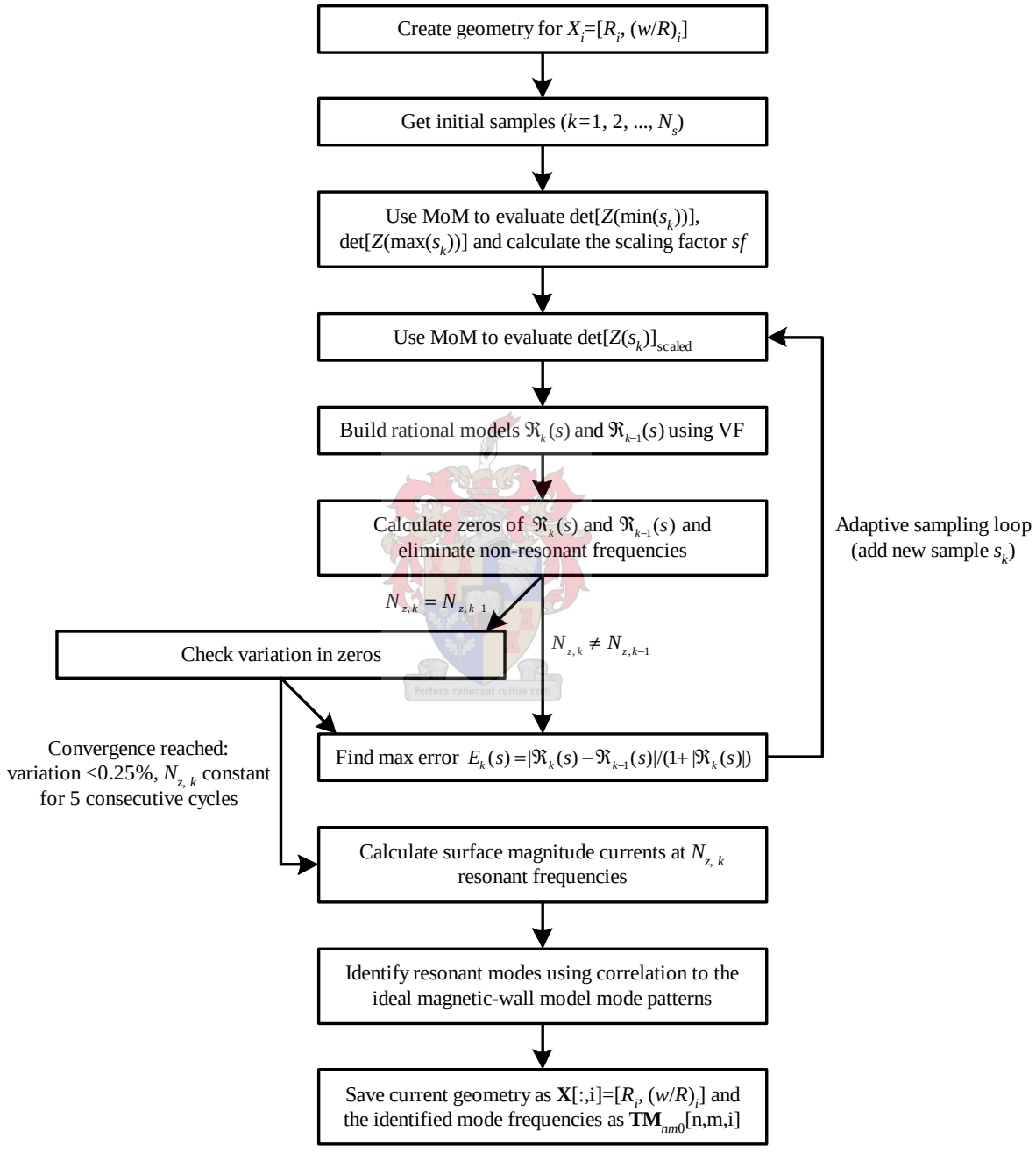

Fig. 6.2. Flowchart of the adaptive rational frequency sampling and mode identification algorithm.

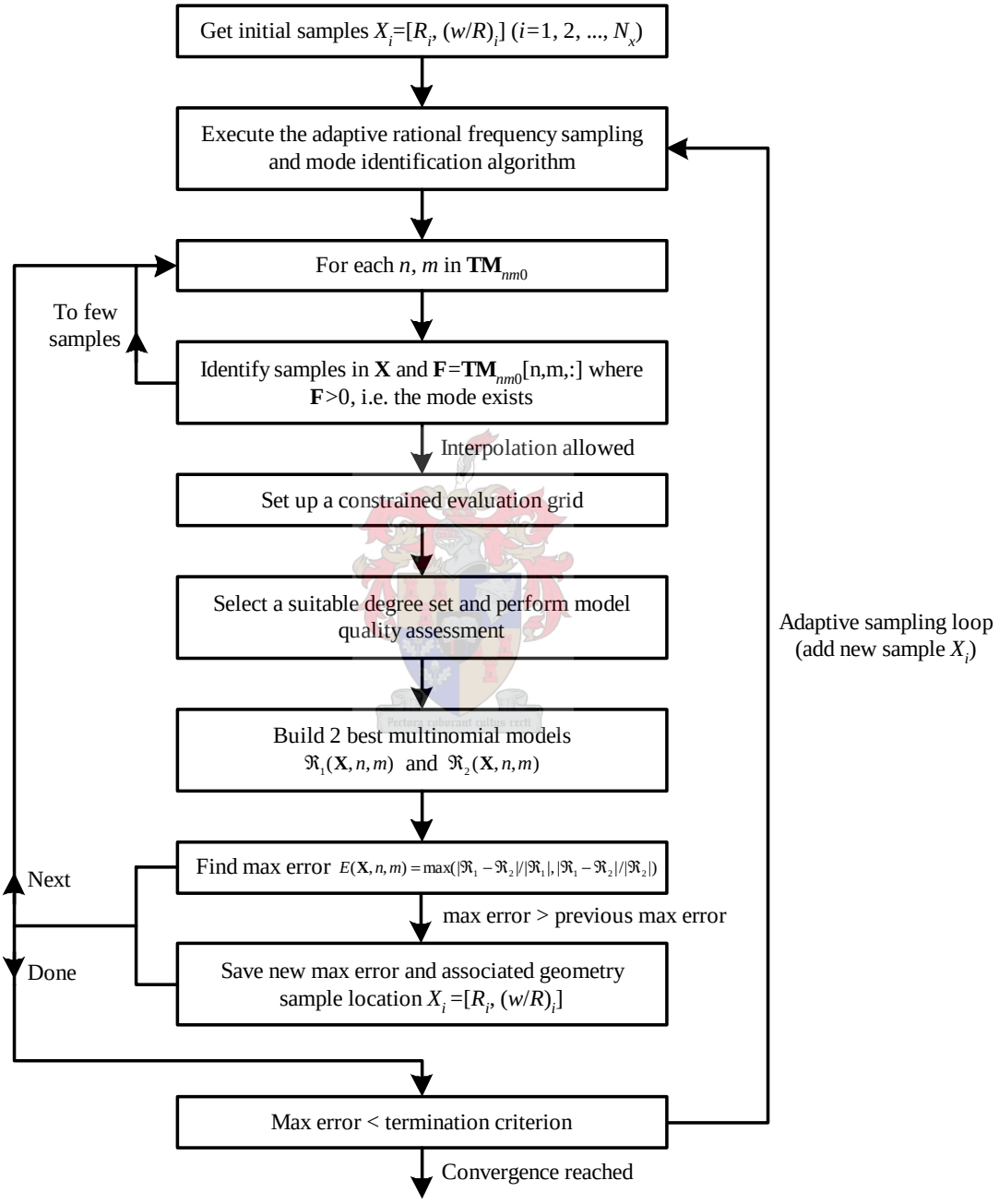

Fig. 6.3. Flowchart of the adaptive multinomial geometrical sampling algorithm.

of ones and $\mathbf{D}$ is the real constant d. Note that $\Re(s_k)$ approximates the measured/simulated data samples $H(s_k)$ at the discrete complex frequencies s_k, $\forall k = 1, \cdots, N_s$.

Finding the zeros of the VF model $\Re(s)$ involves a simple eigenvalue computation of a combination of the state space matrices. It was shown in Section 4.1.2 [27] that, by returning to the time domain state equations of Eq. 6.6 and setting the output equal to zero, the roots are found by solving

$$\text{eig}[\mathbf{A} - \mathbf{B}\mathbf{D}^{-1}\mathbf{C}]. \tag{6.7}$$

Note that in the case of complex pole pairs, a similarity transform applied to each of the submatrices in Eq. 6.7 will ensure that the eigenvalues come out as perfect complex conjugate pairs [20].

Multivariate Multinomial Method

Given multiple non-coinciding sample locations $\mathbf{X}_i \in \mathbb{R}^d$ (input) and corresponding function values f_i (output), a function $\Re : \mathbb{R}^d \to \mathbb{R}$ is constructed, which approximates the values f_i at $\mathbf{X}_i$ using multi-dimensional polynomials (multinomials[§]) of the form

$$\Re(\mathbf{X}) = \sum_{j \in \mathcal{I}} a_j \mathbf{X}^j. \tag{6.8}$$

Here, $j \subset \mathbb{N}^d$, $\mathcal{I}$ is the degree set (Section 6.6 elaborates on the selection of suitable $\mathcal{I}$ sets) and $\mathbf{X}^j$ is a shorthand notation for $x_1^{j_1} \cdots x_d^{j_d}$. Note that, for the particular application of approximating the resonant mode frequencies, the basis functions only depend on the coordinates $\mathbf{X} = [x_1, x_2, \cdots, x_d]$ with d the number of geometrical parameters.

In order to solve for the coefficients a_j in Eq. 6.8, a multinomial with degrees $\mathcal{I}$ that approximates the values f_i at the set of data points $\mathbf{X}_i$ ($i = 1, 2, \cdots, N_x$) in a least-squares sense must be found. This requires solving a homegeneous system of N_x linear equations in N unknown coefficients (the multi-indices in $\mathcal{I}$ can be given a fixed order $j_1, j_2, \cdots, j_N$), each equation of the form

$$\begin{bmatrix} X_i^{j_1} & X_i^{j_2} & \cdots & X_i^{j_N} \end{bmatrix} \begin{bmatrix} a_{j_1} & a_{j_2} & \cdots & a_{j_N} \end{bmatrix}^T = f_i. \tag{6.9}$$

In the case $N_x = N$, the system is square and can be inverted; otherwise, the system is overdetermined and a least-squares technique should be utilised.

When there is just one geometrical parameter ($d = 1$), the multinomial reduces to a simple polynomial and the model is expanded by increasing the degree of the polynomial. The data points $\mathbf{X}_i$ consist of an initial data point distribution plus a number of additional data points selected by an adaptive data point selection algorithm. In this technique, discussed in Section 6.6, two interpolants of different order are constructed and compared (one for each resonant mode).

[§]Multinomials are linear combinations of monomials involving the product of all variables raised to different powers.

A point of largest mismatch for each of these modes are then identified and a new sample is added at the point of greatest error.

As a final note it should be mentioned that the modelling error of any model depends on the ability of the basis functions to represent the data. For highly non-linear data or when there are discontinuities in the data, multinomials have difficulty in modelling the data accurately without resorting to multinomials of very high degree (or using rational models instead), and the algorithm can fail to converge. Furthermore, numerical problems may occur when the degree of the multinomials becomes too high. It is therefore advantageous to limit the degree of the multinomials, or to perform a model quality assessment before selecting the final model order (Section 6.6).

6.3 Prediction of Resonance Frequencies using Error Estimation and Adaptive Vector Fitting

In general, a rational interpolant $\Re(s)$ can be found that accurately models a microwave structure over the interval $[s_0, s_1]$, provided that enough support points are used. However, to reduce the computational expense, adaptive sampling algorithms have been introduced offering an efficient method to establish accurate rational metamodels by automatically placing support points at their optimal position, and thereby minimising computational effort. Previously in [13, 15], Lehmensiek proposed an efficient adaptive frequency sampling algorithm for model-based parameter estimation based on a Thiele-type continued fraction rational interpolation formulation[†]. Convergence of this algorithm is reached when two consecutive models agree within a specified accuracy.

In this section, the adaptive sampling algorithm is extended to ensure a faster convergence based on the position of the actual roots or resonance frequencies of $\Re(s)$. This technique is particularly useful when applied to the problem of accurately finding the resonance frequencies of a structure.

The process of selecting data points and building models in an adaptive way is often called *reflective exploration*. Following the formulation presented in [13, 15], the reflective function used is

$$E_k(s) = \frac{|\Re_k(s) - \Re_{k-1}(s)|}{1 + |\Re_k(s)|}, \tag{6.10}$$

which provides an estimate of the maximum interpolation error over the interval of interest. The residual term $E_k(s)$ in Eq. 6.10 shows the relative error between the current and previous estimates of the interpolant. The standard procedure by which the adaptive sampling algorithm works is as follows—As a first step, an initial number of support points are chosen. Then, by

[†]This technique was also utilised in Chapters 4 and 5.

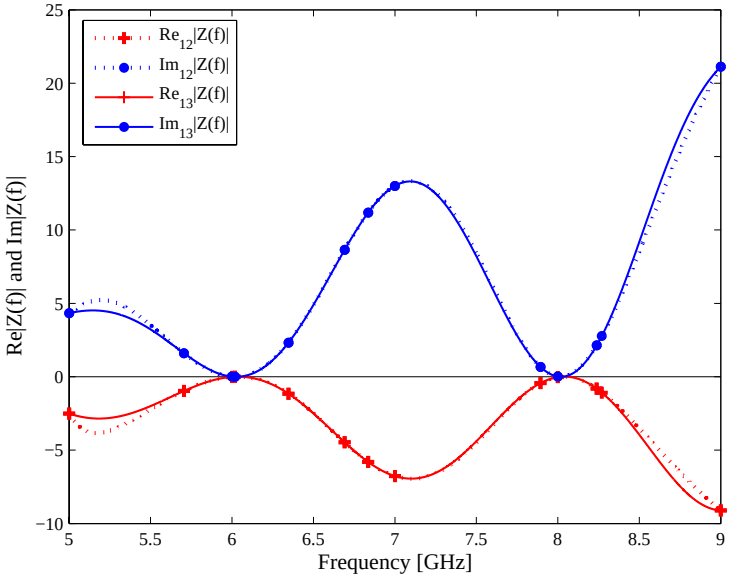

Fig. 6.4. Large discrepancies between the final interpolant estimates may still exist even if the resonance frequencies have converged.

using the VF formulation, the residual $E_k(s)$ is evaluated at a large number of equi-spaced sample points over the interval. A new data point (s_{k+1}, H_{k+1}) is selected near the maximum of the reflective function and the procedure is repeated until the estimated error has been reduced to a sufficiently low value (e.g. -80 dB).

Instead of this approach, a new convergence criterion is introduced, which compares the relative position of the roots of the current and previous estimates $\Re_k(s)$ and $\Re_{k-1}(s)$. After each iteration, Eq. 6.7 is solved and the actual roots (resonant frequencies) of Eq. 6.1 are identified[‡]. When both estimates $\Re_k(s)$ and $\Re_{k-1}(s)$ predict the same number of roots $N_{z,k} = N_{z,k-1}$, the relative movement of each root is compared to its previous prediction. When all the roots have converged to within a sufficiently small variation (e.g. 0.25%), the interpolant is said to have converged.

In some instances there may still be large differences between the final two interpolant estimates, i.e. $\Re_k(s)$ may not be an entirely accurate model. However, since only predictions of the resonance frequencies are required, which are indeed accurate, a more accurate interpolant model is not needed. Fig. 6.4 shows a typical difference between two consecutive models. Note that the interpolants agree closely in the regions of resonance and were found to have converged successfully.

For automatic termination of the algorithm over a certain frequency range, it is required that the same number of roots are predicted for 5 consecutive cycles, and that all of these roots have satisfied the convergence criterion throughout these cycles. The observation was made that the

[‡]For details on the identification process used to extract the resonance frequencies from all found roots, refer to Section 4.1.3, [27].

TABLE 6.1
Number of samples needed to reach a specified convergence criterion together with the number of roots identified. The Convergence % is the relative amount by which roots in two consecutive models may vary.

(a) Ring parameters: $R = 16.9$ mm, $w/R = 0.1$; $f = [1\text{ GHz}, 5\text{ GHz}]$.

Known Number of Roots: 4		
Convergence %	**Number of Samples**	**Number of Roots Found**
5.0	6	2
1.0	9	3
0.5	10	3
0.25	14	4
0.1	14	4

(b) Ring parameters: $R = 16.9$ mm, $w/R = 0.1$; $f = [5\text{ GHz}, 9\text{ GHz}]$.

Known Number of Roots: 4		
Convergence %	**Number of Samples**	**Number of Roots Found**
5.0	7	2
1.0	7	2
0.5	7	2
0.25	13	4
0.1	14	4

(c) Ring parameters: $R = 16.9$ mm, $w/R = 0.6$; $f = [1.5\text{ GHz}, 4.5\text{ GHz}]$.

Known Number of Roots: 4		
Convergence %	**Number of Samples**	**Number of Roots Found**
5.0	7	1
1.0	16	4
0.5	16	4
0.25	16	4
0.1	16	4

zeros converge to accuracies far better than the required 0.25% variation while cycling through the 5 stable intervals. An advantage to this technique is that it is fully automated and the user does not need to know the number of resonance frequencies in advance. A disadvatage is that the algorithm requires evaluation of at least 4 more 'unnecessary' EM analyses than are actually needed.

The algorithm was verified by setting up a two-dimensional test problem consisting of an unloaded lossy microstrip ring resonator with mean ring radius $R = 16.9$ mm and different normalised ring widths (w/R). The substrate has a relative permittivity of $\epsilon_r = 2.2$, a dissipation factor of $\tan(\delta) = 0.0009$ and thickness $h = 0.508$ mm. Table 6.1 shows the number of samples required to reach a desired accuracy of the roots. When the convergence criterion is too relaxed ($> 0.25\%$), the interpolant model may still be too inaccurate to successfully find all the roots. Fig. 6.5 shows this phenomenon by plotting the interpolants $\Re_6(f)$, $\Re_9(f)$, $\Re_{10}(f)$ and $\Re_{14}(f)$ after reaching root convergences of 5.0%, 1.0%, 0.5% and 0.25% respectively. These interpolants correspond to the results presented in Table 6.1(a) and clearly highlight, when looking at $\Re_{14}(f)$, why fewer than the known number of roots were correctly identified using less than 14 samples.

Table 6.2 lists the reduction in the number of sample points required when using a 0.25% root convergence criterion compared to the Lehmensiek error approach with $E_k(s) < -80$ dB, which

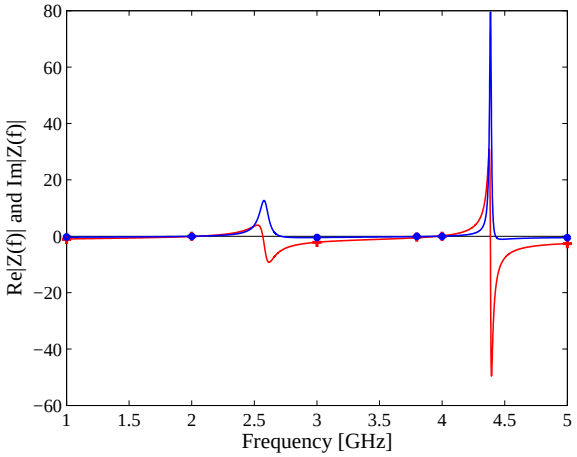

(a) $\Re_6(f)$: 5.0% convergence in roots.

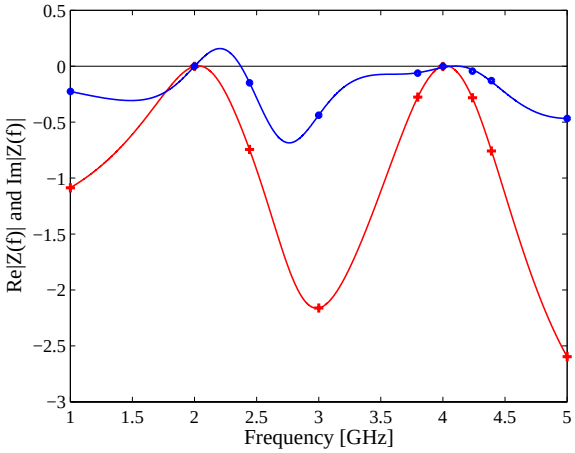

(b) $\Re_9(f)$: 1.0% convergence in roots.

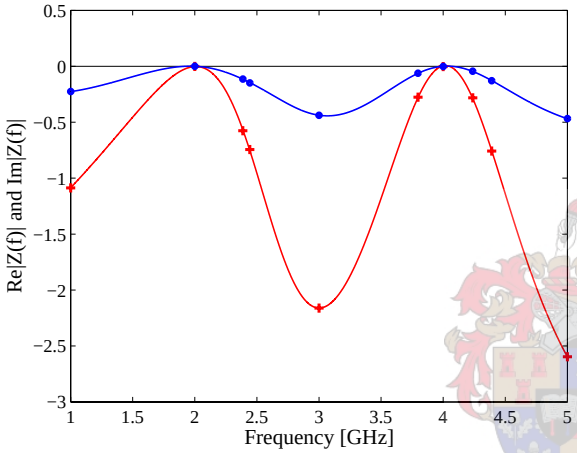

(c) $\Re_{10}(f)$: 0.5% convergence in roots.

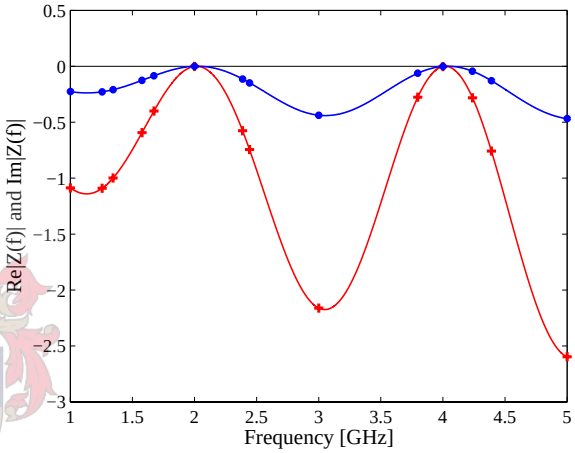

(d) $\Re_{14}(f)$: 0.25% convergence in roots.

Fig. 6.5. Real (red) and imaginary (blue) parts of the scaled interpolants after reaching different convergence criteria.

is needed for the same accuracy of resonance frequencies. Reductions of greater than 25% in the number of selection points were achieved, relating directly to a substantial save in computational effort.

6.4 Mode Identification

In this section a method is introduced by which each of the resonant frequencies identified during the adaptive frequency sampling loop, can be associated with a known resonant mode. While human perception has no difficulty in identifying modal field distributions, automated mode identification is no trivial task. Since the multi-dimensional geometrical interpolation loop needs to 'know' which resonant frequency belongs to which resonant mode (output) before a model can be built, this algorithm is of the utmost importance.

The proposed solution is based on the ideal mode patterns of simplified resonator structures.

TABLE 6.2
REDUCTION IN THE NUMBER OF SAMPLE POINTS REQUIRED WHEN USING THE 0.25% ROOT CONVERGENCE CRITERION AND THE $E_k(s) < -80$ dB LEHMENSIEK [13] APPROACH.

w/R	Frequency [GHz]	Number of Roots	0.25% Convergence Number of Samples	$E_k(s) < -80$ dB Number of Samples	% Decrease in Samples
0.1	1.0–5.0	4	14	21	33.3
0.1	5.0–9.0	4	13	18	27.8
0.6	1.5–4.5	4	16	24	33.3
0.05	1.5–10.5	10	26	43	39.5
0.6	1.5–10.5	23	76	109	30.3

Thus, as an alternative to the human eye, one may use digital signal principles like cross-correlation and a form of variance to establish which one of the ideal (known) mode patterns agrees most with the unknown current pattern. This method is of course only useful when an analytic field analysis solution for the resonant structure exists. One of these analytic models is the magnetic-wall model [56], which is used to model microstrip ring resonators. When recalling that the solution to the fields of this model must satisfy Maxwell's equations in cylindrical coordinates and that by setting the tangential H-fields equal to zero at the inner and outer radii of the ring, it follows that

$$\begin{aligned} H_R &= A\frac{jn}{\omega\mu_0 R}\big(J_n(kR) - \frac{J_n'(kR_o)}{N_n'(kR_o)}N_n(kR)\big)\big(\cos(n\phi) - \sin(n\phi)\big) \\ H_\phi &= A\frac{k}{j\omega\mu_0}\big(J_n(kR) - \frac{J_n'(kR_o)}{N_n'(kR_o)}N_n(kR)\big)\big(\sin(n\phi) + \cos(n\phi)\big), \end{aligned} \tag{6.11}$$

where H_R and H_ϕ are the radial and azimuthal magnetic field components respectively. A is an arbitrary constant, k is the wave number, J_n is a Bessel function of the first kind of order n and N_n is a Bessel function of the second kind and order n. J_n' and N_n' are the derivatives of the Bessel functions with respect to the argument kR. Note that both orthogonal solution sets are included in Eq. 6.11. Also, since the surface current $\mathbf{J}$ is a function of the magnetic fields only

$$\mathbf{J} = \hat{\mathbf{n}} \times \mathbf{H}, \tag{6.12}$$

the electric fields are not shown here. Of even greater importance is that this model is only used to establish the ideal mode patterns for the same geometry resonator as is used in the CEM design. It is not important at what frequencies these patterns were computed, or which substrate was being used, i.e. one may revert to using the simplest free-space solution without worrying about using incorrect effective permittivity and effective width values in the magnetic-wall model.

The correlation coefficient $\rho_{XY}[i]$ is a normalised measure of the strength of the linear relationship between two variables X and Y according to the relation [94]

$$\begin{aligned} r_{XY}[i] &= \sum_{n=-\infty}^{n=\infty} X[n]Y[n-i] \\ \rho_{XY}[i] &= \frac{r_{XY}[i]}{\sqrt{r_{XX}[0]r_{YY}[0]}} \qquad\qquad i = [-\infty, \infty]. \end{aligned} \tag{6.13}$$

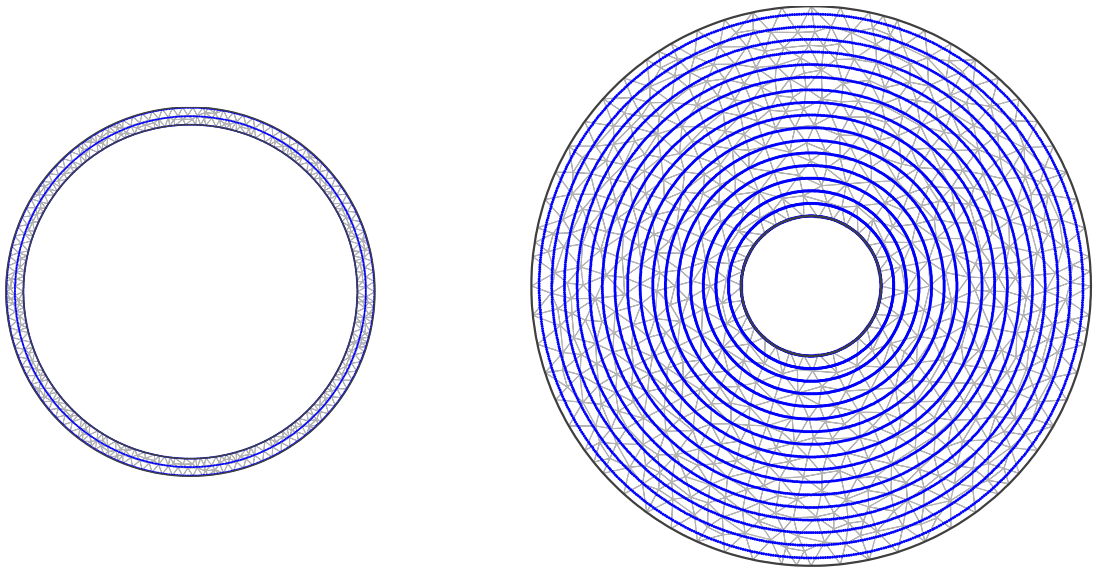

(a) $w/R = 0.05$. (b) $w/R = 0.6$.

Fig. 6.6. Circles along which the current magnitude is computed and correlated to the ideal model.

Here $r_{XY}[i]$ is a second-order moment called cross-correlation, while $r_{XX}[0]$ and $r_{YY}[0]$ are the auto-correlation values for the respective variables X and Y. Uncorrelated data results in a correlation coefficient of 0, while equivalent data sets have a correlation coefficient of 1.

In Fig. 6.6 a number of circular paths are shown atop two different rings of the same mean radius ($R = 16.9$ mm), but with different normalised ring widths of $w/R = 0.05$ and $w/R = 0.6$, respectively. These circles represent points at which the current magnitude will be evaluated. Since rings of large w/R also support higher-order modes, a larger number of evaluation points (more circles) will be used for larger normalised ring widths, according to the equation

$$N_{\text{circles}} = \left\lfloor 25\frac{w}{R} \right\rfloor + 2. \tag{6.14}$$

This distribution of circles may be varied to suit specific needs. Current magnitudes calculated along these circles are appended to form a single current variable, which is then correlated to the analytic current values computed at the same location of points along the surface of the ideal model.

The correlation coefficients graphs shown in Fig. 6.7 were obtained by cross-correlating the current patterns of two of the identified resonance frequencies to various ideal mode patterns as generated by Eq. 6.11. A cross-correlation of 99.79% identified the mode pattern in Fig. 6.7(a) as the TM_{020} mode, while a 99.26% cross-correlation identified the mode pattern in Fig. 6.7(b) as the TM_{510} mode. These are indeed very good correlations. Interesting to note from Fig. 6.7 is that the correlation coefficient graph offering the best cross-correlation, has distinct differences from the other correlation coefficient graphs. These differences are discussed below.

Firstly, when the identified mode has a variation in the ϕ-direction, i.e. $n > 0$ in TM_{nm0}, the

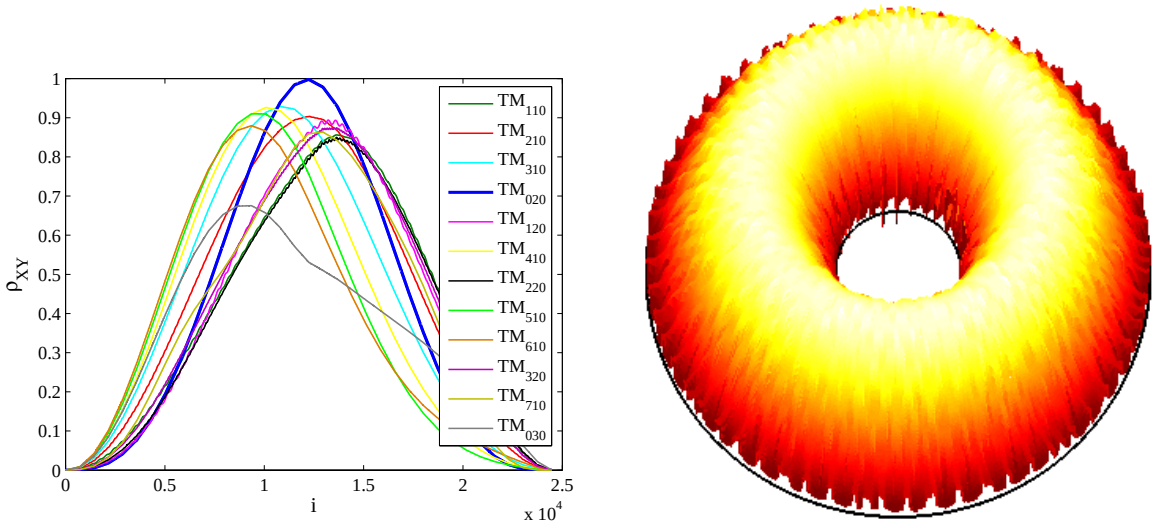

(a) TM_{020} mode identified with a 99.79% correlation.

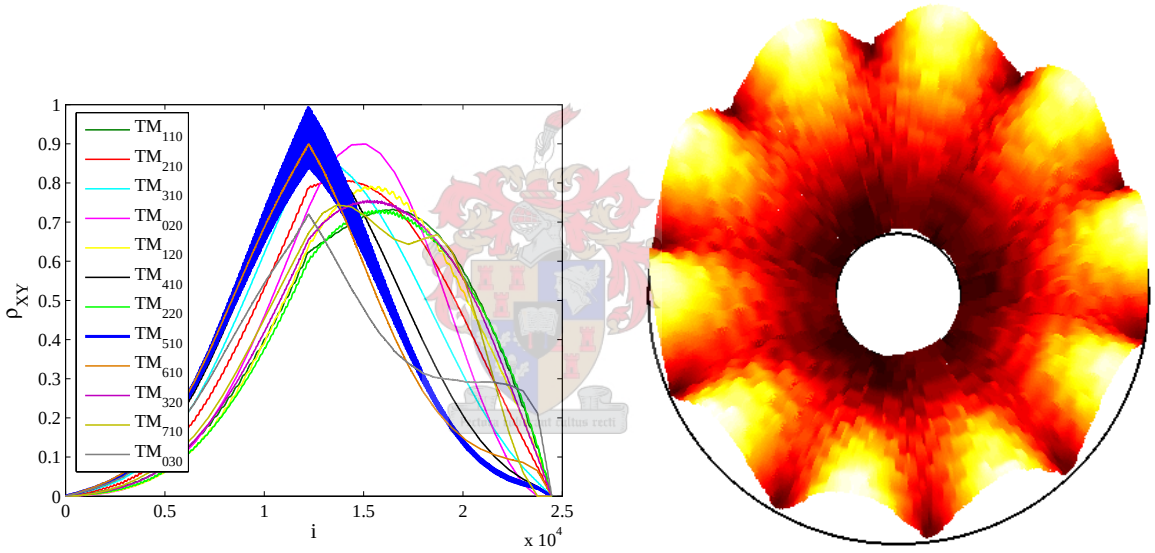

(b) TM_{510} mode identified with a 99.26% correlation.

Fig. 6.7. Correlation coefficient graphs obtained when correlating an unknown mode pattern to a number of possible ideal mode patterns.

correlation coefficient shows a distinct band of variation. This effect is more clearly illustrated in Fig. 6.8 where fewer samples were used, and was found to be typical when correlating two cosine or sine functions of the same period (as was the case for the TM_{510} mode). When $n = 0$ in TM_{nm0}, the variance band phenomenon is absent. This result was expected and may be verified by looking at Eq. 6.11 where the cosine and sine terms either disappear or become constant when $n = 0$.

A second observation is that most of the correlation coefficients graphs tend to become skew relative to their maximum value in ρ_{XY}, except for the best correlation coefficient graph, which shows a symmetrical distribution around its maximum.

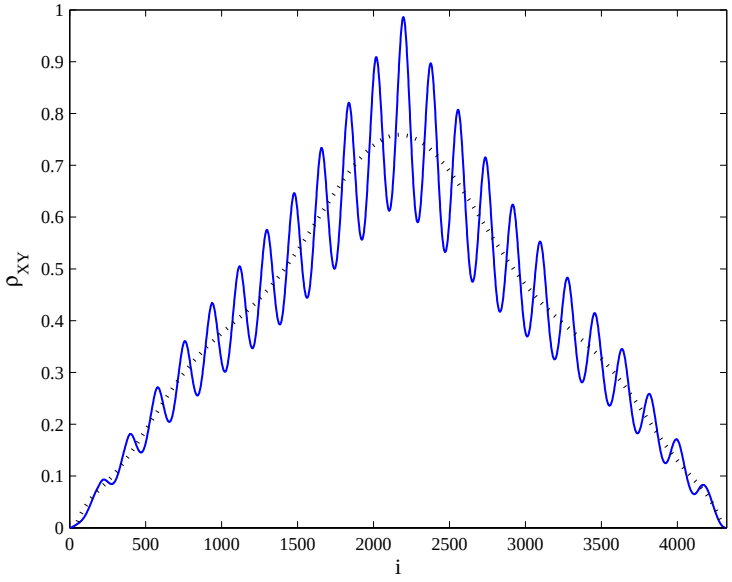

Fig. 6.8. Band of variation found when correlating two cosine or sine functions of the same period. The black dotted line represents a mean vector function, which we call $\bar{\mathbf{X}}$.

These two observations are mostly known as the second and third central moments in random signal theory, the first of which was used to explore and strenghten our mode identification algorithm. The second central moment, or better known as variance [94] for a discrete random variable in signal theory, is given by

$$\sigma_X^2 = E[(\mathbf{X} - E[\mathbf{X}])^2] = \sum_{i=1}^{N} (X[i] - E[\mathbf{X}])^2 P(X[i]), \tag{6.15}$$

where $P(X[i]) = 1/N$ is the probability of the value occurring at $X[i]$ and $E[\mathbf{X}]$ is the expected or mean value of a random variable. For our purposes of calculating the variation band of the correlation coefficient, a mean vector, instead of the mean value around the origin, had to be introduced (shown with a dotted line in Fig. 6.8). This vector can be seen as a function running along the mean of the variation band and will be called $\bar{\mathbf{X}}$. On substituting $\bar{\mathbf{X}}$ for $E[\mathbf{X}]$ into Eq. 6.15 the band of variance can now be calculated. With the exception of the TM_{0m0} modes, where this band of variance is zero, this value serves as an important second 'opinion' to help associate resonant frequencies to their specific modes, especially when the correlation coefficient does not give a convincing percentage correlation.

Tables 6.3 and 6.4 list the identified modes for two ring resonators—the first with radius $R = 16.9$ mm and normalised ring width $w/R = 0.05$, and the second with $R = 18.75$ mm and $w/R = 0.6$ also supporting higher-order modes. The percentage cross-correlation achieved, as well as the band of variance for that mode, is shown together with the second highest percentage cross-correlation and its associated band of variance. These final columns were included to show that the identified modes are clearly recognisable and easily distinguished from the other modes. For most modes, an exceptional correlation is achieved, with the band of variance strengthening the selection. However, the TM_{710} was found to be an exception. Not only is the correlation

TABLE 6.3
IDENTIFICATION OF RESONANT MODES BY MEANS OF CROSS-CORRELATION AND VARIANCE.
(RING PARAMETERS: $R = 16.9$ mm, $w/R = 0.05$)

Resonant Mode	f_0 [GHz]	% Cross-Correlation	Band of Variance	2nd Highest % Cross-Correlation	Band of Variance
TM_{110}	2.0537	92.50	0.0235	83.83	0.0020
TM_{210}	4.0986	98.61	0.0237	83.94	0.0015
TM_{310}	6.1453	96.91	0.0224	81.28	0.0007
TM_{410}	8.1851	99.08	0.0229	84.08	0.0011
TM_{510}	10.2157	99.01	0.0219	81.06	0.0013

(a) TM_{110}: 92.50% correlation. (b) TM_{210}: 98.61% correlation. (c) TM_{310}: 96.91% correlation.

(d) TM_{410}: 99.08% correlation. (e) TM_{510}: 99.01% correlation.

Fig. 6.9. Resonant modes identified using cross-correlation and variance parameters. (Ring parameters: $R = 16.9$ mm, $w/R = 0.05$)

percentage quite low (78.15%), but it is also worse than some of the other mode correlations achieved. Since none of these correlations are very good either (maximum of 89.30%), it was suggested to use the band of variance instead, which indeed identified the correct resonant mode. Figs. 6.9 and 6.10 verify the identified modes by plotting the current magnitude patterns at each of the resonant frequencies.

It was mentioned previously that the proposed technique is limited to the availability of an analytical field analysis model from which the ideal mode patterns can be computed. An example is the square or meander ring resonator. In fact, so far only the annular ring resonator has the field theory derivation for its frequency modes [74]. For square ring resonators, it is difficult

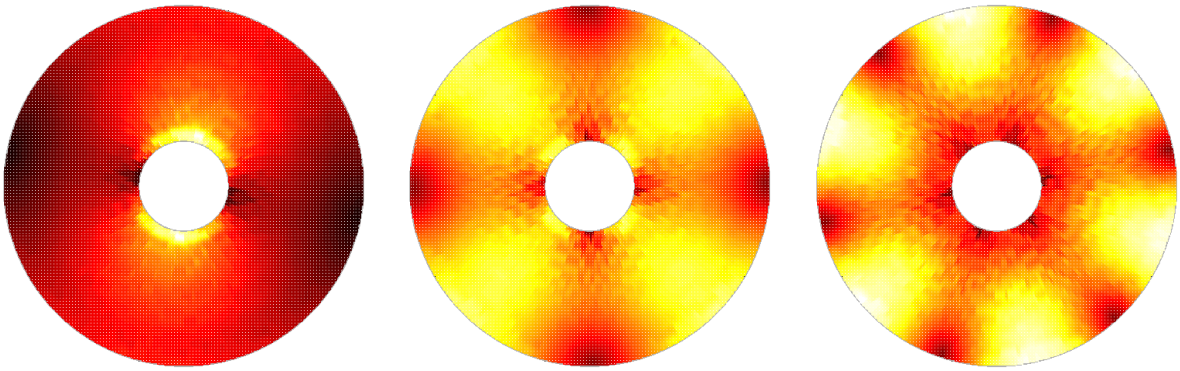

(a) TM_{110}: 99.64% correlation. (b) TM_{210}: 99.74% correlation. (c) TM_{310}: 99.68% correlation.

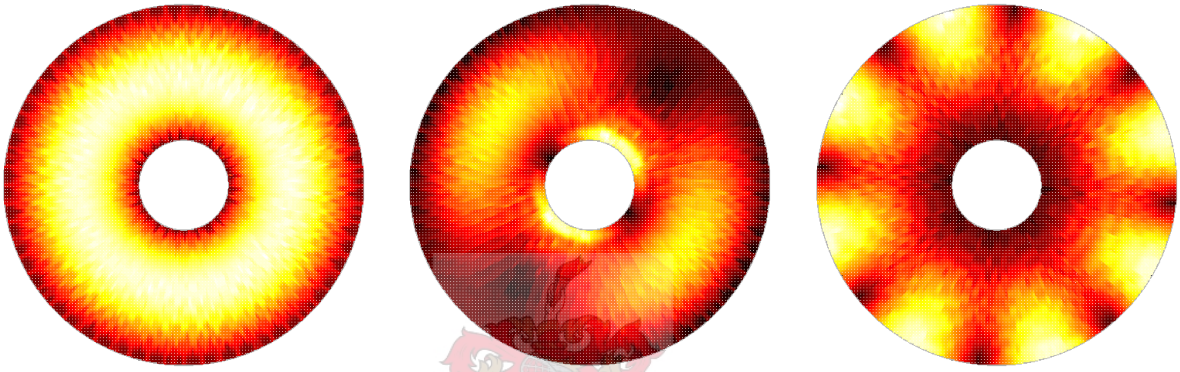

(d) TM_{020}: 99.79% correlation. (e) TM_{120}: 99.33% correlation. (f) TM_{410}: 99.58% correlation.

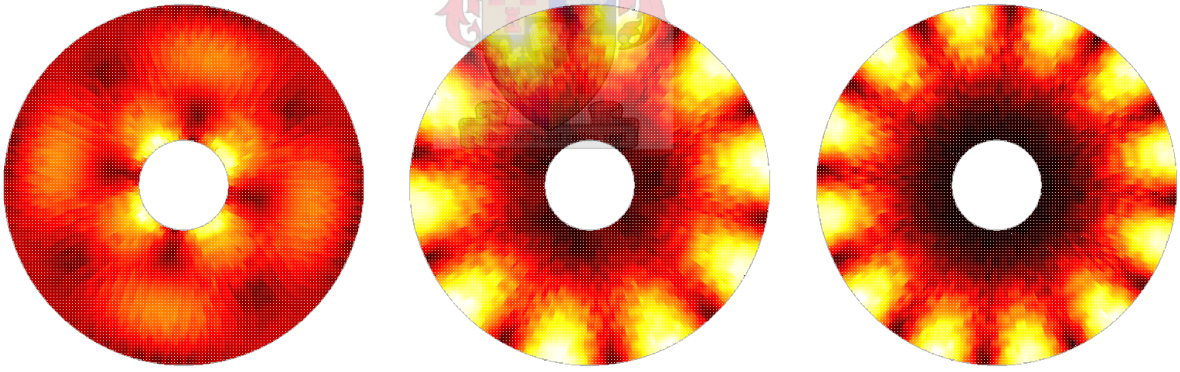

(g) TM_{220}: 99.36% correlation. (h) TM_{510}: 99.26% correlation. (i) TM_{610}: 97.69% correlation.

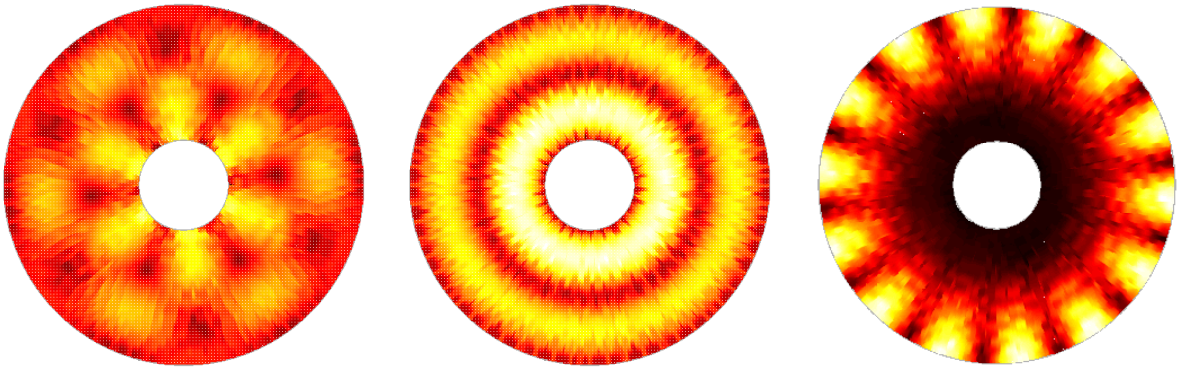

(j) TM_{320}: 99.31% correlation. (k) TM_{030}: 99.23% correlation. (l) TM_{710}: 78.15% correlation.

Fig. 6.10. Resonant modes identified using correlation and variance parameters. (Ring parameters: $R = 18.75$ mm, $w/R = 0.6$)

TABLE 6.4
IDENTIFICATION OF RESONANT MODES BY MEANS OF CROSS-CORRELATION AND VARIANCE.
(RING PARAMETERS: $R = 18.75$ mm, $w/R = 0.6$)

Resonant Mode	f_0 [GHz]	% Cross-Correlation	Band of Variance	2nd Highest % Cross-Correlation	Band of Variance
TM_{110}	1.8426	99.64	0.0071	87.36	0.0001
TM_{210}	3.2716	99.74	0.0023	90.72	0.0000
TM_{310}	4.5317	99.68	0.0019	92.03	0.0000
TM_{020}	4.6994	99.79	0.0000	92.90	0.0000
TM_{120}	5.3940	99.33	0.0052	88.20	0.0001
TM_{410}	5.7557	99.58	0.0021	91.75	0.0000
TM_{220}	6.8973	99.36	0.0058	88.97	0.0015
TM_{510}	6.9662	99.26	0.0023	91.06	0.0001
TM_{610}	8.1529	97.69	0.0025	90.54	0.0002
TM_{320}	8.4844	99.31	0.0038	88.91	0.0000
TM_{030}	9.0018	99.23	0.0000	90.30	0.0004
TM_{710}	9.3979	78.15	0.0016	89.30	0.0000

to use the magnetic-wall model to obtain the frequency modes and field patterns because of their complex boundary conditions. To test the scope of the proposed mode identification technique, the ideal mode patterns of the magnetic-wall model of ring resonators were correlated directly with the unknown current patterns found on a square ring resonator. With the mean circumference of the square ring resonator ($4l$, where l is the mean length of one side) equal to the mean circumference of the annular ring model ($2\pi R$) and the normalised ring widths approximately equal (i.e. $w_s/(0.5l) \approx w/R$, where w_s is half the square ring width), the cross-correlation and band of variance parameters can be calculated as before.

Table 6.5 shows the results for the first four identified modes. The square ring resonator has a mean side length of $l = 26.52$ mm and a normalised width of $w_s/(0.5l) = 0.05$. The substrate parameters were relative permittivity $\epsilon_r = 2.2$, dissipation factor $\tan(\delta) = 0.0009$ and thickness $h = 0.508$ mm. The ring was designed for a fundamental resonant frequency at 2.0 GHz. The percentage cross-correlation achieved as well as the band of variance for that mode is shown together with the second highest percentage cross-correlation and its associated band of variance. Notice that even though the correlation percentages have slightly decreased compared to those in Table 6.3 for an annular ring of similar normalised ring width, the modes are still clearly identifiable. Once again, the effect of a band of variance for the TM_{nm0} modes with $n > 0$ is visible and should be taken into consideration when the correlation percentages become less

TABLE 6.5
IDENTIFICATION OF THE RESONANT MODES OF A SQUARE RING RESONATOR BY MEANS OF CROSS-CORRELATION AND VARIANCE.
(SQUARE PARAMETERS: $l = 26.52$ mm, $w_s/(0.5l) = 0.05$)

Resonant Mode	f_0 [GHz]	% Cross-Correlation	Band of Variance	2nd Highest % Cross-Correlation	Band of Variance
TM_{110}	2.0988	93.22	0.0241	83.11	0.0012
TM_{210}	4.2371	96.75	0.0111	85.89	0.0018
TM_{310}	6.2768	96.25	0.0187	83.22	0.0002
TM_{410}	8.4611	92.29	0.0115	88.70	0.0036

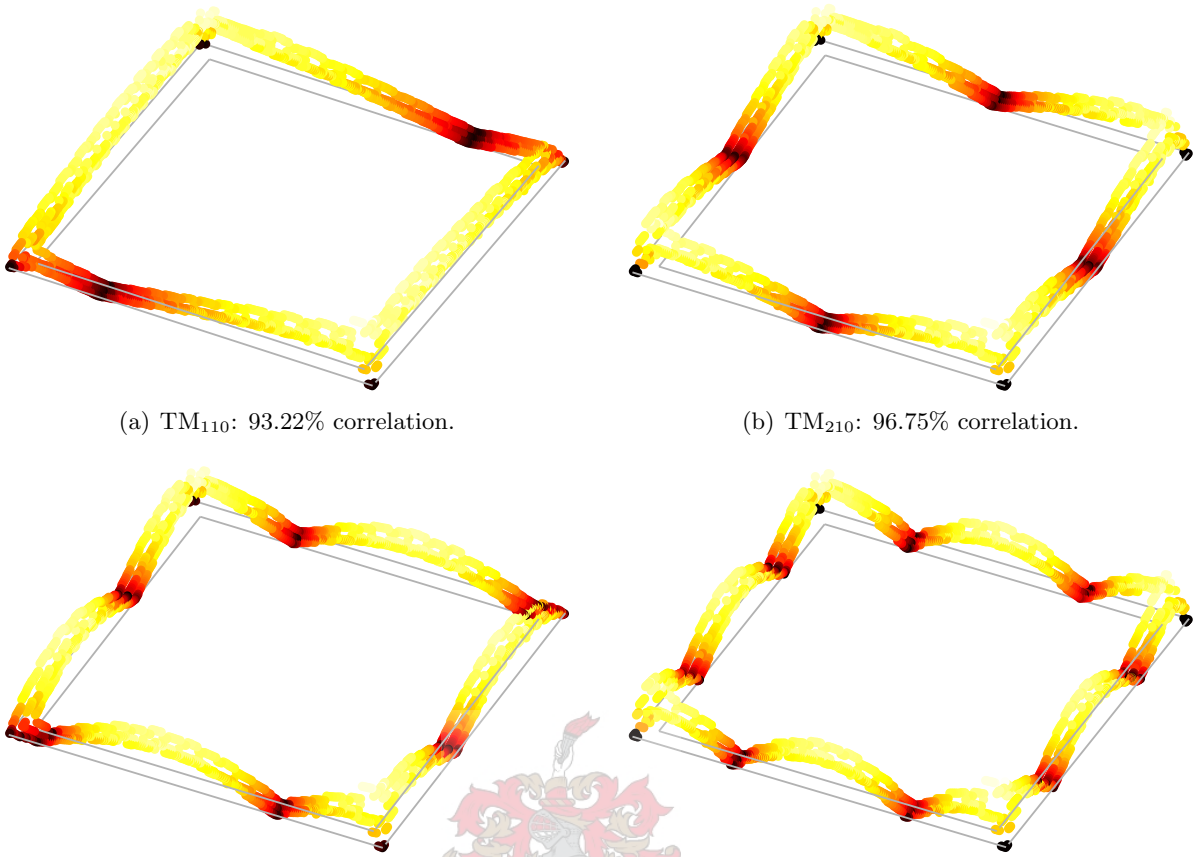

(a) TM_{110}: 93.22% correlation.

(b) TM_{210}: 96.75% correlation.

(c) TM_{310}: 96.25% correlation.

(d) TM_{410}: 92.29% correlation.

Fig. 6.11. Resonant modes of a square ring resonator identified using correlation and variance parameters. (Square parameters: $l = 26.52$ mm, $w_s/(0.5l) = 0.05$)

convincing. Fig. 6.11 verifies the identified modes by plotting the current magnitude patterns at each of the resonant frequencies.

6.5 Constrained Grid Modelling

When building a metamodel, it is important to realise that the interpolation/approximation model is valid only within the constraints of the parameter space. For example, when modelling the resonant frequency behaviour of the various modes of a microwave ring resonator, it may happen that as the geometrical parameters take on smaller dimensions, one or more of the mode responses may exist partly outside of the defined frequency interval. Similarly, higher-order modes TM_{nm0} with $m > 1$ do not exist for a design criterion of normalised ring width $w/R < 0.2$. As a result, to avoid the algorithm from ending up in an infinite loop by not being able to model a specific mode at a specific geometrical parameter, the various models should only be evaluated at a constrained number of grid points within the parameters space. The purpose of this section is to find such a constrained grid for one and two physical dimensions.

A model can be constructed in one dimension when three or more support points are present.

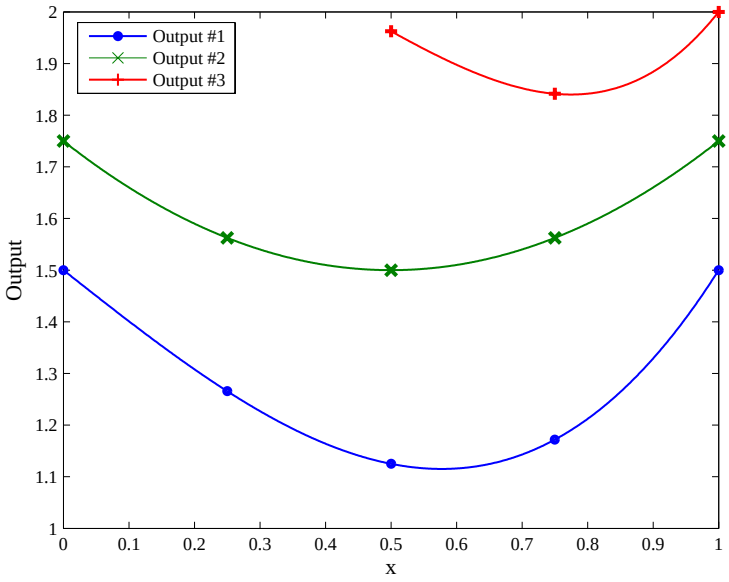

Fig. 6.12. Theoretical example illustrating constrained grid evaluation in one dimension.

Setting up evaluation points in this dimension poses no specific difficulty, as the grid points ($N_w = 300$) are simply spread equally between the minimum and maximum support points for which the specific output has been identified. This is illustrated in Fig. 6.12, where three theoretical output parameters are being modelled. From the figure it is evident that the first two outputs should be evaluated across the entire interval $x = [0, 1]$, while the third output can only be evaluated properly over the interval $x = [0.5, 1]$, even though this parameter may possibly also exist within the interval $x = [0.45, 0.5]$.

In two dimensions, a model can be constructed when the support points cover a non-zero area. Setting up a constrained evaluation grid in two dimensions is, however, not as simple as in the one-dimensional case. For each of the output parameters, the support points need to be classified into points either belonging to the output or points already explored, the latter being support points at which the output does not exist or falls outside of the parameter space. This information is then utilised to construct a type of convex hull around the support points belonging to the output. This will be illustrated more clearly by an example.

In Fig. 6.13(a) a number of support samples are shown, where the circles belong to Output #1 and the plus signs belong to Output #2. Since the circles include the entire parameter space $x_1 = [0, 1]$ and $x_2 = [0, 1]$, no constrained grid needs to be set up and the evaluation points are spread evenly on a 30×30 grid. The situation for Output #2 is very different and the algorithm used to construct the constrained grid of points may be described by the following steps:

i) Identify all support points that define the output (blue plus signs) and connect these points in order around their geometrical mean (red dot) by increasing angle (Fig. 6.13(b)). All remaining support points are marked as points already explored (green circles).

ii) Compute the convex hull around these samples by identifying and removing all interior

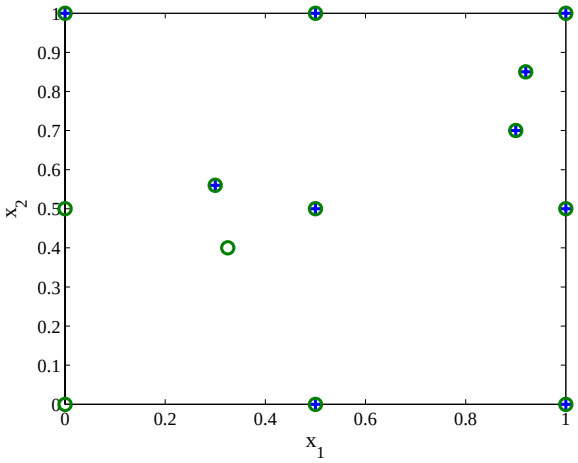

(a) Support samples for a 2D problem with two outputs being modelled.

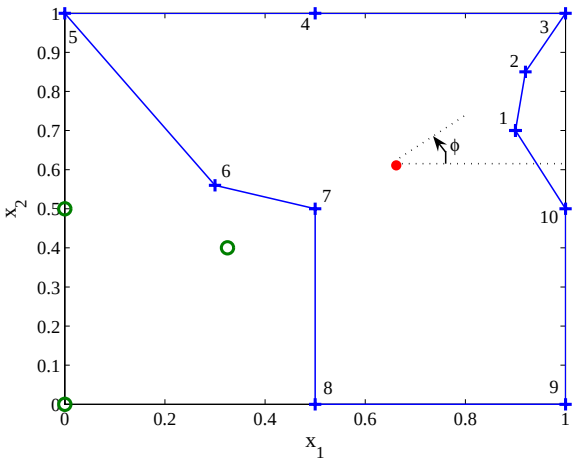

(b) Support samples ordered by increasing angle.

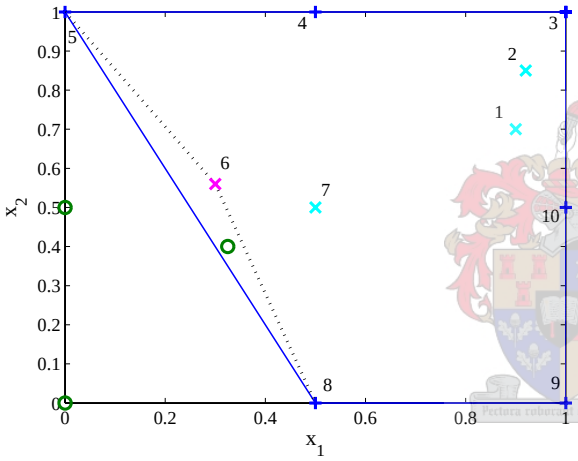

(c) Convex hull around support samples with the interior samples marked.

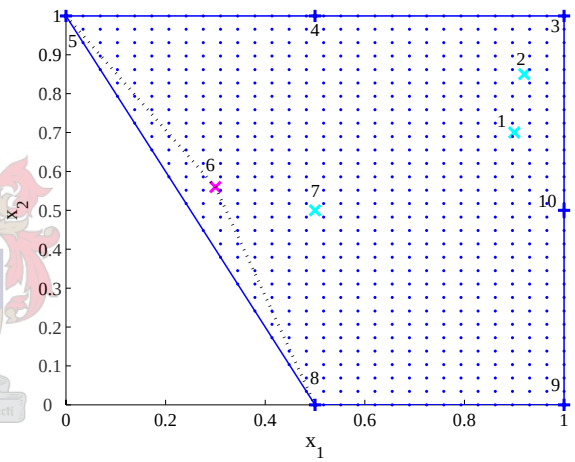

(d) Evaluation grid constrained to convex hull.

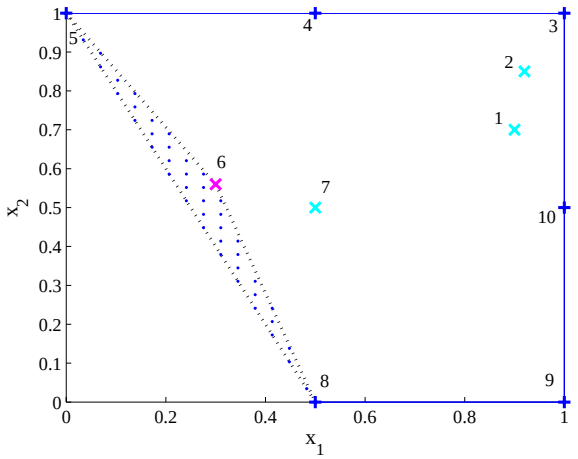

(e) Evaluation samples in previously explored regions should be subtracted from constrained grid.

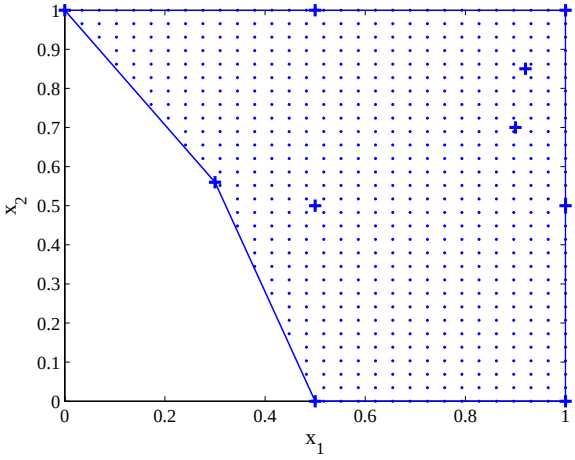

(f) Constrained grid for model evaluation.

Fig. 6.13. Two-dimensional constrained evaluation grid setup as illustrated at different stages of the algorithm.

sample points. Interior samples are those support points having an outer angle of less than 180° with respect to its neighbouring points. The angle is computed by walking in a counterclockwise direction around the support samples. This procedure of removing interior samples should be repeated until no further interior points are left (Fig. 6.13(c)). During this identification step, the interior samples are sorted into two groups. The first group (magenta crosses) forms part of a convex hull that includes previously explored samples, while the second group (cyan crosses) forms part of a convex hull that has not yet been explored. Thus, after the first iteration in the example, samples 1, 2 and 7 would have been identified as interior samples (cyan crosses) and been moved outwards. A second iteration is then required to identify sample 6 as a now newly introduced interior sample. Note, however, that when removing sample 6 to complete the formation of the convex hull, a previously explored sample ends up falling within the constrained grid area. Since this explored sample has previously proved that the output does not exist at that specific geometrical point we cannot include this region as part of the final convex hull. As such, sample 6 is marked with a magenta cross for later exclusion from the convex hull.

iii) Generate an equi-spaced grid of 30×30 evaluation points covering the entire rectangular parameter space. Simplex theory is then utilised to eliminate all samples falling outside of the convex hull (Fig. 6.13(d)). Basically, if the sum of the areas of the triangles formed between each of the edges of the convex hull and a grid point, normalised to the area of the convex hull, is greater than one, that grid point falls outside of the constrained area and is removed.

iv) In the final computational step, evaluation samples are subtracted from the constrained samples presently filling the convex hull. These samples belong to convex regions that include previously explored samples that did not contribute to the output parameter. Exclusion of these samples requires reinsertion of those interior samples marked with magenta crosses. As these regions are convex in shape, samples can easily be removed using the same simplex theory technique discussed in (iii). In the example, sample 6 is reinserted to describe the final constrained evaluation region and exclude samples covering the convex region shown in Fig. 6.13(e).

The final constrained evaluation grid is shown in Fig. 6.13(f).

For simplicity, but without loss of generality, a two-dimensional scenario was assumed. Even though this has not been investigated, the proposed algorithm can, in principle, be extended to higher dimensions.

6.6 Suitable Degree Sets, Model Quality Assessment and Selection of a New Sample Location

When computing a polynomial interpolant, the basis consists of the different orders of the polynomial. When switching from one to many variables, however, the situation is completely different. Not only is there a large choice of multivariate functions, but moreover, different algorithms yield different interpolants and apply to different situations.

In [23] two choices of degrees sets $\mathcal{I}$ for multinomial and rational metamodels were presented, with the suggestion that the homogeneous set is the best choice when all input variables are of equal importance

$$\mathcal{I}_m^h = \left\{ (i_1, \cdots, i_d) \Big| \sum_{j=1}^{d} i_j \leq m \right\}. \tag{6.16}$$

This set can be seen as all degrees inside a simplex with vertices at the origin and at the points with all but one coordinate zero and one coordinate equal to m. Hendrickx [23] argued that degree sets of this type are more natural as an interpolant or approximant remains of the same form when the coordinate system undergoes a linear transformation.

Using an example, the homogeneous degree set in two dimensions with $m = 3$ is given by

$$\mathcal{I}_3^h = \big\{(0,0), (1,0), (0,1), (1,1), (2,0), (0,2), (2,1), (1,2), (3,0), (0,3)\big\}. \tag{6.17}$$

In some instances, however, more sophisticated schemes are required, e.g. a weight vector may attach some degree of importance to each coordinate axis. Similarly, the scheme can be required to adhere to specific constraints, e.g. the degrees of two coordinate axes may not differ by more than a given number V

$$\mathcal{I}_m^v = \left\{ (i_1, \cdots, i_d) \Big| \sum_{j=1}^{d} i_j \leq m; |i_j - i_k| \leq V, \ \forall k = 1, 2, \cdots, d \right\}. \tag{6.18}$$

Thus, for the example in Eq. 6.17 with $V = 1$, the degree set reduces to

$$\mathcal{I}_3^v = \big\{(0,0), (1,0), (0,1), (1,1), (2,1), (1,2)\big\}. \tag{6.19}$$

Since finding the order of the degrees is not the main part of the calculations, m was simply increased until a suitable number of solutions was found.

Now that the degree set has been established, the two best possible metamodels need to be chosen to select a new sample location. Hendrickx [23] proposed a method of grid evaluation and model quality assessment. Basically, a number of metamodels are built through the current

support samples. Each of these models is then evaluated on a grid, after which it can easily be cross-checked with other models by comparing all metamodels pairwise.

To assert the accuracy of each metamodel, an error matrix E is generated

$$E_{kl} = \left(\frac{1}{N_g} \sum_{i=1}^{N_g} \left| \Re_k(\mathbf{X}_i) - \Re_l(\mathbf{X}_i) \right|^2 \right)^{1/2}, \tag{6.20}$$

where E_{kl} is the root mean square error between metamodels k and l, N_g is the total number of grid points in the full-factorial design and $\mathbf{X}_i$ are the grid points at which each model is evaluated. Following from Eq. 6.20, E is symmetric with zeros on the diagonal. Also, if E_{kl} is small this indicates that metamodels k and l are quite similar.

Next, all models receive a score according to the formula

$$\frac{1}{Q_l} = \sum_{k \neq l} \frac{1}{E_{kl}}, \tag{6.21}$$

which identifies models that are most similar to other models. All metamodels are ordered with respect to their Q_l scores. Experiments done by Hendrickx have shown that models with a small Q_l agree better to other models than those with larger Q_l values. Hendrickx also noted that an exception to this rule occurs when two metamodels have particularly similar metamodel parameters. In such cases, the Q's for both of these models will be extremely small ($< 1e^{-10}$) and the models are therefore ignored.

By selecting the two best metamodels, i.e. models with lowest Q scores, and finding the position of maximum relative error between these two models across the grid

$$E(\mathbf{X}) = \max\left(\frac{|\Re_1(\mathbf{X}) - \Re_2(\mathbf{X})|}{|\Re_1(\mathbf{X})|}, \frac{|\Re_1(\mathbf{X}) - \Re_2(\mathbf{X})|}{|\Re_2(\mathbf{X})|} \right), \tag{6.22}$$

a possible new sample location has been identified. However, since every output (resonant mode) would require its own separate metamodel, the above procedure of model quality assessment needs to be repeated for every output. A point of biggest mismatch for each of these modes is then identified and a new sample is added at the point of largest error among these. Note that adding a single support point in the parameter space would result in a sample value being added for each output or resonant mode upon completion of the next frequency interpolation cycle.

Alternatively to the sample selection procedure implemented, other feasible techniques also exist. Lamecki [9] suggested adding support points, one at a time, as long as the error decreases. If the error suddenly increases, indicating poor stability of the numerical solution, the d-parameter space is divided into 2^d sub-spaces and multiple support points are introduced simultaneously, one in each sub-space at the point of biggest interpolant mismatch. A similar procedure was used when a cluster of support points formed.

Hendrickx [23] suggested that multiple sample points be added in each iteration. Sample clustering would be avoided by enforcing a minimal distance between two sample points being added, and the number of sample points added would be restricted by two bounds. This was achieved by randomly adding or removing samples to ensure that the number of samples added in each iteration fall within the specified lower and upper bounds. For the present technique of modelling multiple resonant modes, multiple support points could also be added by introducing a sample for each of the outputs at the point of biggest interpolant mismatch. Alternatively, a single sample could be added by cycling through the various outputs, with each iteration using a different resonant mode to establish a suitable location for adding a new support point to the sample set. Note that these two techniques have not been implemented, but may be investigated in future research.

6.7 Results

In this section a selection of two-dimensional and three-dimensional results are presented to illustrate the proposed modelling algorithm. Computational electromagnetic (CEM) analyses are performed with a full-wave Method of Moments (MoM) code, while the resonant structures being modelled are all of the annular ring resonator type. More specifically, metamodels are built for the TM_{nm0} resonant frequencies of an unloaded lossy microstrip ring resonator on a Taconic TLY-5 substrate, which has a relative permittivity of $\epsilon_r = 2.2$, a dissipation factor of $\tan(\delta) = 0.0009$ and a thickness of $h = 0.508$ mm. The results are verified within the predefined parameter space, which includes frequency and possible geometrical parameters. In the examples presented, the geometrical space may consist of the mean ring radius R and/or the normalised ring width w/R.

6.7.1 Study 1—Two-Dimensional Modelling, with f and R Variable

In this study, the ring structure was chosen to support only TM_{n10} modes with the fundamental mode resonating between 1.5 GHz and 2.5 GHz. The test setup consisted of an unloaded lossy microstrip ring resonator with mean ring radius interval $R = [13.5\text{ mm}, 22.5\text{ mm}]$ and normalised ring width $w/R = 0.05$, while the frequency interval was set to $f = [1\text{ GHz}, 11\text{ GHz}]$. The problem was initialised with $N_x = 4$ and $N_s = 5$ equi-spaced samples, where N_x is the number of geometrical samples at which the adaptive frequency sampling loop is performed and N_s is the number of samples in a specific frequency sampling loop. The adaptive frequency sampling loops terminated upon reaching a 0.25% convergence or variation of the roots, while the adaptive geometrical sampling loop terminated when all output models (the different TM_{nm0} resonant frequencies) reached a convergence of better than 1%, i.e. for each of the outputs the two best quality models should agree to within 1% over the interpolation interval.

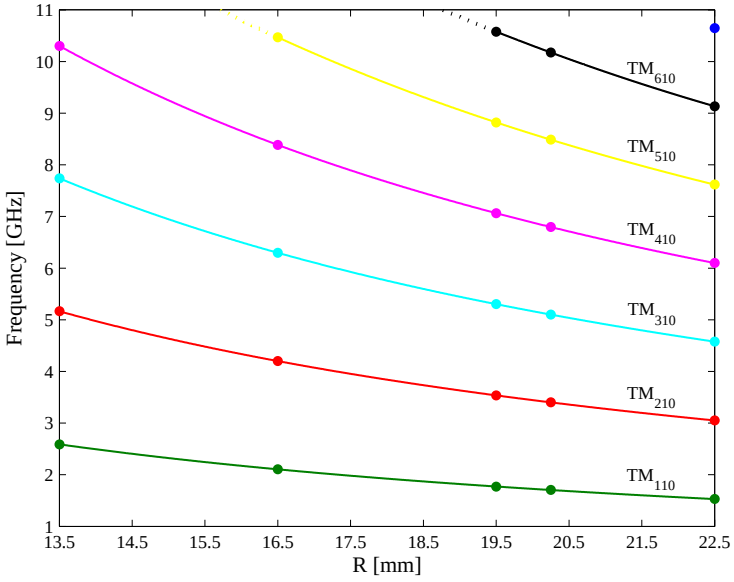

Fig. 6.14. Two-dimensional model of a ring resonator with frequency and mean ring radius variable. (Ring parameters: $R = [13.5 \text{ mm}, 22.5 \text{ mm}]$, $w/R = 0.05$; $f = [1 \text{ GHz}, 11 \text{ GHz}]$)

Fig. 6.14 plots the first six TM_{n10} mode frequencies that were successfully identified and approximated. Convergence of these models was reached within only 5 geometrical samples ($N_x = 5$), while the total number of CEM analyses added up to $N_{s,\text{tot}} = 163$, with a total of $N_{z,\text{tot}} = 56$ resonant frequencies correctly identified. Note that these roots all occurred as degenerate resonance pairs. Table 6.6 lists the individual number of samples N_s required by each of the adaptive frequency sampling loops, with the number of samples increasing almost proportionally to the number of roots identified.

Upon further analysis it was also noted that the TM_{710} resonance frequency was only identified at $R = 22.5$ mm. Since at least three samples are required to build a metamodel, this mode is not added to the output space and no model was constructed. Also, the dotted lines fall outside of the constrained interpolation area and shows extrapolated model values. In some instances the extrapolated values may be fairly accurate, as would seem to be the case for the present example. However, in other situations these values cannot be trusted. Section 6.8 elaborates on this topic of accuracy in the interpolation and extrapolation models.

TABLE 6.6
NUMBER OF SAMPLES REQUIRED TO REACH CONVERGENCE IN EACH OF THE ADAPTIVE FREQUENCY SAMPLING LOOPS.
(RING PARAMETERS: $R = [13.5 \text{ mm}, 22.5 \text{ mm}]$, $w/R = 0.05$; $f = [1 \text{ GHz}, 11 \text{ GHz}]$)

Number of Geometrical Samples (N_x)	R [mm]	Number of Frequency Samples (N_s)	Number of Roots Found (N_z)
1	13.50	26	8
2	22.50	38	14
3	16.50	27	10
4	19.50	32	12
5	20.25	40	12

6.7.2 Study 2—Two-Dimensional Modelling, with f and w/R Variable

In this study, the ring structure was chosen to support both TM_{n10} modes and higher-order TM_{nm0} modes by varying the normalised ring width. The test problem consisted of an unloaded lossy microstrip ring resonator with mean ring radius $R = 16.9$ mm and normalised ring width interval of $w/R = [0.05, 0.6]$, while the frequency interval was set to $f = [1.5\ \mathrm{GHz}, 10.5\ \mathrm{GHz}]$. The problem was initialised with $N_x = 4$ and $N_s = 5$ equi-spaced samples; the adaptive frequency sampling loops terminated upon reaching a 0.25% convergence of the roots and the adaptive geometrical sampling loop terminated when all output models reached a convergence of better than 0.1% over the interpolation interval.

Fig. 6.15 shows the final interpolated (solid) and extrapolated (dotted) modelling results. Convergence was reached with $N_x = 12$, requiring a total of $N_{s,\mathrm{tot}} = 590$ CEM evaluations identifying $N_{z,\mathrm{tot}} = 171$ resonant frequencies. Table 6.7 lists the individual number of samples N_s required by each of the adaptive frequency sampling loops, together with the number of roots identified.

In this example higher-order modes are also being modelled. Since these modes only exist for $w/R > 0.2$, it was found that the samples tend to be more densely spaced in regions where more outputs are being modelled. Also, note that in some instances (e.g. $w/R = 0.4167$) the adaptive frequency sampling algorithm fails to identify some of the higher-order resonance frequencies. This was found to happen only when the resonance frequencies of two different modes are numerically close. However, this poses no significant problem, as the model for that mode is simply built using less data. A disadvantage, however, might be that the constrained region of interpolation ends up being more constrained than is actually the case (see TM_{020} and TM_{120}). Also, the algorithm might require selection of a few more geometrical samples with

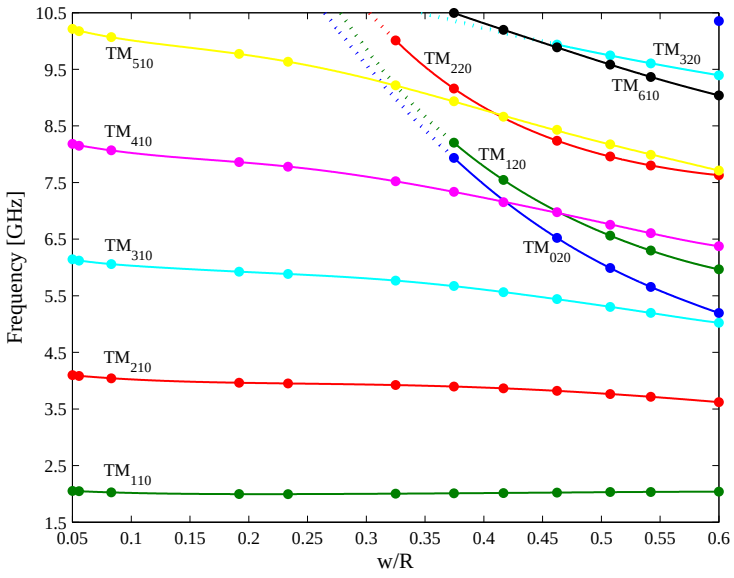

Fig. 6.15. Two-dimensional model of a ring resonator with frequency and normalised ring width variable. (Ring parameters: $R = 16.9$ mm, $w/R = [0.05, 0.6]$; $f = [1.5\ \mathrm{GHz}, 10.5\ \mathrm{GHz}]$)

TABLE 6.7
NUMBER OF SAMPLES REQUIRED TO REACH CONVERGENCE IN EACH OF THE ADAPTIVE FREQUENCY SAMPLING LOOPS.
(RING PARAMETERS: $R = 16.9$ mm, $w/R = [0.05, 0.6]$; $f = [1.5$ GHz, 10.5 GHz$]$)

Number of Geometrical Samples (N_x)	R [mm]	Number of Frequency Samples (N_s)	Number of Roots Found (N_z)
1	0.0500	26	10
2	0.6000	76	21
3	0.2333	36	10
4	0.4167	58	14
5	0.3250	56	13
6	0.0556	26	10
7	0.1917	31	10
8	0.5421	66	19
9	0.4623	63	19
10	0.5075	65	19
11	0.3745	59	16
12	0.0830	28	10

the associated execution of the adaptive frequency loop before convergence is reached. Upon termination, however, all the metamodels are accurate within the given requirements.

6.7.3 Study 3—Three-Dimensional Modelling, with f, R and w/R Variable

As a final example, a three-dimensional test problem is shown. The problem consists of an unloaded lossy microstrip ring resonator with mean ring radius $R = [15.35$ mm, 18.75 mm$]$ and normalised ring width $w/R = [0.1, 0.6]$, while the frequency interval was set to $f = [4.5$ GHz, 9.5 GHz$]$. The parameter space was chosen to verify correct modelling of both fundamental and higher-order modes. The problem was initialised with $N_x = 9$ (3×3 equi-

TABLE 6.8
NUMBER OF SAMPLES REQUIRED TO REACH CONVERGENCE IN EACH OF THE ADAPTIVE FREQUENCY SAMPLING LOOPS.
(RING PARAMETERS: $R = [15.35$ mm, 18.75 mm$]$, $w/R = [0.1, 0.6]$; $f = [4.5$ GHz, 9.5 GHz$]$)

Number of Geometrical Samples (N_x)	R [mm]	w/R	Number of Frequency Samples (N_s)	Number of Roots Found (N_z)
1	15.3500	0.10000	22	4
2	15.3500	0.35000	48	4
3	15.3500	0.60000	41	11
4	17.0500	0.10000	18	4
5	17.0500	0.35000	48	8
6	17.0500	0.60000	49	15
7	18.7500	0.10000	18	6
8	18.7500	0.35000	48	8
9	18.7500	0.60000	48	18
10	17.3431	0.58276	46	15
11	16.6397	0.58276	47	13
12	18.7500	0.35862	48	11
13	16.9913	0.48347	43	11
14	18.7500	0.49180	39	15
15	18.7500	0.22069	22	6
16	15.9362	0.51379	40	11
17	15.7017	0.22069	20	4
18	17.1086	0.15172	23	4
19	17.6948	0.41688	39	10
20	18.1638	0.18621	21	6
21	17.8121	0.43353	42	11
22	16.8741	0.53341	48	13

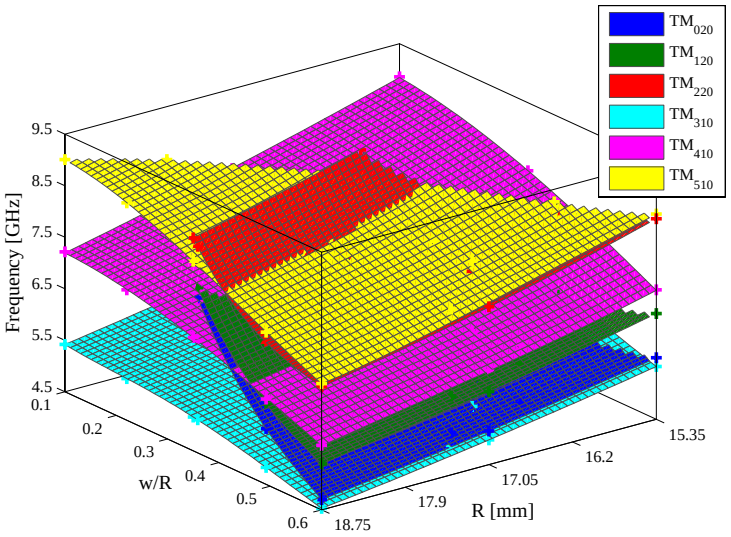

(a) Metamodels of the resonance frequencies of a microstrip ring resonator.

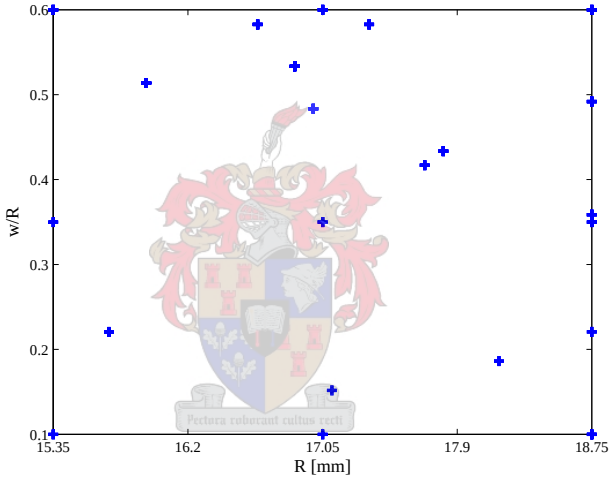

(b) Sample locations.

Fig. 6.16. Three-dimensional model of a ring resonator with frequency, ring radius and normalised ring width variable. (Ring parameters: $R = [15.35\text{ mm}, 18.75\text{ mm}]$, $w/R = [0.1, 0.6]$; $f = [4.5\text{ GHz}, 9.5\text{ GHz}]$)

spaced grid) and $N_s = 5$; the adaptive frequency sampling loop terminated upon reaching a 0.25% convergence of the roots and the adaptive geometrical sampling loop terminated when all output models reached a convergence of better than 0.1% over the interpolation interval.

Fig. 6.16(a) shows the final interpolated results, with Fig. 6.16(b) plotting the adaptively selected sample locations. Once again, the samples are arranged with a higher density in regions where the number of outputs are more, thereby automatically working towards reaching the interpolation goals. Convergence was reached with $N_x = 22$ requiring a total of $N_{s,\text{tot}} = 818$ CEM evaluations and identifying $N_{z,\text{tot}} = 208$ resonant frequencies. Table 6.8 lists the individual number of samples N_s required by each of the adaptive frequency sampling loops, together with the number of roots identified. Note that in this problem the frequency range was set out of range of the TM_{110} and TM_{210} modes, emphasising that the technique is capable of working

within restricted bounds and not limited to searching for the resonance frequencies from dc upwards.

6.8 Accuracy of the Final Metamodels

Once a model is evaluated on a grid, it can easily be cross-checked with the reference data set at all grid locations, to assess how well the model fits the data. In reality, however, the full dataset will not be at hand and is computationally expensive to compute.

In this section, the analytical solution of the magnetic-wall model (instead of the MoM) is used to obtain a set of reference data and to assess the accuracy of interpolated and extrapolated model values within the parameter space. Note that to make a decent comparison between the reference data and interpolation models, it is required that the magnetic-wall model also be used to compute the resonance frequencies that are being interpolated. Accuracy tests were performed for Studies 2 and 3 as was presented in Sections 6.7.2 and 6.7.3.

Fig. 6.17 shows the progression of an error percentage plot for the interpolated and extrapolated model values of Study 2. Upon termination of the interpolation algorithm, 99% of the samples agreed within 0.1% of the reference data, clearly verifying the accuracy of the interpolant models (Fig. 6.17(a)). Interpolation models are, however, known to be accurate within the interpolation space only. Since the interpolation area may be bounded, the accuracy of the extrapolated model values also needs to be investigated. Fig 6.17(b) shows that even though the extrapolated data samples are slightly less accurate, they all agree to within 2.5% of the reference data.

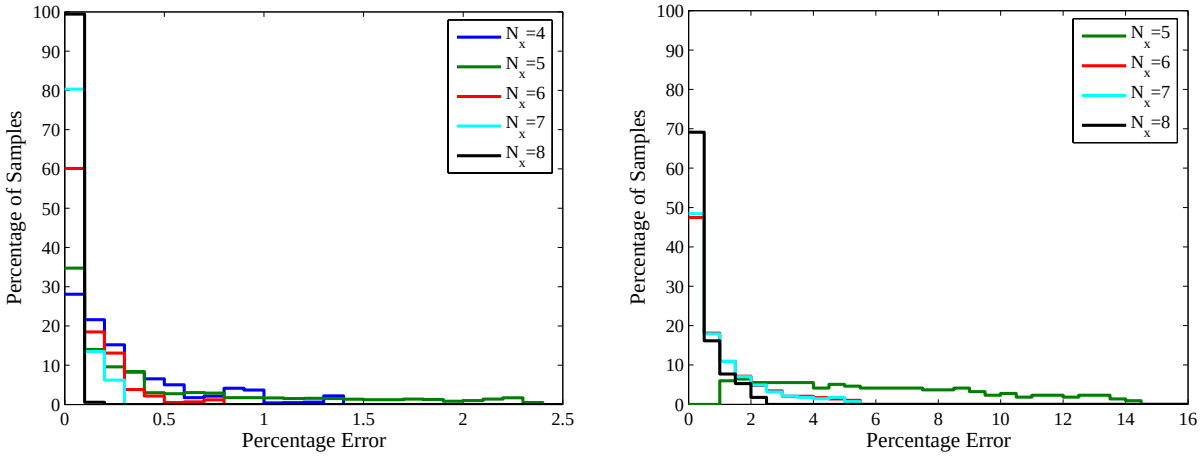

(a) Accuracy of interpolated samples.

(b) Accuracy of extrapolated samples.

Fig. 6.17. Accuracy of the final metamodels over the interpolated and extrapolated regions within the complete parameter space. Results are presented for a two-dimensional model of a ring resonator with frequency and normalised ring width variable. (Ring parameters: $R = 16.9$ mm, $w/R = [0.05, 0.6]$; $f = [1.5\text{ GHz}, 10.5\text{ GHz}]$)

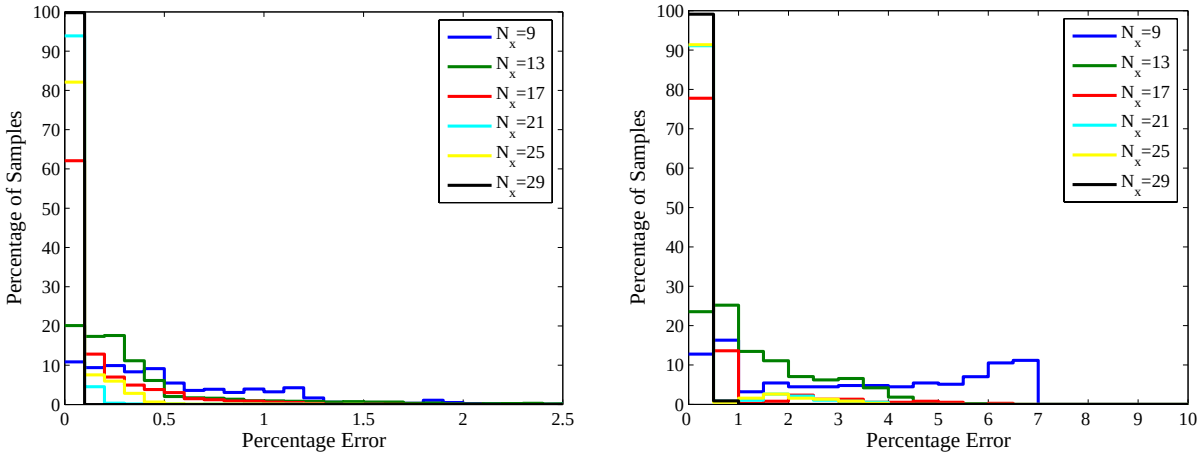

(a) Accuracy of interpolated samples.

(b) Accuracy of extrapolated samples.

Fig. 6.18. Accuracy of the final metamodels over the interpolated and extrapolated regions within the complete parameter space. Results are presented for a three-dimensional model of a ring resonator with frequency, ring radius and normalised ring width variable. (Ring parameters: $R = [15.35\text{ mm}, 18.75\text{ mm}]$, $w/R = [0.1, 0.6]$; $f = [1.5\text{ GHz}, 9.5\text{ GHz}]$)

Similar results were obtained when assessing the accuracy of the three-dimensional models of Study 3 (Section 6.7.3). Fig. 6.18(a) shows the progression of an error percentage plot as evaluated at different stages in the model building procedure. As the number of samples (N_x) increases, the percentage samples in the model that accurately compares with the reference data also increases. The higher-order model also shows greater promise for extrapolating data accurately, as 99% of the evaluated samples are within 0.5% of the reference data.

In Study 2 (Section 6.7.2), it was observed that the adaptive frequency sampling algorithm occasionally fails to identify some of the higher-order resonance frequencies, especially when the resonance frequencies of two different modes are numerically close. Using a statistical Monte Carlo analysis of this same problem, it can be shown that the proposed algorithm is self-compensating, building metamodels of high accuracy despite the absence of some zeros. Figs. 6.19(b)-(f) illustrate the Monte Carlo error percentage plots over the complete parameter space in the absence of either 1, 2, 3, 4 or 5 resonance frequencies. In Fig. 6.19(a) the equivalent error percentage plot is shown for the instance where all resonance frequencies were correctly identified. Each Monte Carlo analysis consisted of 50 simulations and a set number of resonance frequencies were randomly ignored while building the output metamodels. Statistically, it is evident that most samples evaluated with the metamodels are within about 1% error of the reference data, regardless of the number of resonance frequencies ignored. In Fig. 6.20 the statistical analysis data of Figs. 6.19(a)-(f) is combined into a single plot in which the percentage error of model data to reference data when the root-finding algorithm randomly ignores a set number of resonance frequencies is compared. More than 80% of all samples are accurate to within 0.1% of the reference data, while the remaining samples show a maximum error of around 0.5%. Considering that these results include both interpolated and extrapolated (no accuracy guaranteed) values, the accuracy of these models are typically found to be more than sufficient.

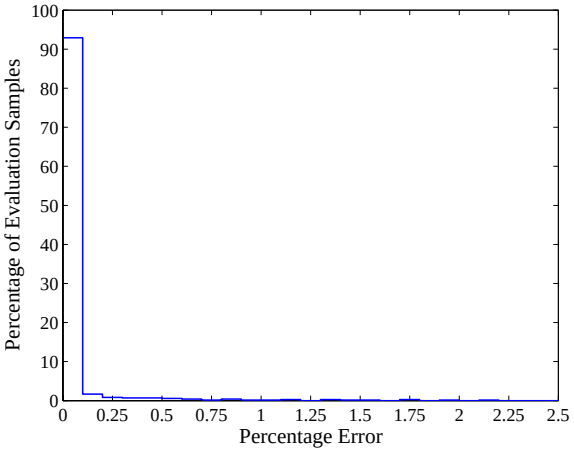

(a) Analysis with all zeros identified.

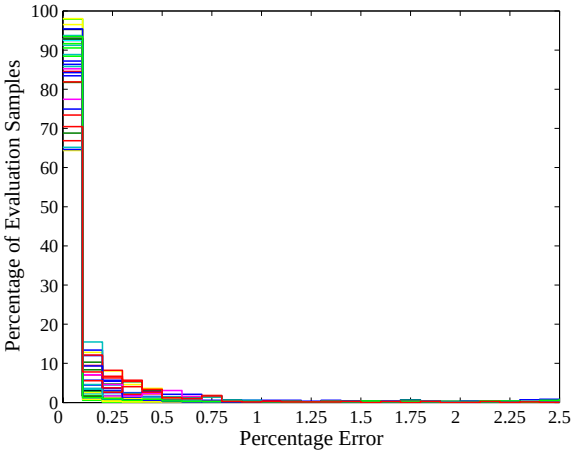

(b) Monte Carlo analysis ignoring 1 zero.

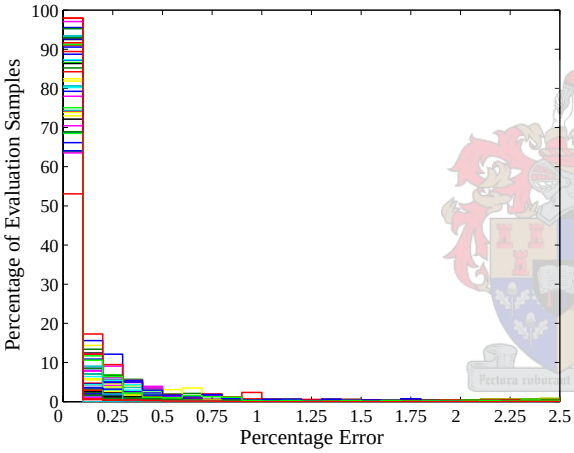

(c) Monte Carlo analysis ignoring 2 zeros.

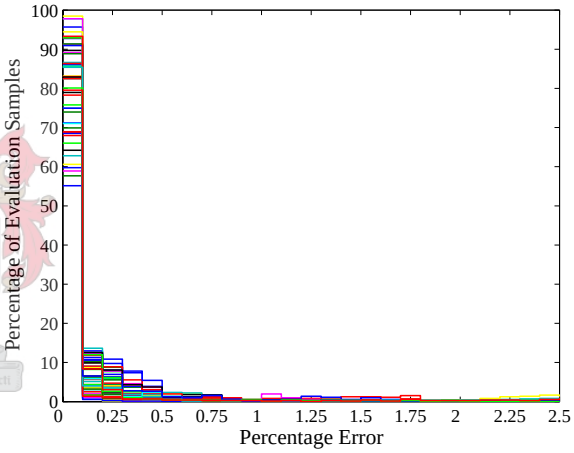

(d) Monte Carlo analysis ignoring 3 zeros.

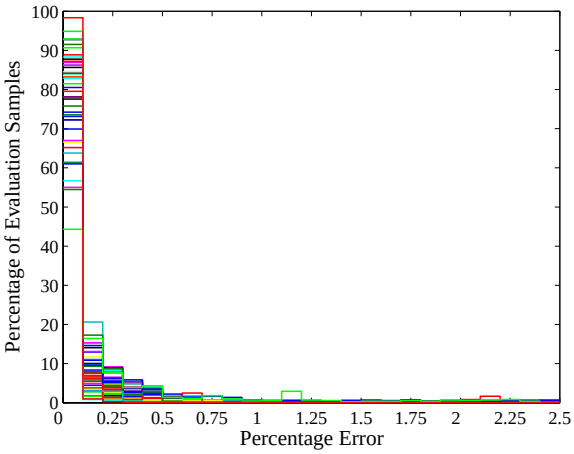

(e) Monte Carlo analysis ignoring 4 zeros.

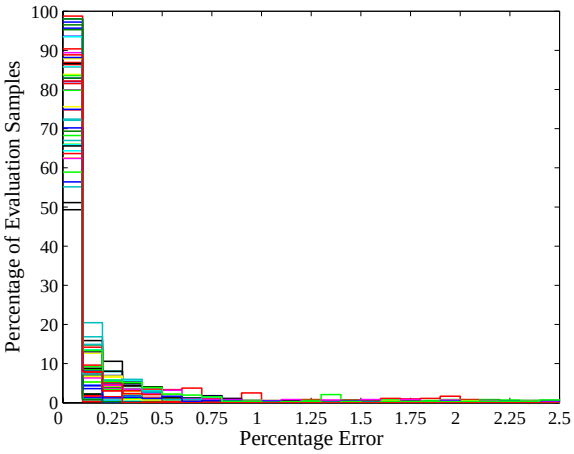

(f) Monte Carlo analysis ignoring 5 zeros.

Fig. 6.19. Statistical analysis of the output model accuracy over the complete parameter space when ignoring random resonance frequencies. Results are presented for a two-dimensional model of a ring resonator with frequency and normalised ring width variable. (Ring parameters: $R = 16.9$ mm, $w/R = [0.05, 0.6]$; $f = [1.5\text{ GHz}, 10.5\text{ GHz}]$)

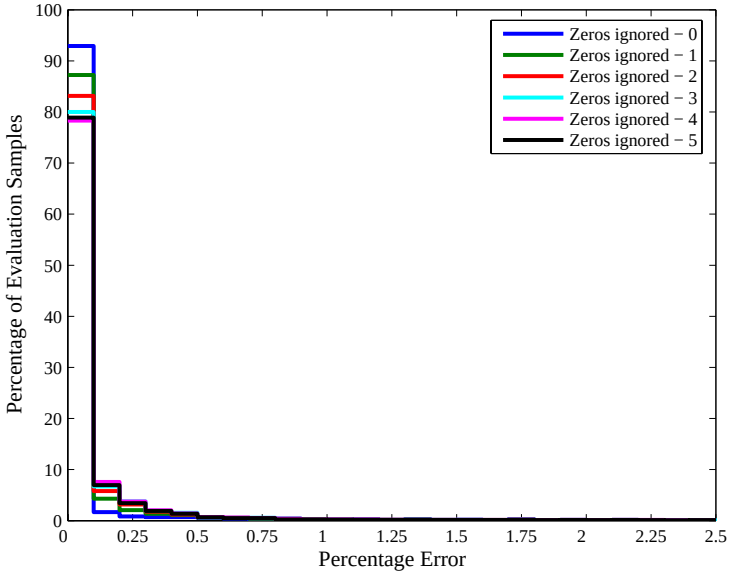

Fig. 6.20. Comparison of the accuracy of model data to reference data when the root-finding algorithm randomly ignores a set number of resonance frequencies. Results are presented for a two-dimensional model of a ring resonator with frequency and normalised ring width variable. (Ring parameters: $R = 16.9$ mm, $w/R = [0.05, 0.6]$; $f = [1.5\text{ GHz}, 10.5\text{ GHz}]$)

Similar results are shown in Fig. 6.21 where Study 3 (Section 6.7.3) has been statistically analysed, ignoring 5 random resonance frequencies in each of the 50 simulations performed. Almost 90% of all evalutated samples (covering the complete parameter space) are within 0.1% of the reference data, with the remaining 10% of samples differing from reference data by at most 0.5%.

These results yield sufficient proof that the proposed algorithm can build models of high accu-

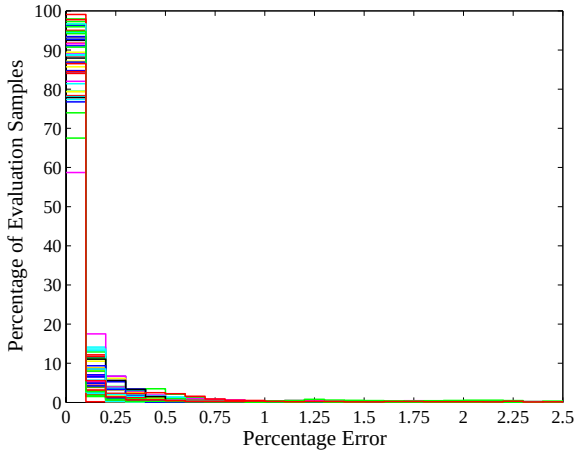

(a) Monte Carlo analysis ignoring 5 zeros.

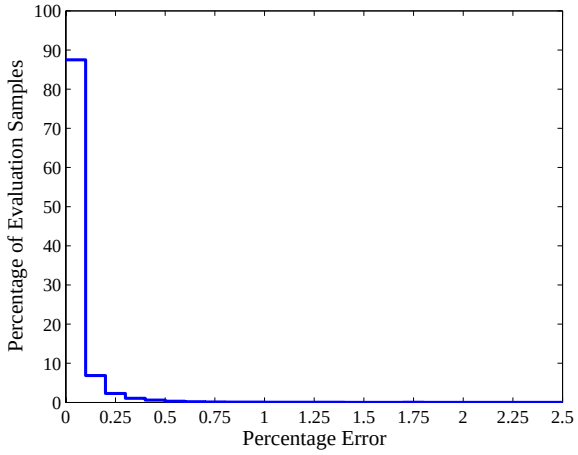

(b) Combined statistical accuracy over the complete parameter space.

Fig. 6.21. Statistical analysis of the output model accuracy over the complete parameter space when ignoring 5 random resonance frequencies. Results are presented for a three-dimensional model of a ring resonator with frequency, ring radius and normalised ring width variable. (Ring parameters: $R = [15.35\text{ mm}, 18.75\text{ mm}]$, $w/R = [0.1, 0.6]$; $f = [1.5\text{ GHz}, 9.5\text{ GHz}]$)

racy, even when some resonance frequencies are left unidentified in the process. The accuracy of results have been presented over the complete parameter space including both interpolated and extrapolated data.

6.9 Conclusion

In this chapter, an automated parameterised model generation algorithm has been presented to model the multiple input, multiple output resonance behaviour of unloaded microwave ring resonators. The frequency dependence is treated separately using adaptive rational Vector Fitting, while the geometrical parameter space is modelled using multinomial approximation techniques. This separation of parameters is essential as the input space of the unloaded eigenmode problem is found to be discontinuous across the geometrical dimensions.

This chapter also presented a new convergence criterion to an existing adaptive frequency sampling technique. The algorithm takes advantage of the knowledge that the resonance frequencies of the structure need to be found accurately. As such, the algorithm terminates upon convergence of these roots. A 25% reduction in the number of support points required to accurately predict the natural frequencies of a microwave resonator is achieved.

A new automated algorithm that associates resonance frequencies with known modes has also been illustrated. The technique relies on digital signal principles such as cross-correlation and variance, and ideal mode patterns are computed analytically using the magnetic-wall model. It was also shown that the technique works, without change, with square ring resonators.

Next, a constrained grid modelling approach was introduced and illustrated for both one and two dimensions. The technique is based on finding a convex hull around all output samples, while excluding previously explored regions where the output was found to either not exist or fall outside of the interpolation space.

Finally, results for both two- and three-dimensional input models were presented. It was shown that the proposed modelling algorithm can successfully model different TM_{nm0} resonant frequencies. In addition, the technique self-compensates and builds high-accuracy models even when the adaptive frequency sampling algorithm occasionally fails to identify some of the higher-order resonance frequencies. The technique was further verified by investigating the accuracy of the interpolation solution and extrapolation results by means of Monte Carlo analyses. Statistically, more than 80% of samples modelling the complete parameter space were accurate to within 0.1% of the reference data used.

Chapter 7

Conclusion

This dissertation has investigated interpolation-based modelling of planar microwave resonators, which was then successfully utilised to accurately predict those resonator characteristics (f_0 and Q) that are most important for designers of microwave devices. The study on modelling of resonance frequencies has been conducted in both one- and multi-dimensional parameter spaces, while the study on modelling of Q-values has been performed in one dimension only.

The development of a multivariate adaptive rational-multinomial combination interpolant has been presented. The algorithm models multiple resonance frequencies of a microwave ring resonator simultaneously. Unlike most of the present multi-dimensional modelling techniques using mostly S-parameter responses of a loaded structure to build a model, the proposed algorithm is based on the solution of an eigenmode problem.

Modelling of the eigenmode determinant function in a MoM solution is subject to frequency scaling and a discontinuous solution space in multiple dimensions. The proposed algorithm addresses the frequency dimension separately from other physical parameters by solving two consecutive adaptive sampling loops. Firstly, the zeros of a one-dimensional adaptive rational Vector Fitting sampling loop, for a specific set of parameter values, are identified and categorised into specific resonant modes. Each of these modes are then modelled using multi-dimensional adaptive multinomial interpolation. Instead of modelling the complete discontinuous parameter space, multiple models characterising the resonance behaviour for each of the resonance modes are built.

The modelling algorithm includes a number of new sub-algorithms:

i) A new convergence criterion is applied to an existing adaptive frequency sampling technique. The algorithm terminates upon reaching root-convergence instead of the standard technique of model-convergence, and showed a 25% reduction in the number of support samples required to accurately predict the natural frequencies of a microwave resonator.

ii) An automated mode identification algorithm based on digital signal principles and ideal

mode patterns of simplified resonator models was suggested. The technique clearly distinguishes the identified mode from other modes and was also successfully applied to square ring resonators.

iii) A constrained grid modelling approach was developed to exclude evaluation samples from previously explored regions, where the output was found to either not exist or fall outside of the interpolation space.

The modelling algorithm was succesfully tested on both two- and three-dimensional input models. Statistical analysis results suggest that the proposed algorithm can build models of high accuracy and self-compensates when some resonance frequencies are left unidentified in the process. The accuracy of results has been presented over the complete parameter space, including interpolated and extrapolated data.

The author anticipates that future extensions of this work could include the following:

i) Orthonormal multinomials are known to improve numerical stability and efficiency of the interpolant [7]. Hence, an investigation into the use of orthonormal multinomial basis instead of the classical multinomial basis presently implemented should be done.

ii) Application of the different sample selection criteria discussed in Section 6.6 to the proposed algorithm should be investigated.

When modelling quality factors, a three-point rational interpolant function in the region of resonance for the calculation of loaded quality factors has been proposed. The technique utilises the already known interpolant coefficients of the S-parameter response of a resonator. By using only three of the interpolant coefficients at a time, the Q-factors are obtained without any additional CEM effort. In standard techniques the extraction of quality factors is obtained by Q-circle fits on multi-frequency S-parameter data. These techniques rely on least-squares fits, which normally require large numbers of frequency points. The new technique provides a direct fit and solution to the Q-factors.

The modelling algorithm was successfully tested against both high-Q and low-Q resonators. Unfortunately the technique cannot be applied to noisy measurement data and, in addition, the technique is based on the S_{11} reflection parameter, which becomes ill-defined under low coupling conditions, yielding unreliable results. The TMQF technique proves to be a far more robust Q-factor extraction technique when applied to the transmission response. The author would suggest using this technique instead, however, utilise interpolation-based models to efficiently generate the S-parameter data needed to solve the least-squares problem.

In conclusion, the investigation resulted in a robust, efficient and accurate multi-dimensional interpolation technique for the extraction of resonant frequencies. In addition, the proposed Q-extraction technique, though not very reliable under weak coupling conditions, did verify that interpolation techniques can be used to good effect to predict Q-values.

Bibliography

[1] A.J. Booker, J.E. Dennis, P.D. Frank, Jr., D.B. Serafini, V. Torczon, and M.W. Trosset, "A Rigorous Framework for Optimization of Expensive Functions by Surrogates," *Structural Optimization*, vol. 17, no. 1, pp. 1–13, Feb. 1999.

[2] J.-F. Liang and K.A. Zaki, "CAD of Microwave Junctions by Polynomial Curve Fitting," *IEEE MTT-S Digest*, vol. 1, pp. 451–454, 1993.

[3] J. Carroll and K. Chang, "Statistical Computer-Aided Design for Microwave Circuits," *IEEE Trans. on Microwave Theory and Techniques*, vol. 44, no. 1, pp. 24–32, Jan. 1996.

[4] T. Dhaene, J. Ureel, N. Faché, and D. de Zutter, "Adaptive Frequency Sampling Algorithm for Fast and Accurate S-parameter Modeling of General Planar Structures," *IEEE MTT-S Digest*, vol. 3, pp. 1427–1430, 1995.

[5] R.S. Adve, T.K. Sarkar, S.M. Rao, E.K. Miller, and D.R. Pflug, "Application of the Cauchy Method for Extrapolating/Interpolating Narrow-Band System Responses," *IEEE Trans. on Microwave Theory and Techniques*, vol. 45, no. 5, pp. 837–845, May 1997.

[6] S.F. Peik, R.R. Mansour, and Y.L. Chow, "Multidimensional Cauchy Method and Adaptive Sampling for an Accurate Microwave Circuit Modeling," *IEEE Trans. on Microwave Theory and Techniques*, vol. 46, no. 12, pp. 2364–2371, Dec. 1998.

[7] J. de Geest, T. Dhaene, N. Faché, and D. de Zutter, "Adaptive CAD-Model Building Algorithm for General Planar Microwave Structures," *IEEE Trans. on Microwave Theory and Techniques*, vol. 47, no. 9, pp. 1801–1809, Sept. 1999.

[8] R. Lehmensiek and P. Meyer, "Creating Accurate Multivariate Rational Interpolation Models of Microwave Circuits by using Efficient Adaptive Sampling to Minimize the Number of Computational Electromagnetic Analyses," *IEEE Trans. on Microwave Theory and Techniques*, vol. 49, no. 8, pp. 1419–1430, Aug. 2001.

[9] A. Lamecki, P. Kozakowski, and M. Mrozowski, "Efficient Implementation of the Cauchy Method for Automated CAD-Model Construction," *IEEE Microwave and Wireless Components Letters*, vol. 13, no. 7, pp. 268–270, July 2003.

[10] W. Hendrickx and T. Dhaene, "Sequential Design and Rational Metamodelling," *Winter Simulation Conference (WSC '05), Orlando (FL)*, pp. 290–298, Dec. 2005.

[11] A. Cuyt, R.B. Lenin, S. Becuwe, and B. Verdonk, "Adaptive Multivariate Rational Data Fitting With Applications in Electromagnetics," *IEEE Trans. on Microwave Theory and Techniques*, vol. 54, no. 5, pp. 2265–2274, May 2006.

[12] U. Beyer and F. Śmieja, "Data Exploration with Reflective Adaptive Models," *Elsevier Computational Statistics and Data Analysis*, vol. 22, pp. 193–211, 1996.

[13] R. Lehmensiek and P. Meyer, "An Efficient Adaptive Frequency Sampling Algorithm for Model-Based Parameter Estimation as Applied to Aggressive Space Mapping," *Microwave and Optical Technology Letters*, vol. 24, no. 1, pp. 71–78, Jan. 2000.

[14] R. Lehmensiek, P. Meyer, and M. Müller, "Adaptive Sampling Applied to Multivariate, Multiple Output Rational Interpolation Models with Application to Microwave Circuits," *International Journal of RF and Microwave Computer-Aided Engineering*, vol. 12, no. 4, pp. 332–340, July 2002.

[15] R. Lehmensiek, *Efficient Adaptive Sampling Applied to Multivariate, Multiple Output Rational Interpolation Models, With Applications in Electromagnetics-Based Device Modelling*, PhD dissertation, University of Stellenbosch, 2001.

[16] R. Lehmensiek and P. Meyer, "Using Efficient Model-Based Parameter Estimation for Pole-Free Solutions of Modal Propagation Constants, as Applied to Shielded Planar Structures," *Applied Computational Electromagnetics Society Journal*, vol. 16, no. 1, pp. 1–10, Mar. 2001.

[17] D. Deschrijver and T. Dhaene, "Univariate Rational Macromodeling of High-Speed Passive Components: A Comparative Study," *Applied Computational Electromagnetics Society Newsletter*, vol. 20, no. 2, pp. 35–60, 2005.

[18] K. Kottapalli, T.K. Sarkar, Y. Hua, E.K. Miller, and G.J. Burke, "Accurate Computation of Wide-Band Response of Electromagnetic Systems Utilizing Narrow-Band Information," *IEEE Trans. on Microwave Theory and Techniques*, vol. 39, no. 4, pp. 682–687, Apr. 1991.

[19] C. Brezinski, "Padé-type Approximation and General Orthogonal Polynomials," *Basel, Switzerland: Birkhauser Verlag*, 1980.

[20] B. Gustavsen and A. Semlyen, "Rational Approximation of Frequency Domain Responses by Vector Fitting," *IEEE Trans. on Power Delivery*, vol. 14, no. 3, pp. 1052–1061, July 1999.

[21] G. Blanch, "Numerical Evaluation of Continued Fractions," *SIAM Rev.*, vol. 6, no. 4, pp. 383–421, Oct. 1964.

[22] T. Dhaene and J. de Geest, "Adaptive Multidimensional Model for General Electrical Interconnection Structures by Optimizing Orthogonal Expansion Parameters," *Agilent Technologies, Inc., U.S. Patent, No. US 6295635 (B1)*, Sept. 2001.

[23] W. Hendrickx and T. Dhaene, "Multivariate Modelling of Complex Simulation-Based Systems," *The 4th International Workshop on Multidimensional (nD) Systems (IEEE NDS)*, pp. 212–216, July 2005.

[24] M. Schoeman, "Mixed-Potential Integral Equation Technique for Hybrid Microstrip-Slotline Multi-Layered Circuits with Horizontal and Vertical Shielding Walls," Study project presented in partial fulfillment of the requirements for the degree of Master of Engineering, University of Stellenbosch, Dec. 2003.

[25] M. Schoeman and P. Meyer, "On the use of Adaptive Rational Interpolation for the Calculation of Resonator Characteristics from MoM Analysis," *International Conference on Adaptive Modeling and Simulation (ADMOS)*, pp. 317–320, Sept. 2005.

[26] M. Schoeman and P. Meyer, "On the use of Adaptive Rational Interpolation for the Calculation of Resonator Characteristics from EM Analysis," *International Journal of RF and Microwave Computer-Aided Engineering*, 2006, accepted.

[27] M. Schoeman and P. Meyer, "A Comparative Study on Adaptive Rational Macromodels of Highly Resonant Structures," *International Journal of RF and Microwave Computer-Aided Engineering*, 2006, accepted.

[28] M. Schoeman and P. Meyer, "Prediction of Microwave Resonator Frequencies using 1D Adaptive Vector Fitting," *International Conference on Numerical Analysis and Applied Mathematics (ICNAAM)*, 2006, accepted.

[29] M. Schoeman and P. Meyer, "Prediction of Microwave Resonator Frequencies using Multi-Dimensional Adaptive Interpolation-Based Modelling," *IEEE Trans. on Microwave Theory and Techniques*, 2006, submitted for publication.

[30] J.R. Mosig and F.E. Gardiol, "General Integral Equation Formulation for Microstrip Antennas and Scatterers," *IEE Proceedings*, vol. 132, pp. 424–432, Dec. 1985.

[31] L. Barlatey, J.R. Mosig, and T. Sphicopoulos, "Analysis of Stacked Microstrip Patches with a Mixed Potential Integral Equation," *IEEE Trans. on Antennas and Propagation*, vol. 38, no. 5, pp. 608–615, May 1990.

[32] K.A. Michalski and D. Zheng, "Electromagnetic Scattering and Radiation by Surfaces of Arbitrary Shape in Layered Media, Part I: Theory," *IEEE Trans. on Antennas and Propagation*, vol. 38, no. 3, pp. 335–344, Mar. 1990.

[33] S.M. Rao, D.R. Wilton, and A.W. Glisson, "Electromagnetic Scattering by Surfaces of Arbitrary Shape," *IEEE Trans. on Antennas and Propagation*, vol. AP-30, no. 3, pp. 409–418, May 1982.

[34] W.C. Chew, *Waves and Fields in Inhomogeneous Media*, Van Nostrand Reinhold, New York, 1990.

[35] J.J. van Tonder, "Electromagnetic Field of HED/VED Dipole Located in Layered Medium," Tech. Rep. 1, Electromagnetic Software & Systems, Apr. 2000.

[36] R.A. Pucel, D.J. Massé, and C.P. Hartwig, "Losses in Microstrip," *IEEE Trans. on Microwave Theory and Techniques*, vol. MTT-16, no. 6, pp. 342–350, June 1968.

[37] R.A. Pucel, D.J. Massé, and C.P. Hartwig, "Correction to "Losses in Microstrip" (Correspondence)," *IEEE Trans. on Microwave Theory and Techniques*, vol. 16, no. 12, pp. 1064, 1968.

[38] E. Belohoubek and E. Denlinger, "Loss Considerations for Microstrip Resonators," *IEEE Trans. on Microwave Theory and Techniques*, pp. 522–526, June 1975.

[39] K.-F. Lee and S.R. Chebolu, "On the Role of Substrate Loss Tangent in the Cavity Model Theory of Microstrip Patch Antennas," *IEEE Trans. on Antennas and Propagation*, vol. 42, no. 1, pp. 110–112, Jan. 1994.

[40] J. Gómez-Tagle and C.G. Christodoulou, "Extended Cavity Model Analysis of Stacked Microstrip Ring Antennas," *IEEE Trans. on Antennas and Propagation*, vol. 45, no. 11, pp. 1626–1635, Nov. 1997.

[41] L.-H. Hsieh and K. Chang, "Equivalent Lumped Elements G, L, C, and Unloaded Q's of Closed- and Open-Loop Ring Resonators," *IEEE Trans. on Microwave Theory and Techniques*, vol. 50, no. 2, pp. 453–460, Feb. 2002.

[42] D. de Zutter and L. Knockaert, "Skin Effect Modeling Based on a Differential Surface Admittance Operator," *IEEE Trans. on Microwave Theory and Techniques*, vol. 53, no. 8, pp. 2526–2538, Aug. 2005.

[43] J.J. van Tonder, "Numerical Analysis of Microstrip Patch Antennas," Study project presented in partial fulfillment of the requirements for the degree of Master of Engineering, University of Stellenbosch, 1992.

[44] Computer Simulation Technology, *CST Microwave Studio Version 5.1: Calculate Skin-Depth and Surface Roughness*, 1998-1994.

[45] D.M. Pozar, *Microwave Engineering*, John Wiley and Sons, Inc., 2nd edition, 1998.

[46] B. Roudot, J. Mosig, and F. Gardiol, "Surface Wave Effects on Microstrip Antenna Radiation," *Microwave Journal*, pp. 201–211, Mar. 1988.

[47] D. El-Kouhen, H. Aubert, M. Ghomi, and H. Baudrand, "Q-Factor Computation of Radiation Loss Corresponding to Surface Wave in a Patch Circular Resonator," *Electronic Letters*, vol. 32, no. 22, pp. 2039–2041, Oct. 1996.

[48] R.F. Harrington, *Field Computations by Moment Methods*, New York: Macmillan, 1968.

[49] M. Irsadi and R. Mittra, "Estimation of Spurious Radiation from Microstrip Etches using Closed-Form Green's Functions," *IEEE Trans. on Microwave Theory and Techniques*, vol. 40, no. 11, pp. 2063–2069, Nov. 1992.

[50] J.-C. Liu, C.-S. Cheng, and L. Yao, "Dual-Mode Double-Ring Resonator for Microstrip Band-Pass Filter Design," *Microwave and Optical Technology Letters*, vol. 36, no. 4, pp. 310–314, Feb. 2002.

[51] P.C.L. Yin, *High-Frequency Circuit Design and Measurements*, Chapman & Hall.

[52] A. Semlyen and B. Gustavsen, "Vector Fitting by Pole Relocation for the State Equation Approximation of Nonrational Transfer Matrices," *Circuits, Systems and Signal Processing*, vol. 19, no. 6, pp. 549–566, 2000.

[53] B. Gustavsen, "Calculation of Zeros in Vector Fitting," http://www.energy.sintef.no/Produkt/VECTFIT/index.asp, May 2004.

[54] W. Hendrickx, D. Deschrijver, and T. Dhaene, "Some Remarks on the Vector Fitting Iteration," *European Conference on Mathematics for Industry (ECMI)*, 2004.

[55] P. Troughton, "Measurement Techniques in Microstrip," *Electronic Letters*, vol. 5, no. 2, pp. 25–26, Jan. 1969.

[56] I. Wolff and N. Knoppik, "Microstrip Ring Resonator and Dispersion Measurement on Microstrip Lines," *Electronic Letters*, vol. 7, no. 26, pp. 779–781, Dec. 1971.

[57] Y.S. Wu and F.J. Rosenbaum, "Mode Chart for Microstrip Ring Resonators," *IEEE Trans. on Microwave Theory and Techniques*, vol. MTT-21, pp. 487–489, July 1973.

[58] I. Wolff, "Microstrip Bandpass Filter using Degenerate Modes of a Microstrip Ring Resonator," *Electronic Letters*, vol. 8, no. 12, pp. 302–303, June 1972.

[59] R.P. Owens, "Curvature Effect in Microstrip Ring Resonators," *Electronic Letters*, vol. 12, no. 14, pp. 356–357, July 1976.

[60] M. Kirschning and R.H. Jansen, "Accurate Model for Effective Dielectric Constant of Microstrip and Validity up to Millimeter-Wave Frequencies," *Electronic Letters*, vol. 18, no. 6, pp. 272–273, Mar. 1982.

[61] R.P. Owens, "Predicted Frequency Dependence of Microstrip Characteristic Impedance using the Planar-Waveguide Model," *Electronic Letters*, vol. 12, no. 11, pp. 269–270, May 1976.

[62] I. Wolff and V.K. Tripathi, "The Microstrip Open-Ring Resonator," *IEEE Trans. on Microwave Theory and Techniques*, vol. MTT-32, no. 1, pp. 102–107, Jan. 1984.

[63] W. Sun, K.-M. Chen, D.P. Nyquist, and E.J. Rothwell, "Determination of the Natural Modes for a Rectangular Plate," *IEEE Trans. on Antennas and Propagation*, vol. 38, no. 5, pp. 643–652, May 1990.

[64] Y. Long, "Determination of the Natural Frequencies for Conducting Rectangular Boxes," *IEEE Trans. on Antennas and Propagation*, vol. 42, no. 7, pp. 1016–1021, July 1994.

[65] C.A. Olley and T.E. Rozzi, "Systematic Characterisation of the Spectrum of Unilateral Finline," *IEEE Trans. on Microwave Theory and Techniques*, vol. MTT-34, no. 11, pp. 1147–1156, Nov. 1986.

[66] V.A. Labay and J. Bornemann, "Matrix Singular Value Decomposition for Pole-Free Solutions of Homogenous Matrix Equations as Applied to Numerical Modelling Methods," *IEEE Microwave and Guided Wave Letters*, vol. 2, no. 2, pp. 49–51, Feb. 1992.

[67] U. Rogge and R. Pregla, "Method of Lines for the Analysis of Dielectric Waveguides," *Journal of Lightwave Technologies*, vol. 11, no. 12, pp. 2015–2020, Dec. 1993.

[68] P. Meyer, "Solving Microstrip Discontinuities with a Combined Mode-Matching and Method-of-Lines procedure," *Microwave and Optical Technology Letters*, vol. 8, no. 1, pp. 4–8, Jan. 1995.

[69] Visual Numerics, *IMSL Help Documentation: Fortran Subroutines for Mathematical Application*, 1997.

[70] G. Peters and J.H. Wilkinson, "Practical Problems arising in the Solution of Polynomial Equations," *J. Inst. Math. Appl.*, vol. 8, pp. 16–35, 1971.

[71] S. Grivet-Talocia and M. Bandinu, "Improving the Convergence of Vector Fitting for Equivalent Circuit Extraction From Noisy Frequency Responses," *IEEE Trans. on Electromagnetic Compatibility*, vol. 48, no. 1, pp. 104–120, Feb. 2006.

[72] K. Chang, S. Martin, F. Wang, and J.L. Klein, "On the Study of Microstrip Ring and Varactor-Tuned Ring Circuits," *IEEE Trans. on Microwave Theory and Techniques*, vol. MTT-35, no. 12, pp. 1288–1295, Dec. 1987.

[73] G.K. Gopalakrishnan and K. Chang, "Bandpass Characteristics of Split-Modes in Asymmetric Ring Resonators," *Electronic Letters*, vol. 26, no. 12, pp. 774–775, June 1990.

[74] K. Chang and L.-H. Hsieh, *Microwave Ring Circuits and Related Structures*, Wiley Series in Microwave and Optical Engineering. John Wiley and Sons, Inc., 2nd edition, 2004.

[75] D. Kajfez and E.J. Hwan, "Q-Factor Measurement with Network Analyzer," *IEEE Trans. on Microwave Theory and Techniques*, vol. MTT-32, no. 7, pp. 666–670, July 1984.

[76] W.P. Wheless, Jr. and D. Kajfez, "Microwave Resonator Circuit Model from Measured Data Fitting," *IEEE MTT-S Digest*, , no. AA-5, pp. 681–684, June 1986.

[77] W.P. Wheless and D. Kajfez, "Determination of Dual-Mode Q Factors from Measured Data," *IEEE MTT-S Digest*, , no. J-34, pp. 375–378, 1987.

[78] W.P. Wheless, Jr. and D. Kajfez, "Experimental Characterization of Multimoded Microwave Resonators using Automated Network Analyzer," *IEEE Trans. on Microwave Theory and Techniques*, vol. MTT-35, no. 12, pp. 1263–1270, Dec. 1987.

[79] J.R. Bray and L. Roy, "Measuring the Unloaded, Loaded, and External Quality Factors of One- and Two-Port Resonators using Scattering-Parameter Magnitudes at Fractional Power Levels," *IEE Proc.-Microwave Antennas Propagation*, vol. 151, no. 4, pp. 345–350, Aug. 2004.

[80] D. Kajfez, "Linear Fractional Curve Fitting for Measurement of High Q Factors," *IEEE Trans. on Microwave Theory and Techniques*, vol. 42, no. 7, pp. 1149–1153, July 1994.

[81] D. Kajfez, "Q-Factor Measurement with a Scalar Network Analyser," *IEE Proc.-Microwave Antennas Propagation*, vol. 142, no. 5, pp. 369–372, Oct. 1995.

[82] K. Leong, J. Mazierska, and J. Krupka, "Measurements of Unloaded Q-Factor of Transmission Mode Dielectric Resonators," *IEEE MTT-S Digest*, vol. 3, pp. 1639–1642, 1997.

[83] D. Kajfez, S. Chebolu, M.R. Abdul-Gaffoor, and A.A. Kishk, "Uncertainty Analysis of the Transmission-Type Measurement of Q-Factor," *IEEE Trans. on Microwave Theory and Techniques*, vol. 47, no. 3, pp. 367–371, Mar. 1999.

[84] K. Leong and J. Mazierska, "Precise Measurements of the Q Factor of Dielectric Resonators in the Transmission Mode—Accounting for Noise, Crosstalk, Delay of Uncalibrated Lines, Coupling Loss, and Coupling Reactance," *IEEE Trans. on Microwave Theory and Techniques*, vol. 50, no. 9, pp. 2115–2127, Sept. 2002.

[85] V. Rizzoli, A. Costanzo, C. Cecchetti, and D. Masotti, "Computer-Aided Optimization of Broadband Nonlinear Microwave Integrated Circuits with the Aid of Electromagnetically generated Look-Up Tables," *Microwave and Optical Technology Letters*, vol. 15, no. 4, pp. 189–196, July 1997.

[86] P. Burrascano, S. Fiori, and M. Mongiardo, "A Review of Artificial Neural Networks Applications in Microwave Computer-Aided Design," *International Journal of RF and Microwave Computer-Aided Engineering*, vol. 9, no. 3, pp. 158–174, May 1999.

[87] T. Dhaene, J. de Geest, and D. de Zutter, "EM-based Multidimensional Parameterized Modeling of General Passive Planar Components," *IEEE MTT-S Digest*, vol. 3, pp. 1745–1748, May 2001.

[88] R.H. Bartels and J.J. Jezioranski, "Least-Squares Fitting using Orthogonal Multinomials," *ACM Trans. on Mathematical Software*, vol. 11, no. 3, pp. 201–217, Sept. 1985.

[89] J. Stoer and R. Bulirsch, *Introduction to Numerical Analysis*, New York: Springer, cop., 1980.

[90] R. Lehmensiek and P. Meyer, "Using Efficient Multivariate Adaptive Sampling by Minimizing the Number of Computational Electromagnetic Analysis Needed to Establish Accurate Interpolation Models," *IEEE MTT-S Digest*, vol. 1, pp. 1749–1752, May 2001.

[91] G.H. Golub and C.F. van Loan, *Matrix Computations*, Baltimore, MD: The Johns Hopkins Univ. Press, 1996.

[92] T. Dhaene, J. de Geest, and D. de Zutter, "Constrained EM-based Modeling of Passive Components," *IEEE MTT-S Digest*, vol. 3, pp. 2113–2116, 2002.

[93] T. Dhaene and J. de Geest, "Self-Organizing Multivariate Constrained Meta-Modeling Technique for Passive Microwave and RF Components," *Elsevier Future Generation Computer Systems*, vol. 21, no. 7, pp. 1040–1046, July 2005.

[94] P.Z. Peebles, Jr., *Probability, Random Variables and Random Signal Principles*, McGraw-Hill International Edition Electrical Engineering Series, 4 edition, 2001.